FERMI LARGE AREA TELESCOPE THIRD SOURCE CATALOG

F. Acero[1], M. Ackermann[2], M. Ajello[3], A. Albert[4], W. B. Atwood[5], M. Axelsson[6,7,8], L. Baldini[9], J. Ballet[1],
G. Barbiellini[10,11], D. Bastieri[12,13], A. Belfiore[14], R. Bellazzini[15], E. Bissaldi[16], R. D. Blandford[4], E. D. Bloom[4],
J. R. Bogart[4], R. Bonino[17,18], E. Bottacini[4], J. Bregeon[19], R. J. Britto[20], P. Bruel[21], R. Buehler[2], T. H. Burnett[22],
S. Buson[12,13], G. A. Caliandro[4,23], R. A. Cameron[4], R. Caputo[5], M. Caragiulo[16], P. A. Caraveo[14], J. M. Casandjian[1],
E. Cavazzuti[24], E. Charles[4], R. C. G. Chaves[19], A. Chekhtman[25], C. C. Cheung[26], J. Chiang[4], G. Chiaro[13],
S. Ciprini[24,27,28], R. Claus[4], J. Cohen- Tanugi[19], L. R. Cominsky[29], J. Conrad[6,8,30,70], S. Cutini[24,27,28], F. D'Ammando[31,32],
A. De Angelis[33], M. DeKlotz[34], F. de Palma[16,35], R. Desiante[10,36], S. W. Digel[4], L. Di Venere[37], P. S. Drell[4], R. Dubois[4],
D. Dumora[38], C. Favuzzi[16,37], S. J. Fegan[21], E. C. Ferrara[39], A. Finke[26], A. Franckowiak[4], Y. Fukazawa[40], S. Funk[4],
P. Fusco[16,37], F. Gargano[16], D. Gasparrini[24,27,28], B. Giebels[21], N. Giglietto[16,37], P. Giommi[24], F. Giordano[16,37],
M. Giroletti[31], T. Glanzman[4], G. Godfrey[4], I. A. Grenier[1], M.-H. Grondin[38], J. E. Grove[26], L. Guillemot[41,42],
S. Guiriec[39,au], D. Hadasch[43], A. K. Harding[39], E. Hays[39], J. W. Hewitt[44,45], A. B. Hill[4,46,72], D. Horan[21], G. Iafrate[10,47],
T. Jogler[4], G. Jóhannesson[48], R. P. Johnson[5], A. S. Johnson[4], T. J. Johnson[25], W. N. Johnson[26], T. Kamae[4], J. Kataoka[49],
J. Katsuta[40], M. Kuss[15], G. La Mura[13,43], D. Landriu[1], S. Larsson[6,7,8], L. Latronico[17], M. Lemoine- Goumard[38,73], J. Li[50],
L. Li[8,51], F. Longo[10,11], F. Loparco[16,37], B. Lott[38], M. N. Lovellette[26], P. Lubrano[27,52], G. M. Madejski[4], F. Massaro[53],
M. Mayer[2], M. N. Mazziotta[16], J. E. McEnery[39,54], P. F. Michelson[4], N. Mirabal[39,71], T. Mizuno[55], A. A. Moiseev[45,54],
M. Mongelli[16], M. E. Monzani[4], A. Morselli[56], I. V. Moskalenko[4], S. Murgia[57], E. Nuss[19], M. Ohno[40], T. Ohsugi[55],
N. Omodei[4], M. Orienti[31], E. Orlando[4], J. F. Ormes[58], D. Paneque[4,59], J. H. Panetta[4], J. S. Perkins[39], M. Pesce- Rollins[15],
F. Piron[19], G. Pivato[15], T. A. Porter[4], J. L. Racusin[39], R. Rando[12,13], M. Razzano[15,74], S. Razzaque[20], A. Reimer[4,43],
O. Reimer[4,43], T. Reposeur[38], L. S. Rochester[4], R. W. Romani[4], D. Salvetti[14], M. Sánchez- Conde[6,8],
P. M. Saz Parkinson[5,60], A. Schulz[2], E. J. Siskind[61], D. A. Smith[38], F. Spada[15], G. Spandre[15], P. Spinelli[16,37],
T. E. Stephens[62], A. W. Strong[63], D. J. Suson[64], H. Takahashi[40], T. Takahashi[65], Y. Tanaka[55], J. G. Thayer[4], J. B. Thayer[4],
D. J. Thompson[39], L. Tibaldo[4], O. Tibolla[66], D. F. Torres[50,67], E. Torresi[68], G. Tosti[27,52], E. Troja[39,54], B. Van Klaveren[4],
G. Vianello[4], B. L. Winer[69], K. S. Wood[26], M. Wood[4], and S. Zimmer[6,8]

[1] Laboratoire AIM, CEA-IRFU/CNRS/Université Paris Diderot, Service d'Astrophysique, CEA Saclay, F-91191 Gif sur Yvette, France; jean.ballet@cea.fr
[2] Deutsches Elektronen Synchrotron DESY, D-15738 Zeuthen, Germany
[3] Department of Physics and Astronomy, Clemson University, Kinard Lab of Physics, Clemson, SC 29634-0978, USA
[4] W. W. Hansen Experimental Physics Laboratory, Kavli Institute for Particle Astrophysics and Cosmology, Department of Physics and SLAC National Accelerator Laboratory, Stanford University, Stanford, CA 94305, USA; digel@stanford.edu
[5] Santa Cruz Institute for Particle Physics, Department of Physics and Department of Astronomy and Astrophysics, University of California at Santa Cruz, Santa Cruz, CA 95064, USA
[6] Department of Physics, Stockholm University, AlbaNova, SE-106 91 Stockholm, Sweden
[7] Department of Astronomy, Stockholm University, SE-106 91 Stockholm, Sweden
[8] The Oskar Klein Centre for Cosmoparticle Physics, AlbaNova, SE-106 91 Stockholm, Sweden
[9] Università di Pisa and Istituto Nazionale di Fisica Nucleare, Sezione di Pisa I-56127 Pisa, Italy
[10] Istituto Nazionale di Fisica Nucleare, Sezione di Trieste, I-34127 Trieste, Italy
[11] Dipartimento di Fisica, Università di Trieste, I-34127 Trieste, Italy
[12] Istituto Nazionale di Fisica Nucleare, Sezione di Padova, I-35131 Padova, Italy
[13] Dipartimento di Fisica e Astronomia "G. Galilei," Università di Padova, I-35131 Padova, Italy
[14] INAF-Istituto di Astrofisica Spaziale e Fisica Cosmica, I-20133 Milano, Italy
[15] Istituto Nazionale di Fisica Nucleare, Sezione di Pisa, I-56127 Pisa, Italy
[16] Istituto Nazionale di Fisica Nucleare, Sezione di Bari, I-70126 Bari, Italy
[17] Istituto Nazionale di Fisica Nucleare, Sezione di Torino, I-10125 Torino, Italy
[18] Dipartimento di Fisica Generale "Amadeo Avogadro," Università degli Studi di Torino, I-10125 Torino, Italy
[19] Laboratoire Univers et Particules de Montpellier, Université Montpellier, CNRS/IN2P3, Montpellier, France
[20] Department of Physics, University of Johannesburg, P.O. Box 524, Auckland Park 2006, South Africa
[21] Laboratoire Leprince-Ringuet, École polytechnique, CNRS/IN2P3, Palaiseau, France
[22] Department of Physics, University of Washington, Seattle, WA 98195-1560, USA; tburnett@u.washington.edu
[23] Consorzio Interuniversitario per la Fisica Spaziale (CIFS), I-10133 Torino, Italy
[24] Agenzia Spaziale Italiana (ASI) Science Data Center, I-00133 Roma, Italy; elisabetta.cavazzuti@asdc.asi.it
[25] College of Science, George Mason University, Fairfax, VA 22030, resident at Naval Research Laboratory, Washington, DC 20375, USA
[26] Space Science Division, Naval Research Laboratory, Washington, DC 20375-5352, USA
[27] Istituto Nazionale di Fisica Nucleare, Sezione di Perugia, I-06123 Perugia, Italy
[28] INAF Osservatorio Astronomico di Roma, I-00040 Monte Porzio Catone (Roma), Italy
[29] Department of Physics and Astronomy, Sonoma State University, Rohnert Park, CA 94928-3609, USA
[30] The Royal Swedish Academy of Sciences, Box 50005, SE-104 05 Stockholm, Sweden
[31] INAF Istituto di Radioastronomia, I-40129 Bologna, Italy
[32] Dipartimento di Astronomia, Università di Bologna, I-40127 Bologna, Italy
[33] Dipartimento di Fisica, Università di Udine and Istituto Nazionale di Fisica Nucleare, Sezione di Trieste, Gruppo Collegato di Udine, I-33100 Udine, Italy
[34] Stellar Solutions Inc., 250 Cambridge Avenue, Suite 204, Palo Alto, CA 94306, USA
[35] Università Telematica Pegaso, Piazza Trieste e Trento, 48, I-80132 Napoli, Italy
[36] Università di Udine, I-33100 Udine, Italy
[37] Dipartimento di Fisica "M. Merlin" dell'Università e del Politecnico di Bari, I-70126 Bari, Italy
[38] Centre d'Études Nucléaires de Bordeaux Gradignan, IN2P3/CNRS, Université Bordeaux 1, BP120, F-33175 Gradignan Cedex, France
[39] NASA Goddard Space Flight Center, Greenbelt, MD 20771, USA

[40] Department of Physical Sciences, Hiroshima University, Higashi-Hiroshima, Hiroshima 739-8526, Japan
[41] Laboratoire de Physique et Chimie de l'Environnement et de l'Espace—Université d'Orléans / CNRS, F-45071 Orléans Cedex 02, France
[42] Station de radioastronomie de Nançay, Observatoire de Paris, CNRS/INSU, F-18330 Nançay, France
[43] Institut für Astro- und Teilchenphysik and Institut für Theoretische Physik, Leopold-Franzens-Universität Innsbruck, A-6020 Innsbruck, Austria
[44] Department of Physics and Center for Space Sciences and Technology, University of Maryland Baltimore County, Baltimore, MD 21250, USA
[45] Center for Research and Exploration in Space Science and Technology (CRESST) and NASA Goddard Space Flight Center, Greenbelt, MD 20771, USA
[46] School of Physics and Astronomy, University of Southampton, Highfield, Southampton, SO17 1BJ, UK
[47] Osservatorio Astronomico di Trieste, Istituto Nazionale di Astrofisica, I-34143 Trieste, Italy
[48] Science Institute, University of Iceland, IS-107 Reykjavik, Iceland
[49] Research Institute for Science and Engineering, Waseda University, 3-4-1, Okubo, Shinjuku, Tokyo 169-8555, Japan
[50] Institute of Space Sciences (IEEC-CSIC), Campus UAB, E-08193 Barcelona, Spain
[51] Department of Physics, KTH Royal Institute of Technology, AlbaNova, SE-106 91 Stockholm, Sweden
[52] Dipartimento di Fisica, Università degli Studi di Perugia, I-06123 Perugia, Italy
[53] Department of Astronomy, Department of Physics and Yale Center for Astronomy and Astrophysics, Yale University, New Haven, CT 06520-8120, USA
[54] Department of Physics and Department of Astronomy, University of Maryland, College Park, MD 20742, USA
[55] Hiroshima Astrophysical Science Center, Hiroshima University, Higashi-Hiroshima, Hiroshima 739-8526, Japan
[56] Istituto Nazionale di Fisica Nucleare, Sezione di Roma "Tor Vergata," I-00133 Roma, Italy
[57] Center for Cosmology, Physics and Astronomy Department, University of California, Irvine, CA 92697-2575, USA
[58] Department of Physics and Astronomy, University of Denver, Denver, CO 80208, USA
[59] Max-Planck-Institut für Physik, D-80805 München, Germany
[60] Department of Physics, The University of Hong Kong, Pokfulam Road, Hong Kong, China
[61] NYCB Real-Time Computing Inc., Lattingtown, NY 11560-1025, USA
[62] Harold B. Lee Library, Brigham Young University, Provo, UT 84602, USA
[63] Max-Planck Institut für extraterrestrische Physik, D-85748 Garching, Germany
[64] Department of Chemistry and Physics, Purdue University Calumet, Hammond, IN 46323-2094, USA
[65] Institute of Space and Astronautical Science, Japan Aerospace Exploration Agency, 3-1-1 Yoshinodai, Chuo-ku, Sagamihara, Kanagawa 252-5210, Japan
[66] Mesoamerican Centre for Theoretical Physics (MCTP), Universidad Autónoma de Chiapas (UNACH), Carretera Emiliano Zapata Km. 4, Real del Bosque (Teràn),
29050 Tuxtla Gutiérrez, Chiapas, México
[67] Institució Catalana de Recerca i Estudis Avançats (ICREA), Barcelona, Spain
[68] INAF-IASF Bologna, I-40129 Bologna, Italy
[69] Department of Physics, Center for Cosmology and Astro-Particle Physics, The Ohio State University, Columbus, OH 43210, USA

ABSTRACT

We present the third *Fermi* Large Area Telescope (LAT) source catalog (3FGL) of sources in the 100 MeV–300 GeV range. Based on the first 4 yr of science data from the *Fermi Gamma-ray Space Telescope* mission, it is the deepest yet in this energy range. Relative to the Second *Fermi* LAT catalog, the 3FGL catalog incorporates twice as much data, as well as a number of analysis improvements, including improved calibrations at the event reconstruction level, an updated model for Galactic diffuse γ-ray emission, a refined procedure for source detection, and improved methods for associating LAT sources with potential counterparts at other wavelengths. The 3FGL catalog includes 3033 sources above 4σ significance, with source location regions, spectral properties, and monthly light curves for each. Of these, 78 are flagged as potentially being due to imperfections in the model for Galactic diffuse emission. Twenty-five sources are modeled explicitly as spatially extended, and overall 238 sources are considered as identified based on angular extent or correlated variability (periodic or otherwise) observed at other wavelengths. For 1010 sources we have not found plausible counterparts at other wavelengths. More than 1100 of the identified or associated sources are active galaxies of the blazar class; several other classes of non-blazar active galaxies are also represented in the 3FGL. Pulsars represent the largest Galactic source class. From source counts of Galactic sources we estimate that the contribution of unresolved sources to the Galactic diffuse emission is ∼3% at 1 GeV.

Key words: catalogs – gamma-rays: general

Supporting material: FITS file, machine-readable tables

1. INTRODUCTION

This paper presents a catalog of high-energy γ-ray sources detected in the first 4 yr of the *Fermi Gamma-ray Space Telescope* mission by the Large Area Telescope (LAT). It is the successor to the LAT Bright Source List (hereafter 0FGL; Abdo et al. 2009d), the First *Fermi* LAT (1FGL; Abdo et al. 2010d) catalog, and the Second *Fermi* LAT (2FGL; Nolan et al. 2012) catalog, which were based on 3 months, 11 months, and 2 yr of flight data, respectively. The 3FGL catalog both succeeds and complements the First *Fermi* LAT Catalog of Sources Above 10 GeV (1FHL, Ackermann et al. 2013a), which was based on 3 yr of flight data but considered only sources detected above 10 GeV. The new 3FGL catalog is the deepest yet in the 100 MeV–300 GeV energy range. The result of a dedicated effort for studying the active galactic nucleus (AGN) population in the 3FGL catalog is published in an accompanying paper (3LAC; Ackermann et al. 2015).

We have implemented a number of analysis refinements for the 3FGL catalog:

1. Pass 7 reprocessed data[75] are now used (Section 2.2). The principal difference relative to the original Pass 7 data used for 2FGL is improved angular resolution above 3 GeV. In addition, systematics of the instrument response functions (IRFs) are better characterized and smaller.

2. This catalog employs a new model of the diffuse Galactic and isotropic emissions, developed for the 3FGL analysis (Section 2.3). The model has improved fidelity to the observations, especially for regions where the diffuse emission cannot be described using a spatial template derived from observations at other wavelengths. In addition, the accuracy of the model is improved toward bright star-forming regions and at energies above 40 GeV generally. The development of this model is described in a separate publication (Casandjian & the Fermi LAT Collaboration 2015).

3. We explicitly model 25 sources as extended emission regions (Section 3.4), up from 12 in 2FGL. Each has an angular extent measured with LAT data. Taking into account the finite sizes of the sources allows for more accurate flux and spectrum measurements for the extended sources, as well as for nearby point sources.

4. We have further refined the method for characterizing and localizing source "seeds" evaluated for inclusion in the catalog (Section 3.1). The improvements in this regard are mostly marked at low Galactic latitudes, where an iterative approach to finding seeds has improved the sensitivity of the catalog in the Galactic plane.

5. For studying the associations of LAT sources with counterparts at other wavelengths, we have updated several of the catalogs used for counterpart searches and correspondingly recalibrated the association procedure.

The exposure of the LAT is fairly uniform across the sky, but the brightness of the diffuse backgrounds, and hence the sensitivity for source detection, depends strongly on direction. As for previous LAT source catalogs, for the 3FGL catalog sources are included based on the statistical significance of their detection considered over the entire time period of the analysis. For this reason the 3FGL catalog is not a comprehensive catalog of transient γ-ray sources; however, the catalog does include light curves on a monthly timescale for sources that meet the criteria for inclusion.

In Section 2 we describe the LAT and the models for the diffuse backgrounds, celestial and otherwise. Section 3 describes how the catalog is constructed, with emphasis on what has changed since the analysis for the 2FGL catalog. The 3FGL catalog itself is presented in Section 4, along with a comparison to previous LAT catalogs. We discuss associations and identifications in Section 5 and Galactic source counts in Section 6. The conclusions are presented in Section 7. We provide appendices with technical details of the analysis and of the format of the electronic version of the catalog.

2. INSTRUMENT AND BACKGROUND

2.1. The Large Area Telescope

The LAT detects γ-rays in the energy range from 20 MeV to more than 300 GeV, measuring their arrival times, energies,

and directions. The LAT is also an efficient detector of the intense background of charged particles from cosmic rays and trapped radiation at the orbit of the *Fermi* satellite. Accounting for γ-rays lost in filtering charged particles from the data, the effective collecting area is ∼6500 cm² at 1 GeV (for the P7REP_SOURCE_V15 event selection used here; see below). The live time is nearly 76%, limited primarily by interruptions of data taking when *Fermi* is passing through the South Atlantic Anomaly (SAA) (∼13%) and readout dead-time fraction (∼9%). The field of view of the LAT is 2.4 sr at 1 GeV. The per-photon angular resolution (point-spread function, PSF, 68% containment) is ∼5° at 100 MeV, decreasing to 0°.8 at 1 GeV (averaged over the acceptance of the LAT), varying with energy approximately as $E^{-0.8}$ and asymptoting at ∼0°.2 above 20 GeV. The tracking section of the LAT has 36 layers of silicon strip detectors interleaved with 16 layers of tungsten foil (12 thin layers, 0.03 radiation length, at the top or *Front* of the instrument, followed by four thick layers, 0.18 radiation length, in the *Back* section). The silicon strips track charged particles, and the tungsten foils facilitate conversion of γ-rays to positron–electron pairs. Beneath the tracker is a calorimeter composed of an eight-layer array of CsI crystals (∼8.5 total radiation lengths) to determine the γ-ray energy. A segmented charged-particle anticoincidence detector (plastic scintillators read out by photomultiplier tubes) around the tracker is used to reject charged-particle background events. More information about the LAT is provided in Atwood et al. (2009), and the in-flight calibration of the LAT is described in Abdo et al. (2009g) and Ackermann et al. (2012a, 2012c).

2.2. The LAT Data

The data for the 3FGL catalog were taken during the period from 2008 August 4 (15:43 UTC) to 2012 July 31 (22:46 UTC), to covering close to 4 yr. They are the public data available from the *Fermi* Science Support Center (FSSC). Intervals around bright GRBs (080916C, 090510, 090902B, 090926A, 110731A; Ackermann et al. 2013b) were excised. Solar flares became relatively frequent in 2011–12 (close to solar maximum) and were excised as well whenever they were bright enough to be detected over a month at the 3σ level. Solar flares last much longer than GRBs, so we were attentive not to reject too much time. Since the γ-ray emission is localized on the Sun, we kept intervals during which the Sun was at least 3° below the Earth limb[76] even during solar flares. The solar flares were detected over 3 hr intervals so the corresponding Good Time Intervals (GTIs) are aligned to those 3 hr marks. Overall about 2 days were excised due to solar flares. In order to reduce the contamination from the γ-ray-bright Earth limb (Section 2.3.4), times when the rocking angle of the spacecraft was larger than 52° and events with zenith angles larger than 100° were excised as well. The precise time intervals corresponding to selected events are recorded in the `GTI` extension of the 3FGL catalog (FITS version; Appendix B).

The rocking angle remained set at 50° after 2009 September (it was 35° for about 80% of the time before that).[77] With the larger rocking angle the orbital plane is further off axis with the
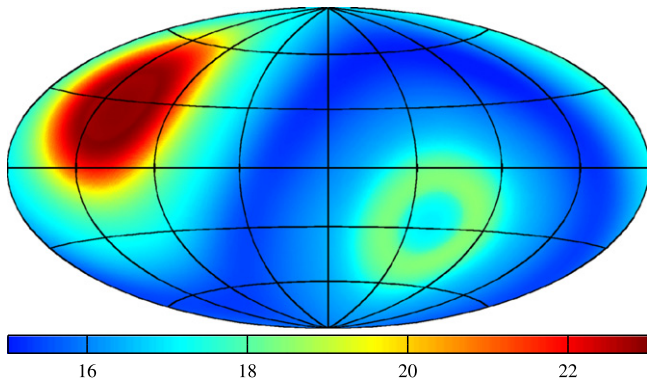

Figure 1. Exposure at 1 GeV in Galactic coordinates and Hammer–Aitoff projection for the 4 yr period analyzed for the 3FGL catalog. The units are equivalent on-axis observing time (in Ms).

result that the survey is slightly non-uniform. The maximum exposure is reached at the north celestial pole. At 1 GeV it is 60% larger than the minimum exposure, which is reached at the celestial equator (Figure 1).

In parallel with accumulating new data, developments on the instrument analysis side (Bregeon et al. 2013) led to reprocessing all LAT data with new calibration constants, resulting in the Pass 7 reprocessed data that were used for 3FGL.[78] The main advantage for the source catalog is that the reprocessing improved the PSF above 10 GeV by ∼30%, improving the localization of hard sources (Section 3.1). We used the source class event selection.

The lower bound of the energy range was left at 100 MeV, but the upper bound was raised to 300 GeV as in the 1FHL catalog. This is because as the source-to-background ratio decreases, the sensitivity curve (Figure 18 of Abdo et al. 2010d, 1FGL) shifts to higher energies.

2.3. Model for the Diffuse Gamma-ray Background

Models for the diffuse γ-ray backgrounds were updated for the 3FGL analysis, taking into account the new IRFs for Pass 7 reprocessed data and the improved statistics available with a 4 yr data set, and also applying some refinements in the procedure for evaluating the models. The primary components of the diffuse backgrounds are the diffuse γ-ray emission of the Milky Way and the approximately isotropic background consisting of emission from sub-threshold celestial sources plus residual charged particles misclassified as γ-rays. In addition, we treat the "passive" emission of the Sun and Moon from cosmic-ray interactions with the solar atmosphere, solar radiation field, and the lunar lithosphere as effectively a diffuse component, because the Sun and Moon move across the sky. The residual Earth limb emission after the zenith angle selection (Section 2.2) is also treated as effectively diffuse. Each component of the background model for the 3FGL analysis is described in more detail below.

2.3.1. Diffuse Emission of the Milky Way

The diffuse γ-ray emission of the Milky Way originates in cosmic-ray interactions with interstellar gas and radiation. As for 2FGL, for any given energy the model is primarily a linear

combination of template maps derived from CO and H I line survey data plus infrared maps of interstellar dust, which trace interstellar gas and in the model represent the γ-ray emission from pion decay and bremsstrahlung. In addition, we include in the model a template representing the intensity of emission from inverse Compton scattering of cosmic-ray electrons on the interstellar radiation field. This component was calculated using the GALPROP code[79] (Moskalenko & Strong 1998).

For the 3FGL analysis we have made several improvements relative to 2FGL in modeling the diffuse emission. The development of this new model is described by Casandjian & the Fermi LAT Collaboration (2015).[80] Here we briefly summarize the improvements. For 3FGL the representation of the gas traced uniquely by the infrared maps was improved in the vicinity of massive star-forming regions. The overall model was fit to the LAT data iteratively, taking into account a preliminary version of the 3FGL source list, for the energy range 50 MeV–50 GeV. Relative to the 2FGL model for Galactic diffuse emission, we have improved the extrapolation to lower and higher energies using the energy dependence of the γ-ray emissivity function. We developed a new procedure to account for the structured celestial γ-ray emission that could not be fit using templates derived from observations at other wavelengths. This residual component, also fit iteratively, was derived by deconvolving the residuals to take into account the effects of the PSF, filtering the result to reduce statistical fluctuations (removing structures on angular scales smaller than ∼2°). The spectrum was modeled as inverse Compton emission from a population of cosmic-ray electrons with a spectral break at 965 MeV.

2.3.2. Isotropic Background

The isotropic diffuse background was derived from all-sky fits of the 4 yr data set using the Galactic diffuse emission model described above and a preliminary version of the 3FGL source list. The diffuse background includes charged particles misclassified as γ-rays. We implicitly assume that the acceptance for these residual charged particles is the same as for γ-rays in treating these diffuse background components together. For the analysis we derived the contributions to the isotropic background separately for *Front*-converting and *Back*-converting events. They are available as `iso_sour-ce_xxx_v05.txt` from the FSSC, where `xxx` is `front` or `back`.

2.3.3. Solar and Lunar Template

The quiescent Sun and the Moon are fairly bright γ-ray sources (Abdo et al. 2011b, 2012b). The Sun moves in the ecliptic, but the solar γ-ray emission is extended because of cosmic-ray interactions with the solar radiation field; detectable emission from inverse Compton scattering of cosmic-ray electrons on the radiation field of the Sun extends several degrees from the Sun (Abdo et al. 2011b). The Moon is not an extended source in this way, but the lunar orbit is inclined somewhat relative to the ecliptic, and the Moon moves through a larger fraction of the sky than the Sun. Averaged over time, the γ-ray emissions from the Sun and Moon trace a region around the ecliptic. We used models of their observed emission together with calculations of their motions and of the exposure

---

[78] Details about the performance of the LAT are available at http://www.slac.stanford.edu/exp/glast/groups/canda/lat_Performance.htm.

[79] See http://galprop.stanford.edu.

[80] The model is available as `gll_iem_v05_rev1.fit` from the FSSC.

of the observations by the LAT to make templates for the equivalent diffuse component for the 3FGL analysis using *gtsuntemp* (Johannesson & Orlando 2013). For the light curves (Section 3.6) we evaluated the equivalent diffuse components for the corresponding time intervals.

2.3.4. Residual Earth Limb Template

The limb of the Earth is an intense source of γ-rays from cosmic-ray collisions with the upper atmosphere (Abdo et al. 2009a). At the ∼565 km altitude of the (nearly circular) orbit of the LAT, the limb is ∼112° from the zenith. During survey-mode observations, which predominated in the first 4 yr of the *Fermi* mission, the spacecraft was rocked toward the northern and southern orbital poles on alternate ∼90-minute orbits. With these attitudes, the edge of the LAT field of view closest to the orbital poles generally subtended part of the Earth limb. As described in Section 2.2, we limited the data selection and exposure calculations to zenith angles less than 100°. Because the Earth limb emission is so intense and the tails of the LAT PSF are long (Ackermann et al. 2012a), a residual component of limb emission remained in the data. Over the course of a precession period of the orbit (∼53 days), the residual glow fills out large "caps" around the celestial poles, with the angular radius determined by the sum of the orbital inclination (25°.6) and the angular distance of the zenith angle limit from the orbital pole (10°). Casandjian & the Fermi LAT Collaboration (2015) describe how the map and spectrum of the residual component were derived. The spectrum is well modeled as a steep power law in energy with index 4.25. This is steep enough that the residual Earth limb emission contributes significantly only below 300 MeV.

3. CONSTRUCTION OF THE CATALOG

The procedure used to construct the 3FGL catalog has a number of improvements relative to what was implemented for the 2FGL catalog. In this section we review the procedure, with an emphasis on what is being done differently. The significances (Section 3.2), spectral parameters (Section 3.3), and fluxes (Section 3.5) of all catalog sources were obtained using the standard *pyLikelihood* framework (Python analog of *gtlike*) in the LAT Science Tools[81] (version v9r32p5). The localization procedure (Section 3.1), which relies on *pointlike*, provided the source positions, the starting point for the spectral fitting, and a comparison for estimating the reliability of the results (Section 3.7.4). Throughout the text we use the test statistic TS = $2\Delta \log \mathcal{L}$ for quantifying how significantly a source emerges from the background, comparing the likelihood function $\mathcal{L}$ with and without that source.

3.1. Detection and Localization

This section describes the generation of a list of candidate sources, with locations and initial spectral fits, for processing by the standard LAT science analysis tools, especially *gtlike* to compute the likelihood (Section 3.2). This initial stage uses instead *pointlike* (Kerr 2010). Compared with the *gtlike*-based analysis described in Sections 3.2–3.7, it uses the same data, exposure, and IRFs, but the partitioning of the sky, the computation of the likelihood function, and its optimization are independent. Since this version of the computation of the

likelihood function is used for localization, it needs to represent a valid estimate of the probability of observing a point source with the assumed spectral function.

The process started with an initial set of sources from the 2FGL analysis: not just those reported in that catalog, but also including all candidates failing the significance threshold (i.e., with TS < 25). It also used the latest extended source list with 25 entries (Section 3.4) and the three-source representation of the Crab (Section 3.3). The same spectral models were considered for each source as in Section 3.3, but the favored model (power law or curved) was not necessarily the same.

Many details of the processing were identical to the 2FGL procedure: using HEALPix[82] (Górski et al. 2005) with N_{side} = 12, to tile the sky, resulting in 1728 tiles of ∼25 deg² area; optimizing spectral parameters for the sources within each tile, for the data in a cone of 5° radius about the center of the tile; and including the contributions of all sources within 10° of the center. The tiles are of course discrete, but the regions, which we refer to as RoIs, for Regions of Interest, are overlapping and not independent. The data were binned in energy (14 energy bands from 100 MeV to 316 GeV) and position, where the angular bin size (the bins also defined using HEALPix) was set to be small compared with the PSF for each energy and event type. Separating the photons according to event type is important, especially for localization, since the *Front*-converting events have a factor of two narrower PSF core than the *Back*-converting events. Thus, the parameter optimization was performed by maximizing the logarithm of the likelihood, expressed as a sum over each energy band and each of the two event types (*Front*, *Back*). The fits for each RoI, maximizing the likelihood as a function of the free parameters, were performed independently. Correlations between sources in neighboring RoIs were then accounted for by iterating all 1728 fits until the changes in the log likelihoods for all RoIs were less than 10.

After a set of iterations had converged, then the localization procedure was applied and source positions updated for a new set of iterations. At this stage, new sources were occasionally added using the residual TS procedure described below. The detection and initial localization process resulted in 4029 candidate point sources with TS > 10.

New features that are discussed below include an assessment of the reliability of each spectral fit and of the model as a whole in each RoI, a different approach to the normalization of the Galactic diffuse background component, and a method to unweight the likelihood to account for the effect of potential systematic errors in the Galactic diffuse emission on source spectra.

3.1.1. Fit Validation

An important criterion is that not only are the spectral and spatial models for all sources optimized, but the predictions of the models are consistent with the data. Maximizing the likelihood as an estimator for spectral parameters and position is valid only if the likelihood, given a set of parameters, corresponds to the probability of observing the data. We have three measures.

The first compares the number of counts in each energy band, combining *Front* and *Back*, for each of the 1728 regions, defining a χ^2-like measure as the sum of the squares of the deviations divided by the predicted number of counts. The

---

[81] See http://fermi.gsfc.nasa.gov/ssc/data/analysis/documentation/Cicerone/.
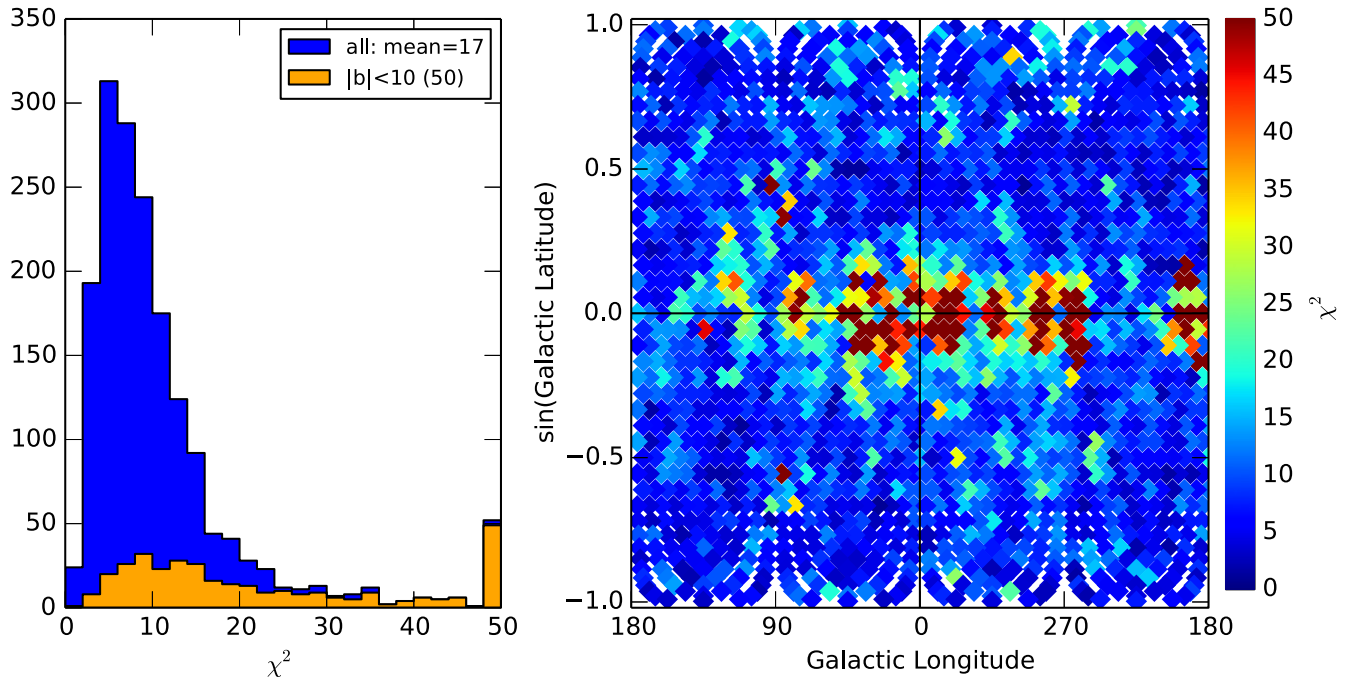
[82] http://healpix.sourceforge.net.

Figure 2. Distributions of the χ^2 measure of consistency of the measured spectrum of each RoI with the model (capped at 50). Left: histogram highlighting the low-latitude subset. Right: distribution of the values over the sky.

number of counts is the expected variance for Poisson counting statistics. This measure is of course only a component of the likelihood and depends only weakly on most of the point sources. That is, maximizing the likelihood does not necessarily minimize this quantity. But it is important to check the reliability of the diffuse model used, since this can distort the point-source spectral fits. Figure 2 shows the distribution of that χ^2-like measure and its values as a function of location on the sky. The number of degrees of freedom is 14 (the number of energy bands) minus the effective number of variables. The fact that the distribution peaks at $\simeq 9$ seems sensible. The ~ 35 regions with $\chi^2 > 50$ indicate problems with the model. Most are close to the Galactic plane, indicating difficulty with the component representing the Galactic diffuse emission. The few at high latitudes could be due to missing sources or, for very strong sources, inadequacy of the simple spectral models that we use.

The second measure is a check that the spectral model for each source is consistent with the data. The likelihood associated with a source is the product of the likelihoods for that source for each energy band, including the contributions of nearby, overlapping sources, and the diffuse backgrounds. The correlations induced by those are only relevant for the lower energies, typically below 1 GeV. For this analysis, we keep these contributions fixed. We form the spectral fit quality as $2\log(\mathcal{L}_{\mathrm{bands}}/\mathcal{L}_{\mathrm{fit}})$, where the flux for each band is optimized independently in $\mathcal{L}_{\mathrm{bands}}$, whereas the spectral model is applied in $\mathcal{L}_{\mathrm{fit}}$. The spectrum in Figure 3 illustrates the concept.

In Figure 4, we show the distribution of the spectral fit quality for all preliminary spectra, with separate plots for the three different spectral functions (Section 3.3): power law, lognormal, and power law with an exponential cutoff. The latter, applied almost exclusively to pulsars, is separated into sources in and out of the Galactic plane. It is seen that sources in the plane often have poorer fits. All are compared with an example χ^2 distribution with 10 degrees of freedom. There are
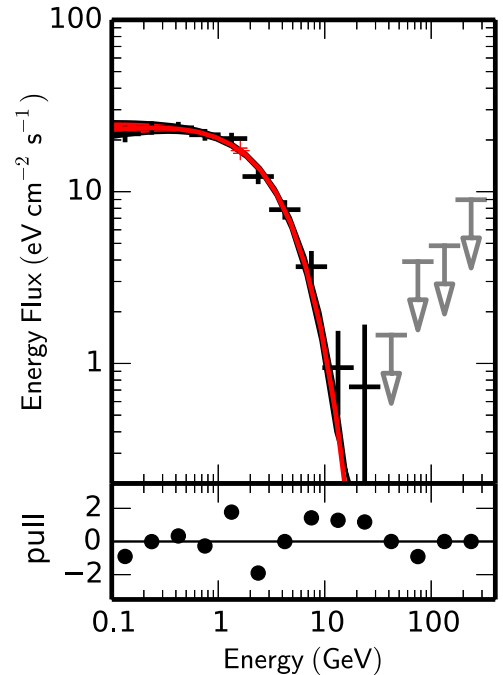

Figure 3. Spectral energy distribution for a typical source, in this case PSR J1459−6053, as measured by the *pointlike* analysis. The lower plot shows the *pulls*, defined as the square root of the difference $2\Delta\log\mathcal{L}$ between the fitted flux and the spectral model in each energy band, signed with the residual. The points with error bars reflect the dependence of the likelihood on the flux for each energy band, combining *Front* and *Back*, while the curve is the result of the fit to all the energy bands.

14 bands, and two to four parameters, but the higher-energy bands often do not contribute, so the number of degrees of freedom is not well defined, and we use 10 for illustration only.
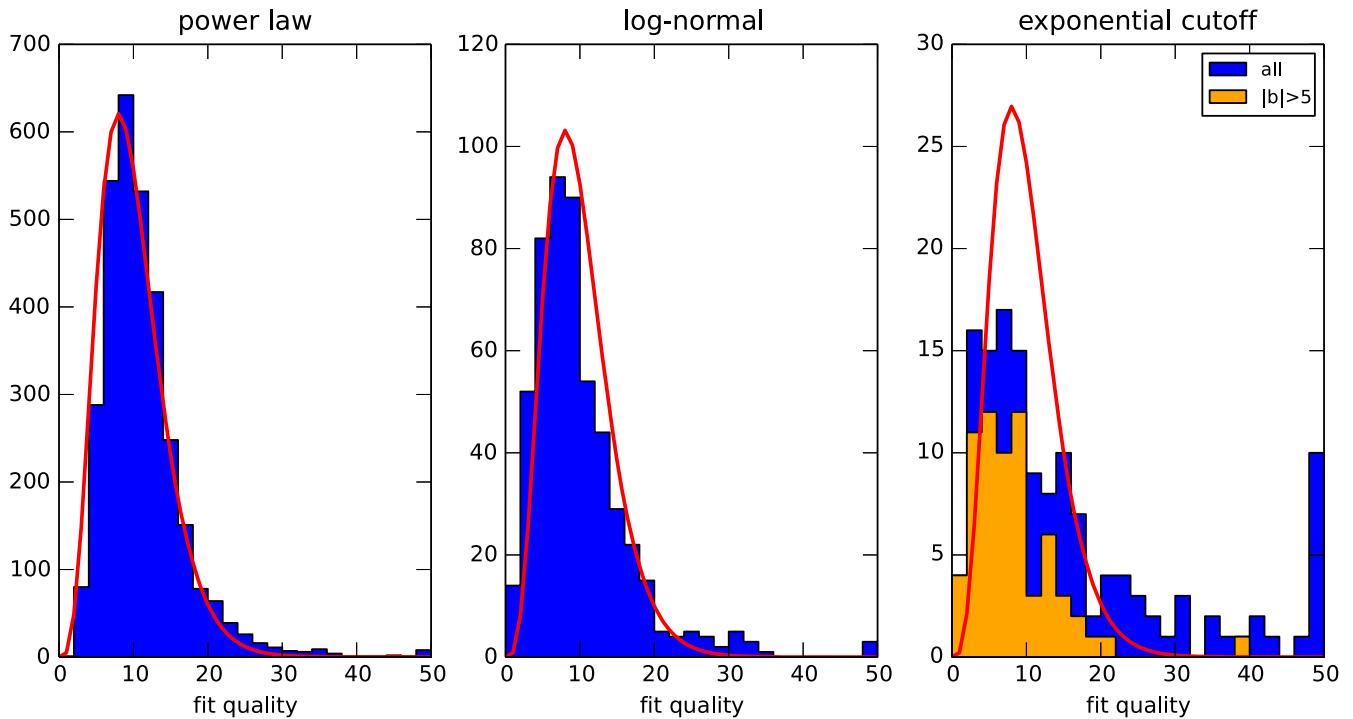
Figure 4. Distributions of the spectral fit quality (capped at 50). Left: sources fit with a power-law spectrum; center: sources fit with a log normal; right: sources fit with a power law with exponential cutoff. All are overlaid with the χ^2 distribution with 10 degrees of freedom.

Finally, the localization process fits the logarithm of the likelihood as a function of position to a quadratic form and checks the consistency with a χ^2-like measure (Section 3.1.3).

3.1.2. Galactic Diffuse Normalization and Unweighting

The model that we used for the Galactic diffuse background is a global fit using the data, as described in Section 2.3. For an individual RoI, however, we found that we needed to adjust the normalizations for each band to fit the data. For the relatively broad energy bands, four per decade, used in the *pointlike* fit we allow the normalization for each band to vary, effectively ignoring the spectral prediction of the diffuse component analysis. So, for each of the 1728 RoIs, and for each of the eight energy bands below 10 GeV, we measured a normalization factor, which applies to both *Front* and *Back*, by maximizing the likelihood with respect to it. A motivation for this procedure was that, for the lowest energy bands, it often improved the fit consistencies of the spectral models of the sources in the same RoI.

While the precision of the determination of the average contribution from the Galactic diffuse for an energy band is subject to only the statistics of the number of photons, the value of the Galactic diffuse intensity at the location of each source, that is, the angular distribution of the intensity, is subject to an additional systematic error. Since this intensity is strongly correlated with the measurement of the flux from the source itself, and the correlation can be very significant for weak sources, we have adopted an ad hoc but conservative procedure to account for the additional uncertainty by increasing the width of the log likelihood distribution from each energy band according to how sensitive it is to the Galactic diffuse contribution. This is accomplished by dividing the log likelihood by $\max(1, N_{\mathrm{diff}}/1000)$, where N_{diff} is the predicted number of Galactic diffuse photons in the RoI. This has the effect of limiting the precision to the statistics of 1000 photons in the RoI and energy band, i.e., it unweights contributions from energy ranges for which the contribution from the diffuse component is relatively less well defined.

3.1.3. Localization

The position of each source was determined by maximizing the likelihood with respect to its position only. That is, all other parameters are kept fixed. The possibility that a shifted position would affect the spectral models or positions of nearby sources is accounted for by iteration. Ideally, the likelihood is the product of two Gaussians in two orthogonal angular variables. Thus, the log likelihood is a quadratic form in any pair of angular variables, assuming small angles. We define LTS, for Localization test statistic, to be twice the log of the likelihood ratio (LR) of any position with respect to the maximum; the LTS evaluated for a grid of positions is called an LTS map. We fit the distribution of LTS to a quadratic form to determine the uncertainty ellipse, the major and minor axes, and orientation. We also define a measure, the localization quality (LQ), of how well the actual LTS distribution matches this expectation by reporting the sum of the squares of the deviations of eight points evaluated from the fit at a circle of radius corresponding to twice the geometric mean of the two Gaussian sigmas. Figure 5 shows examples of localization regions for point sources. The distribution of the LQ is shown in Figure 6.

An important issue is how to treat apparently significant sources that do not have good localization fits, which we defined as LQ > 8. An example is shown in Figure 5 (right). We flagged such sources (Flag 9 in Table 3) and for them estimated the position and uncertainty by performing a moment analysis of the LTS function instead of fitting a quadratic form. Some sources that did not have a well-defined peak in the likelihood were discarded by hand, on the consideration that
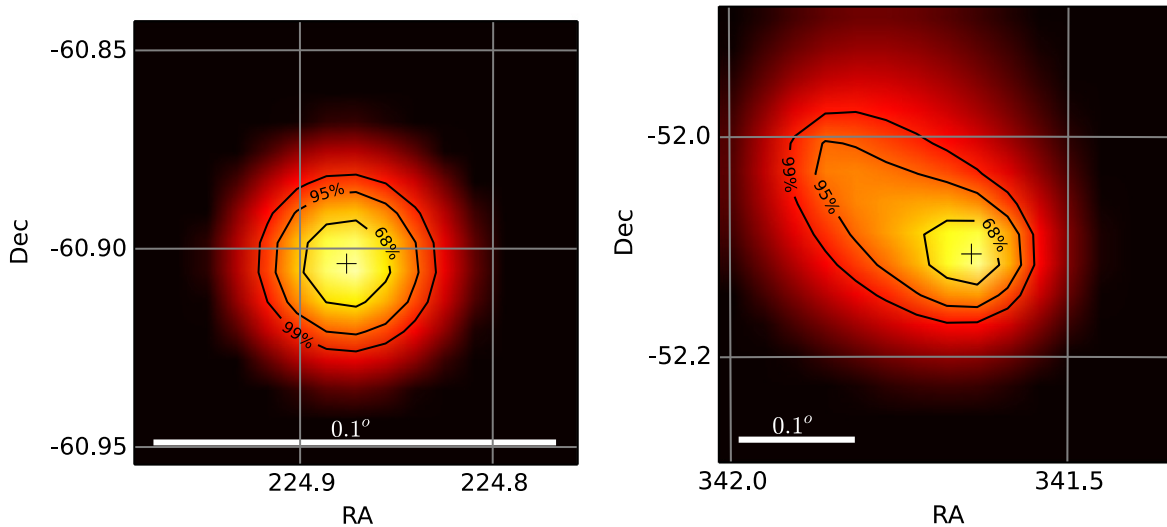
Figure 5. Examples of localization TS maps. The contours for 68%, 95%, and 99% containment are shown. The scale (in decimal degrees) is not the same in both plots. Left: PSR J1459−6053, a good localization with LQ = 0.63. Right: 3FGL J2246.7−5205, a bad localization with LQ = 14.
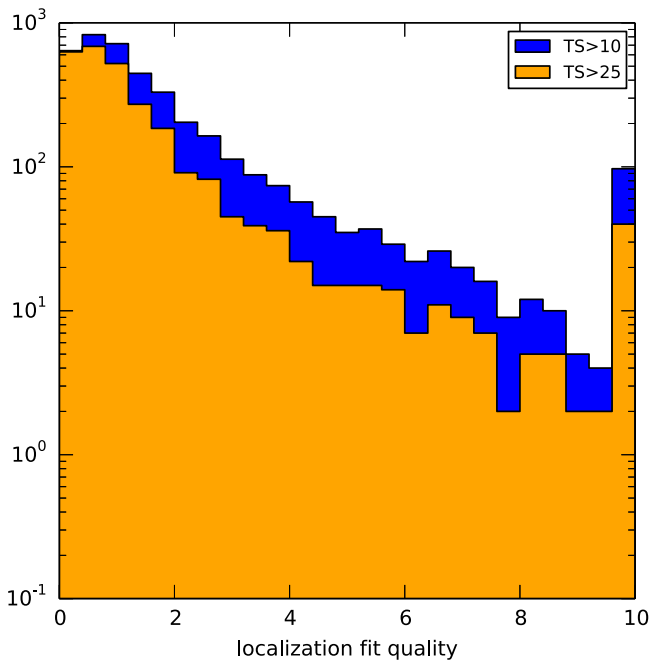

Figure 6. Distribution, in the preliminary source list, of the localization quality LQ (capped at 10).

they were most likely related to residual diffuse emission. Another possibility is that two nearby sources produce a dumbbell-like shape; for some of these cases we added a new source by hand. A final selection demanding that the semimajor radius (1σ) be less than $0°25$ resulted in 3976 candidate sources, of which 142 were localized using the moment analysis.

As in 1FGL and 2FGL, we compared the localizations of the brightest sources with associations with their true positions in the sky. This indicated that the absolute precision is still the same, $\sim0°005$ at the 95% confidence level. After the associations procedure (Section 5.2), we compared the distribution of distances to the high-confidence counterparts (in units of the estimated 1σ errors) with a Rayleigh distribution and noted that it was slightly broader, by a factor

of 1.05 (smaller than the 1.1 factor used in 1FGL and 2FGL). Consequently, we multiplied all error estimates by 1.05 and added $0°005$ in quadrature to both 95% ellipse axes. The resulting comparison with the Rayleigh distribution is shown in Figure 3 of Ackermann et al. (2014, 3LAC) and indicates good agreement.

3.1.4. Detection of Additional Sources

We used the *pointlike* definition of likelihood itself to detect sources that needed to be added to the model of the sky. Using HEALPix with $N_{side} = 512$, we defined 3.2 M pixels in the sky, separated by $\simeq0°15$, then evaluated the improvement in the likelihood from adding a new point source at the center of each, assuming a power-law spectrum with index 2.2. The TS value for each attempt, assigned to the pixel, defines a residual TS map of the sky. Next we performed a cluster analysis for all pixels with TS > 10, determining the number of pixels, the maximum TS, and the TS-weighted centroid. All such clusters with at least two pixels were added to a list of seeds. Then each seed was reanalyzed, now allowing the spectral index to vary, with a full optimization in the respective RoI, and then localized. The last step was to add all such refit seeds, if the fits to the spectrum and the position were successful, and TS > 10, as new sources, for a final optimization of the full sky.

3.2. Significance and Thresholding

The framework for this stage of the analysis is inherited from the 2FGL catalog. It splits the sky into RoIs, varying typically half a dozen sources near the center of the RoI at the same time. There were 840 RoIs for 3FGL, listed in the ROIs extension of the catalog (Appendix A). The global best fit is reached iteratively, injecting the spectra of sources in the outer parts of the RoI from the previous step. In that approach the diffuse emission model (Section 2.3) is taken from the global templates (including the spectrum, unlike what is done with *pointlike* in Section 3.1), but it is modulated in each RoI by three parameters: normalization and small corrective slope of the Galactic component and normalization of the isotropic component. Appendix A shows how those parameters vary over the sky.

Among more than 4000 seeds coming from the localization stage, we keep only sources at TS > 25, corresponding to a significance of just over 4σ evaluated from the χ^2 distribution with 4 degrees of freedom (position and spectral parameters, Mattox et al. 1996). The model for the current RoI is readjusted after removing each seed below threshold, so that the final model fits the full data. The low-energy flux of the seeds below threshold (a fraction of which are real sources) can be absorbed by neighboring sources closer than the PSF radius. There is no pair of seeds closer than 0°.1, so the neighbors are unaffected at high energy. The fixed sources outside the core of the RoI are not tested and therefore not removed during the last fit of an RoI. Since the TS threshold at the previous step was set to 16, seeds with 16 < TS < 25 still populate the outer parts of the RoI, preventing the background level from rising (bullet 5 below).

We introduced a number of improvements with respect to 2FGL (by decreasing order of importance):

1. After 2FGL was completed, we understood that it was important to account for the different instrumental backgrounds in *Front* and *Back* events (Section 2.3). Implicitly assuming that they were equal as in 2FGL resulted in lower TS (fewer sources) and tended to underestimate the low-energy flux. The impact is largest at high latitude. We used different isotropic spectral templates for *Front* and *Back* events but a common renormalization parameter. We also used different *Front* and *Back* models of the Earth limb. The same distinction was introduced for computing the fluxes per energy band (Section 3.5) and per month (Section 3.6).

2. Another effect discovered after 2FGL was a slight inconsistency (8% at 100 MeV) between the *Front* and *Back* effective areas. This affected mostly the Galactic plane, where the strong interstellar emission makes up 90% of the events. That effect created opposite low-energy residuals in *Front* and *Back* that did not compensate each other because of the differing PSF. It was corrected empirically in the P7REP_SOURCE_V15 version of the IRFs (Bregeon et al. 2013).

3. We put in place an automatic iteration procedure at the next-to-last step of the process checking that the all-sky result is stable (2FGL used a fixed number of five iterations), similar to what was done for localization in 2FGL. Quantitatively, we iterated an RoI and its neighbors until log $\mathcal{L}$ did not change by more than 10. In practice, this changes nothing at high latitude but improves convergence in the Galactic plane. Fifteen iterations were required to reach full convergence. That iteration procedure was run twice, allowing sources to switch to a curved spectral shape (Section 3.3) after the first convergence.

4. The software issue that prevented using unbinned likelihood in 2FGL was solved. We took advantage of that by using unbinned likelihood at high energy where keeping track of the exact direction of each event helps. At low energy we used binned likelihood in order to cap the memory and CPU resources. The dividing energy was set to 3 GeV, resulting in data cubes (below 3 GeV) and event lists (above 3 GeV) of approximately equal size. Both data sets were split between *Front* and *Back*. This was implemented in the *SummedLikelihood* framework of *pyLikelihood*. In binned mode, the pixel size was set to

0°.2 and 0°.3 for *Front* and *Back* events, respectively (at 3 GeV the FWHM of the PSF is 0°.25 and 0°.38, respectively). The energy binning was set to 10 bins per decade as in 2FGL. In the exposure maps for unbinned mode, the pixel size was set to 0°.1 (even though the exposure varies very slowly, this is required to model precisely the edge of the field of view).

5. We changed the criterion for including sources outside the RoI in the model. We replaced the flat 7° distance threshold by a threshold on contributed counts (predicted from the model at the previous step). We kept all sources contributing more than 2% of the counts per square degree in the RoI. This is a good compromise between reliability and memory/CPU requirements and accounts for bright sources even far outside the RoI (at 100 MeV the 95% containment radius for *Back* events is 14°). Compared to 2FGL, that new procedure affects mostly high latitudes (where the sources make up a larger fraction of the diffuse emission). Because it brings more low-energy events from outside in the model, it tends to reduce the fitted level of the low-energy diffuse emission, resulting in slightly brighter and softer source spectra.

6. The fits are now performed up to 300 GeV, and the overall significances (Signif_Avg) and the spectral parameters refer to the full 100 MeV–300 GeV band.

7. We introduced explicitly the model of the Sun and Moon contributions (Section 2.3), without any adjustment or free parameter in the likelihood analysis. The success of that procedure is illustrated in Figures 7 and 10.

8. For homogeneity (so that the result does not depend on which spectral model we start from) the TS > 25 threshold was always applied to the power-law model, even if the best-fit model was curved. There are 21 sources in 2FGL with TS − TS$_{\rm curve}$ < 25, which would not have made it with this criterion (see Section 3.3 for the definition of TS$_{\rm curve}$).

3.3. Spectral Shapes

The spectral representation of sources was mostly the same as in 2FGL. We introduced an additional parameter modeling a super- or subexponentially cutoff power law, as in the pulsar catalog (Abdo et al. 2013). However, this was applied only to the brightest pulsars (PSR J0835−4510 in Vela, J0633+1746, J1709−4429, J1836+5925, J0007+7303). The global fit with nearby sources was too unstable for the fainter ones, which were left with a simple exponentially cutoff power law. The subexponentially cutoff power law was also adopted for the brightest blazar 3C 454.3.[83] The fit was very significantly better than with either a lognormal or a broken power-law shape. Even though bright sources are not a scientific objective of a catalog, avoiding low-energy spectral residuals (which translate into spatial residuals because of the broad PSF) is important for nearby sources.

Therefore, the spectral representations that can be found in 3FGL are:

1. A lognormal representation (LogParabola in the tables) for all significantly curved spectra except pulsars

---

[83] That is only a mathematical model; it should not be interpreted in a physical sense since it is an average over many different states of that very variable object.
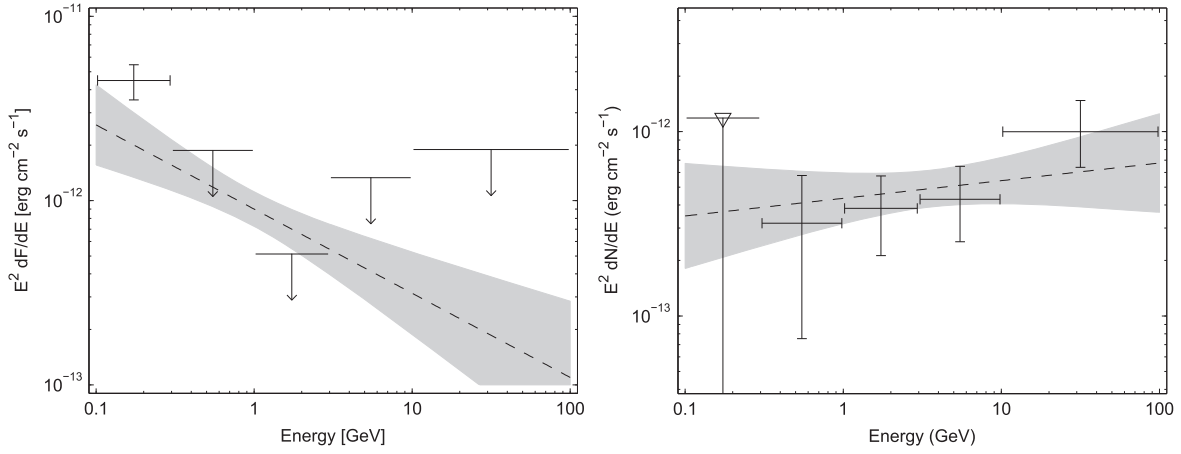
Figure 7. Spectral energy distribution of the same source (the BL Lac TXS 0836+182) as 2FGL J0839.4+1802 (left) and 3FGL J0839.6+1803 (right). This source was flagged as "possibly due to the Sun" (Flag 11 in Table 3) in 2FGL. Entering the Sun and Moon into the background model has reduced to zero the low-energy signal that drove the 2FGL fit, resulting in a hard source in 3FGL. The dashed line is the best fit over the full energy range (Section 3.2), and the grayshaded area is the statistical uncertainty around the best fit (for a given spectral form). The vertical scale is not the same in the left and right plots. Note that the 300 MeV–1 GeV point has (asymmetric) error bars in 3FGL as explained in Section 3.5 even though its significance is less than 2σ. Upper limits (indicated by a downward triangle in 3FGL and a downward arrow in 2FGL) are at 95% confidence level.

and 3C 454.3:

$$\frac{dN}{dE} = K \left(\frac{E}{E_0} \right)^{-\alpha - \beta \, \log\left(E/E_0 \right)}, \tag{1}$$

where log is the natural logarithm. The reference energy E_0 is set to `Pivot_Energy` in the tables. The parameters K, α (spectral slope at E_0), and the curvature β appear as `Flux_Density`, `Spectral_Index`, and `beta` in the tables, respectively. No negative β (spectrum curved upward) was found. The maximum allowed β was set to 1 as in 2FGL.

2. An exponentially cutoff power law for all significantly curved pulsars and a super- or subexponentially cutoff power law for the bright pulsars and 3C 454.3 (`PLExpCutoff` or `PLSuperExpCutoff` in the tables, depending on whether b was fixed to 1 or left free):

$$\frac{dN}{dE} = K \left(\frac{E}{E_0} \right)^{-\Gamma} \exp\left(\left(\frac{E_0}{E_c} \right)^b - \left(\frac{E}{E_c} \right)^b \right), \tag{2}$$

where the reference energy E_0 is set to `Pivot_Energy` in the tables and the parameters K, Γ (low-energy spectral slope), E_c (cutoff energy), and b (exponential index) appear as `Flux_Density`, `Spectral_Index`, `Cutoff`, and `Exp_Index` in the tables, respectively. Note that this is not the way that spectral shape appears in the Science Tools (no $(E_0/E_c)^b$ term in the exponential), so the error on K in the tables was obtained from the covariance matrix. The minimum Γ was set to 0.5 (in 2FGL it was set to 0).

3. A simple power-law form for all sources not significantly curved.

As in 2FGL, a source is considered significantly curved if $\mathrm{TS_{curve}} > 16$, where $\mathrm{TS_{curve}} = 2(\log \mathcal{L}(\text{curved spectrum}) - \log \mathcal{L}(\text{power-law}))$. The curved spectrum is `PLExpCutoff` (or `PLSuperExpCutoff`) for pulsars and 3C 454.3,

`LogParabola` for all other sources. The curvature significance is reported as `Signif_Curve` (see Section 3.5).

Another difference with 2FGL is that the complex spectrum of the Crab was represented as three components:

1. A `PLExpCutoff` shape for the pulsar, with free K, Γ, and E_c.
2. A soft power-law shape for the synchrotron emission of the nebula, with free K and Γ since the synchrotron emission is variable (Abdo et al. 2011c). The synchrotron component is called 3FGL J0534.5+2201s.
3. A hard power-law shape for the inverse Compton emission of the nebula, with parameters fixed to those found in Abdo et al. (2010e). That component does not vary, and leaving it free made the fit unstable. It is called 3FGL J0534.5+2201i.

In 2FGL, two sources (MSH 15−52 and Vela X) spatially coincident with pulsars had trouble converging, and their spectra were fixed to the result of the dedicated analysis (Abdo et al. 2010a, 2010g). In 3FGL the spectra of five sources were fixed for the same reason: the same two, the inverse Compton component of the Crab Nebula, the Cygnus X cocoon (Ackermann et al. 2011a), and the γ-Cygni supernova remnant (SNR). The spatial template of γ-Cygni was taken from Lande et al. (2012) as in 1FHL. We did not switch to the more complex spatial template used in Ackermann et al. (2011a), but the spectral template was obtained from a reanalysis of the Cygnus region including the Cygnus X cocoon (L. Tibaldo 2015, private communication).

Overall in 3FGL six sources (the five brightest pulsars and 3C 454.3) were fit as `PLSuperExpCutoff` (with b of Equation (2) < 1), 110 pulsars were fit as `PLExpCutoff`, 395 sources were fit as `LogParabola`, and the rest (including the five fixed sources) were represented as power laws.

3.4. Extended Sources

As for the 2FGL and 1FHL catalogs, we explicitly model as spatially extended those LAT sources that have been shown in dedicated analyses to be resolved by the LAT. Twelve extended sources were entered in the 2FGL catalog. That

number grew to 22 in the 1FHL catalog. The spatial templates were based on dedicated analysis of each source region and have been normalized to contain the entire flux from the source (>99% of the flux for unlimited spatial distributions such as 2D Gaussians). The spectral form chosen for each source is the best adapted among those used in the catalog analysis (see Section 3.3). Three more extended sources have been reported since then and were included in the same way in the 3FGL analysis.[84]

The catalog process does not involve looking for new extended sources or testing possible extension of sources detected as point-like. This was last done comprehensively by Lande et al. (2012) based on 1FGL. The extended sources published since then were the result of focused studies, so there most likely remain unreported faint extended sources in the *Fermi*-LAT data set. The process does not attempt to refit the spatial shape of known extended sources either.

The extended sources include 12 SNRs, nine pulsar wind nebulae (PWNe) or candidates, the Cygnus X cocoon, the Large and Small Magellanic Clouds (LMC and SMC), and the lobes of the radio galaxy Centaurus A. Below we provide notes on new sources and changes since 2FGL:

1. HB 21 is an SNR recently reported as an LAT source (Reichardt et al. 2012). We added it to the list, using the simple disk template and `LogParabola` spectral shape derived by Pivato et al. (2013).
2. HESS J1303−631 and HESS J1841−055 are two H.E.S.S. sources (most likely PWNe) recently reported as faint hard LAT sources by Acero et al. (2013). We added them to the list, using the original H.E.S.S. template rather than the best spatial fit to the LAT data, in keeping with the spectral analysis in that paper.
3. We changed the spectral representation of the LMC and the Cygnus Loop from `PLExpCutoff` to `LogParabola`, which fits the data better. The curvature of the fainter SMC spectrum is not significant; therefore, it was fit as a power law.

In general, we did not allow any point source inside the extended templates, even when the TS maps indicated that adding new seeds would improve the fit. Most likely (pending a dedicated reanalysis) those additional seeds were simply residuals due to the fact that the very simple geometrical representations that we adopted are not precise enough, rather than independent point sources. We preferred not splitting the source flux into pieces. The only exceptions are 3FGL J1823.2−1339 within HESS J1825−137, 3FGL J2053.9+2922 inside the Cygnus Loop, 3FGL J0524.5−6937 inside the LMC, and sources inside the Cygnus X cocoon. The first one is as significant as the extended source and was a 2FGL source already. The next two are well localized over large extended sources and show a very hard spectrum, so they do not impact the spectral characteristics of the extended sources. The Cygnus X cocoon was fixed (Section 3.3), and allowing point sources on top of it was necessary to reach a reasonable representation of the region.

Table 1 lists the source name, spatial template description, spectral form, and the reference for the dedicated analysis. These sources are tabulated with the point sources, with the only distinction being that no position uncertainties are

reported and their names end in `e` (see Section 4.1). Unidentified point sources inside extended ones are marked by "xxx field" in the `ASSOC2` column of the catalog.

3.5. Flux Determination

The source photon fluxes are reported in the same five energy bands (100–300 MeV, 300 MeV–1 GeV, 1–3 GeV, 3–10 GeV, 10–100 GeV) as in 2FGL. The fluxes were obtained by freezing the spectral index to that obtained in the fit over the full range and adjusting the normalization in each spectral band. For the curved spectra (Section 3.3) the spectral index in a band was set to the local spectral slope at the logarithmic mid-point of the band $\sqrt{E_n E_{n+1}}$, restricted to be in the interval [0, 5]. The photon flux between 1 and 100 GeV and the energy flux between 100 MeV and 100 GeV (F_{35} and S_{25} in Table 5; the subscript ij indicates the energy range as 10^i–10^j MeV) are derived from the full-band analysis assuming the best spectral shape and their uncertainties from the covariance matrix. Even though the full analysis is carried out up to 300 GeV in 3FGL, we have not changed the energy range over which we quote fluxes, so that they can be easily compared with past fluxes. The photon flux above 100 GeV is negligible anyway, and the energy flux above 100 GeV is not precisely measured (even for hard sources).

Improvements with respect to the 2FGL analysis are as follows:

1. We used binned likelihood in the first three bands (up to 3 GeV) and unbinned likelihood in the last two bands, distinguishing *Front* and *Back* events. The pixel sizes in each band in binned mode were 0°.3 and 0°.5, 0°.2 and 0°.3, 0°.1 and 0°.15, where in each band the first value is for *Front*, the second one for *Back*. This reduces error bars by 10%–15% compared to mixing *Front* and *Back* events as in 2FGL.
2. Following what was done in the 1FHL catalog, the errors on the fluxes of moderately faint sources (TS ⩾ 1 in the band) were computed as 1σ errors with MINOS in the Minuit[85] package. This was done whenever the relative error on flux in the quadratic approximation (from the covariance matrix) was larger than 10%. Both errors (lower and upper) are reported in the FITS table (Appendix B). The lower error is reported with a minus sign (when the error comes from the quadratic approximation, the lower error is simply minus the upper error). The upper limits F_i^{UL} for very faint sources (TS < 1) were computed as in 2FGL, using the Bayesian method (Helene 1983) at 95% of the posterior probability. The upper error is then reported as $0.5(F_i^{UL} - F_i^{BF})$, where F_i^{BF} is the best-fit flux, and the lower error is set to NULL.
3. The same iteration procedure described in Section 3.2 was put in place for the fluxes per energy band using a more stringent criterion ($\Delta \log \mathcal{L} < 3$). Convergence was fast at high energy (little cross-talk between sources). It was a little slower at low energy (six iterations in the first band) but much faster than the full-band fit because no spectral adjustment was involved.
4. We report as `nuFnuxxx_yyy` the spectral energy distribution (SED) in the band defined by xxx–yyy MeV, which can be directly overlaid on an SED plot. The SED was obtained by dividing the energy flux in the band

---

[84] The templates and spectral models are available through the FSSC.

[85] http://lcgapp.cern.ch/project/cls/work-packages/mathlibs/minuit/home.html.

Table 1
Extended Sources Modeled in the 3FGL Analysis

3FGL Name	Extended Source	Spatial Form	Extent (deg)	Spectral Form	Reference
J0059.0−7242e	SMC	2D Gaussian	0.9	PowerLaw	Abdo et al. (2010b)
J0526.6−6825e	LMC	2D Gaussian[a]	1.2, 0.2	LogParabola	Abdo et al. (2010k)
J0540.3+2756e	S 147	Map	⋯	PowerLaw	Katsuta et al. (2012)
J0617.2+2234e	IC 443	2D Gaussian	0.26	LogParabola	Abdo et al. (2010j)
J0822.6−4250e	Puppis A	Disk	0.37	PowerLaw	Lande et al. (2012)
J0833.1−4511e	Vela X	Disk	0.88	PowerLaw	Abdo et al. (2010g)
J0852.7−4631e	Vela Junior	Disk	1.12	PowerLaw	Tanaka et al. (2011)
J1303.0−6312e	HESS J1303−631	2D Gaussian	0.16	PowerLaw	Aharonian et al. (2005)
J1324.0−4330e	Centaurus A (lobes)	Map	⋯	PowerLaw	Abdo et al. (2010c)
J1514.0−5915e	MSH 15−52	Disk	0.25	PowerLaw	Abdo et al. (2010a)
J1615.3−5146e	HESS J1614−518	Disk	0.42	PowerLaw	Lande et al. (2012)
J1616.2−5054e	HESS J1616−508	Disk	0.32	PowerLaw	Lande et al. (2012)
J1633.0−4746e	HESS J1632−478	Disk	0.35	PowerLaw	Lande et al. (2012)
J1713.5−3945e	RX J1713.7−3946	Map	⋯	PowerLaw	Abdo et al. (2011d)
J1801.3−2326e	W28	Disk	0.39	LogParabola	Abdo et al. (2010f)
J1805.6−2136e	W30	Disk	0.37	LogParabola	Ajello et al. (2012)
J1824.5−1351e	HESS J1825−137	2D Gaussian	0.56	LogParabola	Grondin et al. (2011)
J1836.5−0655e	HESS J1837−069	Disk	0.33	PowerLaw	Lande et al. (2012)
J1840.9−0532e	HESS J1841−055	2D Gaussian[b]	(0.41, 0.25)	PowerLaw	Aharonian et al. (2008)
J1855.9+0121e	W44	Ring[b]	(0.22, 0.14), (0.30, 0.19)	LogParabola	Abdo et al. (2010i)
J1923.2+1408e	W51C	Disk[b]	(0.40, 0.25)	LogParabola	Abdo et al. (2009b)
J2021.0+4031e	γ-Cygni	Disk	0.63	PowerLaw	Lande et al. (2012)
J2028.6+4110e	Cygnus X cocoon	2D Gaussian	2.0	PowerLaw	Ackermann et al. (2011a)
J2045.2+5026e	HB 21	Disk	1.19	LogParabola	Pivato et al. (2013)
J2051.0+3040e	Cygnus Loop	Ring	0.7, 1.6	LogParabola	Katagiri et al. (2011)

Note.
List of all sources that have been modeled as extended sources. The Extent column indicates the radius for disk sources, the dispersion for Gaussian sources, and the inner and outer radii for ring sources.
[a] Combination of two 2D Gaussian spatial templates.
[b] The shape is elliptical; each pair of parameters (a, b) represents the semimajor (a) and semiminor (b) axes.

by the bandwidth in natural logarithm log(yyy/xxx). Since the fit is performed on the flux only (no spectral freedom in each band), the relative error on the SED is the same as that on the corresponding flux.

As in 2FGL, we report in 3FGL a curvature significance Signif_Curve=$\sqrt{\text{TS}_{\text{curve}}\, R_{\text{syst}}}$ (in σ units) after approximately accounting for systematic uncertainties on effective area via

$$R_{\text{syst}} = \frac{\sum_i \left(F_i - F_i^{\text{PL}}\right)^2 \Big/ \left(\sigma_i^2 + \left(f_i^{\text{rel}} F_i^{\text{fit}}\right)^2\right)}{\sum_i \left(F_i - F_i^{\text{PL}}\right)^2 / \sigma_i^2}, \qquad (3)$$

where i runs over all bands, F_i^{PL} is the flux predicted by the power-law model, and F_i^{fit} is the flux predicted by the best-fit (curved) model in that band from the spectral fit to the full band. f_i^{rel} reflects the systematic uncertainty on effective area (Section 3.7). The values were set to 0.1, 0.05, 0.05, 0.05, 0.1 in our five bands (the fourth one went down from 0.08 in 2FGL, thanks to improved calibration). Equation (3) is not exactly the same formula used for 2FGL. In 2FGL F_i^{fit} would have been replaced by F_i^{PL}. The disadvantage of the previous estimate was that it capped Signif_Curve to rather low

values (below 15), resulting in a small dynamic range because the largest relative systematic errors are in the two extreme bands and in those bands the power-law fit can run way above the points (because the spectra are curved downward). Using the curved fit (closer to the points) to estimate the systematic errors is a more reasonable procedure and recovers a larger dynamic range (up to 85 in 3FGL).

As in 2FGL, we consider that only sources with Signif_Curve > 4 are significantly curved (at the 4σ level). When R_{syst} is small (bright source), it can happen that $\text{TS}_{\text{curve}} > 16$ (triggering a curved model following Section 3.3) but Signif_Curve < 4. The 43 such sources with LogParabola spectra (and two pulsars with PLExpCutoff spectra) but Signif_Curve < 4 could be power laws within systematic errors. Nevertheless, we do not go back to power-law spectra for those sources because they are better fit with curved models and power-law models would result in negative low-energy residuals, which might affect nearby sources. One of them is illustrated in Figure 8. All are bright sources with modest curvature.

Spectral fit quality (for Flag 10 in Table 3) is computed as in Equation (3) of Nolan et al. (2012, 2FGL) rather than as in Section 3.1.1. Among the 42 sources flagged because of a too large spectral fit quality, most show deviations at low energy and are in confused regions or close to a brighter neighbor, as in Figure 9.
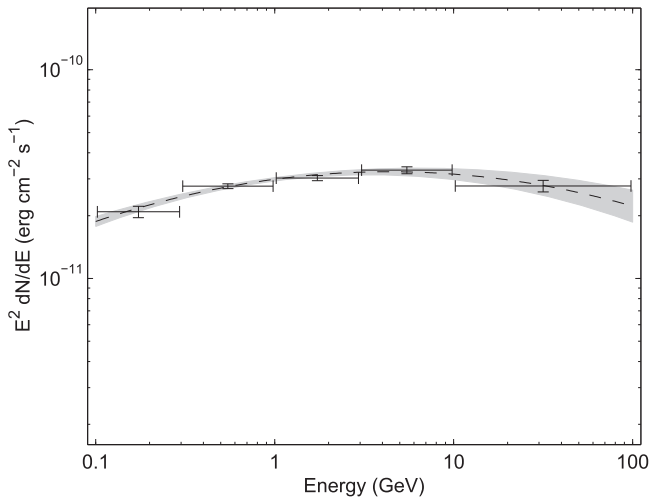
Figure 8. Spectral energy distribution of 3FGL J0222.6+4301 (3C 66A) fitted by a `LogParabola` spectrum with $\beta = 0.039 \pm 0.007$ but `Signif_Curve` (defined just before Equation (3)) = 2.81. The curvature is statistically significant, but a power law cannot be excluded given the range of the systematic errors on effective area.
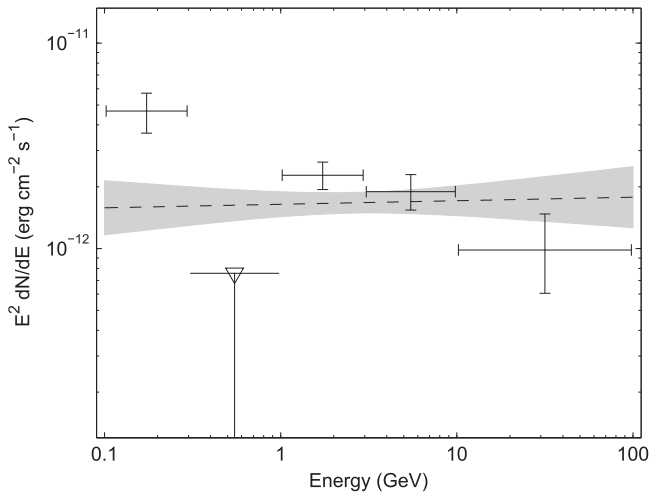

Figure 9. Spectral energy distribution of 3FGL J1226.9−1329 (PMN J1226 −1328) flagged with bad spectral fit quality (Flag 10 in Table 3). The first two points deviate from the power-law fit. This source is within 1°3 of the much brighter pulsar PSR J1231−1411, so it is confused with it (within r_{68}) below 600 MeV.

Spectral plots for all 3FGL sources overlaying the best model on the individual SED points are available from the FSSC.

3.6. Variability

The light curves were computed over the same (1 month) intervals as in 1FGL and 2FGL (there are now 48 points). The first 23 intervals correspond exactly to 2FGL. The fluxes in each bin were obtained by freezing the spectral parameters to those obtained in the fit over the full range and adjusting the normalization. We used unbinned likelihood over the full energy range for the light curves. Over short intervals it does not incur a large CPU or memory penalty and it preserves the full information. We used a different isotropic and Earth limb model for *Front* and *Back* events, as in the main fit (Section 3.2). We also used a different Sun/Moon model for
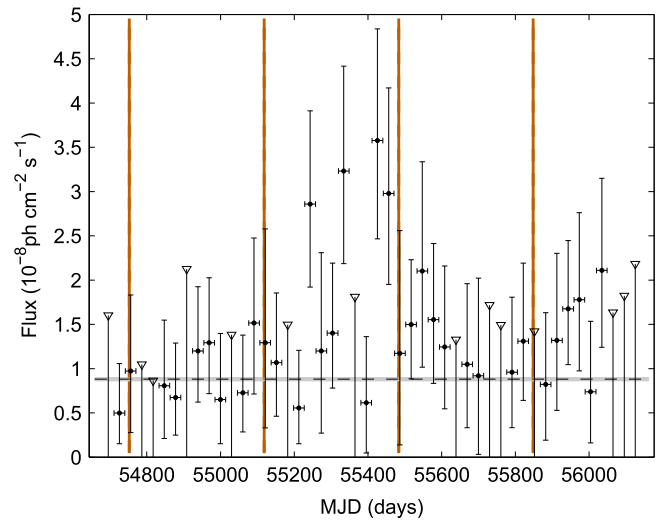

Figure 10. Light curve of 3FGL J1315.7−0732 (NVSS J131552−073301) in the ecliptic plane. That source is significantly variable. The flares do not correspond to the times when the Sun passed through the region (vertical orange bands). The only effect of the Sun passage is somewhat larger error bars. The gray shaded horizontal area materializes the systematic uncertainty of 2%. Upper limits (indicated by a downward triangle) are at 95% confidence level.

each month (the Sun is obviously at a different place in the sky each month). That improvement, together with our removing the solar flares, effectively mitigated the peaks that we noted in the 2FGL light curves due to the Sun passage near the source (Flag 11 in Table 3). We have not noted any obvious Sun-related peak in the 3FGL light curves (Figure 10).

As in the band flux calculation (Section 3.5), the errors on the monthly fluxes of moderately faint sources (TS > 1) were computed as lower and upper 1σ errors with MINOS in Minuit. Both errors (lower and upper) are reported in the FITS table (Table 16), so the `Unc_Flux_History` column is a 2×48 array. This allowed providing more information in the light-curve plots[86] by keeping points with error bars whenever TS > 1 (the lower error does not reach 0). When TS < 1, the 95% upper limit is converted into an upper error in the same way as in 2FGL and the band flux calculation.

We noted an inconsistency between the light curve and the flux from the main fit (over the full interval) in several extended sources, whereby the average of the light curve appears distinctly above the flux from the main fit. It is particularly obvious in Cen A lobes, HESS J1616−508 (Figure 11), S147, W28, and W30. We traced the problem to the fact that we used unbinned likelihood over the whole energy range for the light curves but binned likelihood for the main fit below 3 GeV. We have not found any evidence that this affects the point sources. Since we do not expect variability in extended sources, we left this inconsistency in the catalog as a known feature.

The variability indicator `Variability_Index` is the same as in 2FGL, with the same relative systematic error of 2%. Variability is considered probable when `Variabili-ty_Index` exceeds the threshold of 72.44 corresponding to 99% confidence in a χ^2 distribution with 47 degrees of freedom.

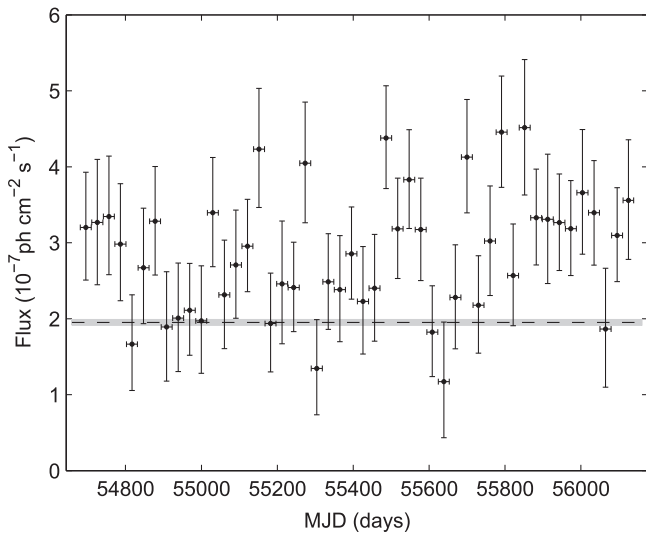[86] These plots are available from the FSSC.

Figure 11. Light curve of 3FGL J1616.2−5054e (HESS J1616−508). That is an extended source that should not be variable. Indeed the monthly fluxes are compatible with a constant, but not with the flux extracted over the full 4 yr (dashed line with gray shaded uncertainty). That inconsistency is due to a remaining difference between binned and unbinned likelihood fits affecting only extended sources.
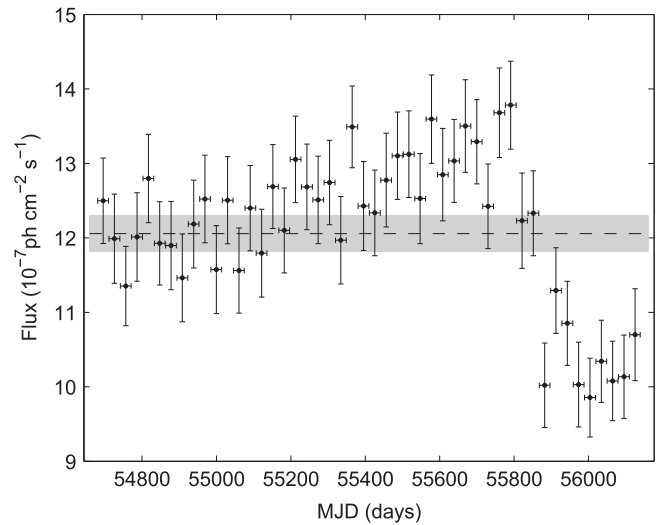

Figure 12. Light curve of 3FGL J2021.5+4026 (PSR J2021+4026 in the γ Cygni SNR). The variability of that pulsar is easily detected by the automatic procedure. The vertical scale does not start at 0.

The Crab Nebula and pulsar are a particularly difficult case. The nebula is very variable (Abdo et al. 2011c; Tavani et al. 2011), while the pulsar has no detected variability. So we would have liked the synchrotron component to absorb the full variability in 3FGL. It does not turn out this way, however, because the spectrum of the nebula becomes much harder during flares. This is not accounted for in the variability analysis (the spectral slopes are fixed to that in the full interval). As a result, the pulsar component also increases during the nebular flares and the pulsar becomes formally variable. We stress here that it is only a feature of our automatic analysis and is in no way a real detection of variability in the Crab pulsar. Besides the Crab, we detect the (real) variability of PSR J2021+4026 (Figure 12, Allafort et al. 2013). The only other formally variable pulsar is PSR J1732−3131 just above threshold. Since this is 1 in 137 pulsars, it is compatible with a chance occurrence at the 99% confidence level.

3.7. Limitations and Systematic Uncertainties

3.7.1. Source Confusion

As for the 1FGL and 2FGL catalogs, we investigated source confusion by comparing the actual distribution of angular separations between 3FGL sources with what would be expected for a population of sources that could be detected independently regardless of how small their angular separations. The formalism is defined in Abdo et al. (2010d, 1FGL). We considered the region of the sky above $|b| = 10°$, within which the average angular separation of 3FGL sources is $2°2$. The distribution of nearest neighbors distances is shown in Figure 13 along with the distribution expected if the source detection efficiency did not decrease for closely spaced sources. The observed density of nearest-neighbor starts to fall below the expected curve at about $0°8$ angular separation. The implied number of missing closely spaced sources is ∼140, or about 6% of the estimated true source count in the region. For the 2FGL catalog the fraction was only 3.3%. This indicates that even
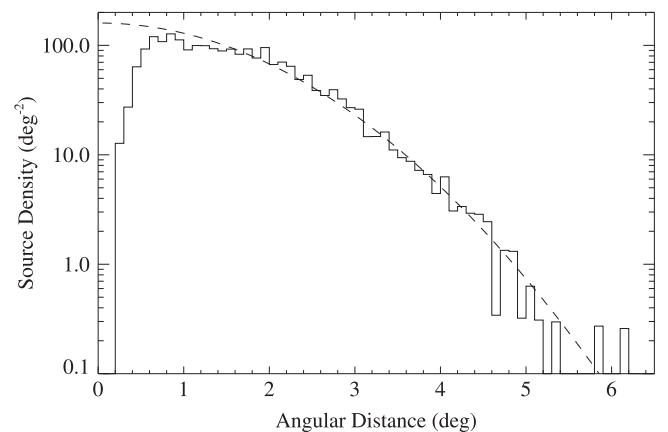
Figure 13. Distribution of nearest-neighbor distances for 3FGL sources at $|b| > 10°$. The dashed curve was derived as described in Abdo et al. (2010d, 1FGL). It is the distribution expected if sources could be detected at arbitrarily small angular separations. The dashed curve is normalized to match the total observed number of sources for separations $>0°8$ (2035). This corresponds to an expected true number of sources (extrapolated down to 0 separation) of 2336 at $|b| > 10°$.

though the PSF improved after the Pass 7 reprocessing, the larger number of detected sources (2193 versus 1319) is now pushing the LAT catalog into the confusion limit even outside the Galactic plane. Because the confusion process goes as the square of the source density, the expected number of sources above the detection threshold within $0°5$ of another one (most of which are not resolved) has increased by a factor of 3 between 2FGL and 3FGL.

The consequence of source confusion is not only losing a fraction of sources. It can also lead to "composite" γ-ray sources merging the characteristics of two very nearby astronomical objects. An example is the unassociated 3FGL J0536.4−3347, located between two bright blazars. Its spectrum is relatively soft, similar to that expected from the FSRQ BZQ J0536−3401, 14′ away. Its location, however, is closer (4′) to the BL Lac BZB J0536−3343 because that one dominates at high energy, where the *Fermi* PSF is best. That issue is discussed in more detail in the 3LAC paper.

Table 2
The Table Gives the Bias and the Scatter Induced by Changing One of two Important Elements in the Analysis Chain

Selection	Quantity	Diffuse Model (Section 3.7.3)		Analysis Method (Section 3.7.4)	
		Bias	Scatter	Bias	Scatter
Galactic ridge	Eflux (174)	$+1.88\sigma$ (+21%)	3.40σ (42%)	-0.47σ (−7%)	1.93σ (27%)
	Index (88)	$+1.44\sigma$ (+0.14)	1.81σ (0.37)	-0.08σ (−0.01)	2.40σ (0.21)
Galactic plane	Eflux (662)	$+0.51\sigma$ (+7%)	2.19σ (32%)	-0.66σ (−12%)	1.26σ (23%)
	Index (470)	$+0.34\sigma$ (+0.04)	1.54σ (0.21)	-0.44σ (−0.06)	1.15σ (0.15)
High latitude	Eflux (2193)	$+0.07\sigma$ (+1%)	0.98σ (15%)	-0.42σ (−7%)	0.74σ (13%)
	Index (1960)	$+0.23\sigma$ (+0.03)	0.73σ (0.10)	-0.34σ (−0.05)	0.73σ (0.10)

Note.

The table gives the bias and the scatter induced by changing one of two important elements in the analysis chain, first in units of the statistical error (i.e., on $(A_i^{\text{alt}} - A_i)/\sigma_i)$, then in absolute terms (i.e., on $A_i^{\text{alt}} - A_i$), where A_i is either the log of the energy flux between 100 MeV and 100 GeV or the spectral index in the standard analysis, A_i^{alt} is the same quantity in the alternative analysis, and σ_i the statistical uncertainty on A_i. The spectral index comparison is restricted to pure power-law sources. The Galactic ridge is defined as $|b| < 2°$ and $|l| < 60°$. High latitude is defined as $|b| \geqslant 10°$. The Galactic plane is everything else (i.e., it does not include the Galactic ridge). The number of sources in each selection is given in parentheses after the quantity.

3.7.2. Instrument Response Functions

The systematic uncertainties on effective area have improved since 2FGL, going from P7SOURCE_V6 to P7REP_SOURCE_V15. They are now estimated to be 5% between 316 MeV and 10 GeV, increasing to 10% at 100 MeV and 15% at 1 TeV (see the caveats page at the FSSC), following the methods described by Ackermann et al. (2012a). As in previous LAT catalogs, we have not included those uncertainties in any of the error columns, because they apply uniformly to all sources. They must be kept in mind when working with absolute numbers, but comparisons between sources can be carried out at better precision. The systematic uncertainties on effective area have been included in the curvature significance (Section 3.5), and a systematic uncertainty of 2% on the stability of monthly flux measurements (measured directly on the bright pulsars) has been included in the variability index (Section 3.6).

3.7.3. Diffuse Emission Model

The model of diffuse emission is the main source of uncertainties for faint sources. Contrary to the effective area, it does not affect all sources equally: its effects are smaller outside the Galactic plane, where the diffuse emission is fainter and varying on larger angular scales. It is also less of a concern in the high-energy bands (>3 GeV), where the core of the PSF is narrow enough that the sources dominate the background under the PSF. But it is a serious concern inside the Galactic plane in the low-energy bands (<1 GeV) and particularly inside the Galactic ridge ($|l| < 60°$), where the diffuse emission is strongest and very structured, following the molecular cloud distribution. It is not easy to assess precisely how large the uncertainties are, because they relate to uncertainties in the distributions of interstellar gas, the interstellar radiation field, and cosmic rays, which depend in detail on position on the sky.

For an assessment we have tried re-extracting the source spectra using one of the eight alternative interstellar emission models described in de Palma et al. (2013), namely, the one obtained with optically thin H I, an SNR cosmic-ray source distribution and a 4 kpc halo, adapted to the P7REP IRFs. For computational reasons we have not used all eight alternative models, but that one should be representative. In each RoI we left free the normalization of each component of the model contributing (with its normalization set to 1) more than 3% of the total counts in the RoI. The isotropic normalization was also left free, but the inverse Compton, Loop I, and *Fermi* bubble components were fixed (too large scale to be fitted inside a single RoI). That approach (independent components) differs enough from the standard diffuse model that it can provide a stronger test than comparing with the previous generation diffuse model, as we did for 2FGL. Nevertheless, both models still rely on nearly the same set of H I and CO maps of the gas in the interstellar medium, so they are not as independent as we would like.

The results show that the systematic uncertainty more or less follows the statistical one, i.e., it is larger for fainter sources in relative terms. We list the induced biases and scatters of flux and spectral index in Table 2. We have not increased the flux and index errors in the catalog itself accordingly because this alternative model does not fit the data as well as the newer one. The fit quality is nearly everywhere worse, except near the Carina region, where we know that the standard model does not fit the data very well (Appendix A). From that point of view we may expect these estimates of the systematic uncertainties to be upper limits. So we regard the values as qualitative estimates. In the Galactic plane (and even worse in the Galactic ridge) the systematic uncertainties coming from the diffuse model are larger than the statistical ones. In the Galactic ridge, even the bias is larger than the statistical uncertainty. The effect is larger than what we estimated for 2FGL (even though the diffuse model has improved), partly because the exposure is twice as deep and partly because the new alternative model is further from the standard one. Outside the Galactic plane the systematic uncertainty due to the diffuse model remains less than the statistical one, and the bias is negligible.

The same comparison also allows flagging outliers as suspect (Section 3.9). A total of 119 sources received Flag 1 (Table 3) because they ended up with TS < 25 with the alternative model, and 118 received Flag 3, indicating that their photon or energy fluxes changed by more than 3σ. That uncertainty also appears in Flag 4, whereby we flag all sources with source-to-background ratio less than 10% in all bands in which they are statistically significant.

Table 3
Definitions of the Analysis Flags

Flag[a]	Meaning
1	Source with TS > 35, which went to TS < 25 when changing the diffuse model (Section 3.7.3) or the analysis method (Section 3.7.4). Sources with TS $\leqslant$ 35 are not flagged with this bit because normal statistical fluctuations can push them to TS < 25
2	Not used
3	Flux (>1 GeV) or energy flux (>100 MeV) changed by more than 3σ when changing the diffuse model or the analysis method. Requires also that the flux change by more than 35% (to not flag strong sources)
4	Source-to-background ratio less than 10% in highest band in which TS > 25 Background is integrated over πr_{68}^2 or 1 square degree, whichever is smaller
5	Closer than $\theta_{\rm ref}$ from a brighter neighbor. $\theta_{\rm ref}$ is defined in the highest band in which source TS > 25, or the band with highest TS if all are <25. $\theta_{\rm ref}$ is set to 2°.17 (FWHM) below 300 MeV, 1°.38 between 300 MeV and 1 GeV, 0°.87 between 1 and 3 GeV, 0°.67 between 3 and 10 GeV, and 0°.45 above 10 GeV ($2\,r_{68}$)
6	On top of an interstellar gas clump or small-scale defect in the model of diffuse emission; equivalent to the c designator in the source name (Section 3.8)
7	Unstable position determination; result from *gtfindsrc* outside the 95% ellipse from *pointlike*
8	Not used
9	Localization Quality > 8 in *pointlike* (Section 3.1) or long axis of 95% ellipse >0°.25
10	Spectral Fit Quality >16.3 (Equation (3) of Nolan et al. 2012, 2FGL)
11	Possibly due to the Sun (Section 3.6)
12	Highly curved spectrum; `LogParabola` β fixed to 1 or `PLExpCutoff` `Spectral_Index` fixed to 0.5 (see Section 3.3)

[a] In the FITS version the values are encoded as individual bits in a single column, with Flag n having value $2^{(n-1)}$. For information about the FITS version of the table see Table 16 in Appendix B.

3.7.4. Analysis Method

The check presented in this section is new to 3FGL. As explained in Section 3.1, a total of the *pointlike*-based method used to detect and localize sources also provides an estimate of the source spectra and significance. Therefore, we use it to estimate systematic errors due to the analysis itself. Many aspects differ between the two methods: the code, the RoIs, the Earth limb representation. The alternative method does not remove faint sources (with TS < 25) from the model. The diffuse model is the same spatially, but it was rescaled spectrally in each energy bin. The *pointlike*-based method also rescales log $\mathcal{L}$ in order to play down the energy bins in which the source-to-background ratio is low.

The procedure to compare the results is the same as in Section 3.7.3. We list the induced biases and scatters of flux and spectral index in Table 2. In general, the effect of changing the analysis procedure is less than changing the diffuse model. Outside the Galactic ridge (and even outside the Galactic plane), we observe a negative bias on flux and index (i.e., fainter harder sources with the *pointlike* pipeline) close to half the statistical error. That effect is probably the result of removing the sources below threshold in the standard method. This favors absorbing the flux of faint neighbors at low energy (where the PSF is broad), resulting in somewhat brighter and softer sources.

A total of 118 sources received Flag 1 (TS < 25 with *pointlike*), and 101 received Flag 3 (flux changed by more than 3σ). Only 25 (Flag 1) and 19 (Flag 3) sources are flagged from both the diffuse model and the analysis method comparisons. In other words, the 3FGL catalog is more or less halfway between the result from *pointlike* and the result with the alternative diffuse model. Comparing the lists from *pointlike* and the alternative diffuse model would result in 202 sources with Flag 1 and 209 with Flag 3.

3.8. Sources toward Local Interstellar Clouds and the Galactic Ridge

As we did for the 2FGL catalog, we carefully evaluated which sources are potentially artifacts due to systematic uncertainties in modeling the Galactic diffuse emission. The procedure, described in more detail in the 2FGL paper, flags unassociated sources with moderate TS and spectral index $\Gamma > 2$, corresponding to features in individual gas components. For 3FGL we did not consider sources that have very curved spectra to be artifacts. Very soft sources with power-law spectra are instead more likely to be problematic. Sources considered to be potential artifacts are assigned an analysis flag in the catalog (Section 3.9). We also append c to the source names.

Relative to the 2FGL catalog, far fewer c sources are flagged here (78 here versus 162 for 2FGL) despite the much greater number of sources overall in the 3FGL catalog. Away from the Galactic plane, the reduction of c sources is primarily due to improvement of the representation of the dark gas component of the Galactic diffuse emission model in the vicinity of massive star-forming regions (Section 2.3). At low latitudes, the reduction primarily is due to relaxing the criterion on unassociated sources with very curved spectra.

Figure 14 shows the locations of the c sources for 3FGL. The majority are close to the Galactic plane, where the diffuse γ-ray emission is brightest and very structured. Clusters are apparent in regions where spiral arms of the Milky Way are viewed essentially tangentially, in particular the Cygnus ($l \sim 80°$) and Carina ($l \sim 285°$) regions, where
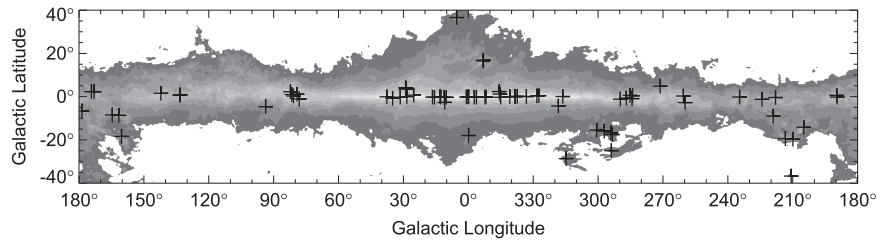
Figure 14. Locations of the c sources in the 3FGL catalog overlaid on a grayscale representation of the model for the Galactic diffuse γ-ray emission used for the 3FGL analysis (see Section 2.3). The plotted symbols are centered on the locations of the sources. The model diffuse intensity is shown for 1 GeV, and the spacing of the levels is logarithmic from 1% to 100% of the peak intensity.

the systematic uncertainties of the Galactic diffuse emission model are especially large. None of the c sources are identified (Section 5.1), and 63 (~80%) have no firm association with a counterpart at other wavelengths, a much larger fraction than the overall average (~30%) for 3FGL (Table 6).

3.9. Analysis Flags

As in 2FGL, we identified a number of conditions that should be considered cautionary regarding the reality of a source or the magnitude of the systematic uncertainties of its measured properties. They are described in Table 3.

Each flag has the same definition as for the 2FGL catalog, except for Flag 7, which was unused in that catalog.

Flags 1–12 have similar intent as in 2FGL, but differ in detail.

1. Flags 1 and 3 are now applied not only when a source is sensitive to changing the diffuse model (Section 3.7.3) but also to the analysis method (Section 3.7.4).
2. Flag 2 is not used. We did not go so far as to rerun the full detection and localization procedure (Section 3.1) with the alternative diffuse model. Assessing the changes in source characteristics is normally enough.
3. For Flag 4, we lowered the threshold for flagging the source-to-background ratio to 10%, recognizing that the uncertainties in the interstellar emission model are now reduced (Appendix A).
4. We reinstated Flag 7 (comparison between *pointlike* and *gtfindsrc* localizations), which was not used in 2FGL because of an inconsistency in the unbinned likelihood results. It indicates sources for which the source locations derived from *pointlike* (Section 3.1.3) and *gtfindsrc* are inconsistent at the 95% confidence level. *gtfindsrc* was applied only above 3 GeV due to computing time constraints. This is appropriate for most sources (because the PSF is much better at high energy) but does not allow testing the localization of soft sources.
5. Flag 8 has been merged into Flag 9. Both tested localization reliability.
6. Flag 11 is deprecated because we put in place an explicit time-dependent model for the Sun and Moon emission (Section 2.3).

4. THE 3FGL CATALOG

We present a basic description of the 3FGL catalog in Section 4.1, including a listing of the main table contents and some of the primary properties of the sources in the catalog. We present a detailed comparison of the 3FGL catalog with the 2FGL catalog in Section 4.2.

4.1. Catalog Description

Table 4 is the catalog, with information for each of the 3033 sources;[87] see Table 5 for descriptions of the columns. The source designation is 3FGL JHHMM.m+DDMM, where the 3 indicates that this is the third LAT catalog, and FGL represents *Fermi* Gamma-ray LAT. Sources close to the Galactic ridge and some nearby interstellar cloud complexes are assigned names of the form 3FGL JHHMM.m+DDMMc, where the c indicates that caution should be used in interpreting or analyzing these sources. Errors in the model of interstellar diffuse emission, or an unusually high density of sources, are likely to affect the measured properties or even existence of these 78 sources (see Section 3.8). In addition, a set of analysis flags has been defined to indicate sources with unusual or potentially problematic characteristics (see Section 3.9). The c designator is encoded as one of these flags. An additional 572 sources have one or more of the other analysis flags set. The 25 sources that were modeled as extended for 3FGL (Section 3.4) are singled out by an e appended to their names.

The designations of the classes that we use to categorize the 3FGL sources are listed in Table 6 along with the numbers of sources assigned to each class. Figure 15 illustrates where the source classes are in the sky. We distinguish between associated and identified sources, with associations depending primarily on close positional correspondence (see Section 5.2) and identifications requiring measurement of correlated variability at other wavelengths or characterization of the 3FGL source by its angular extent (see Section 5.1). In the cases of multiple associations with a 3FGL source, we adopt the single association that is statistically most likely to be true if it is above the confidence threshold (see Section 5.2). Sources associated with SNRs are often also associated with PWNe and pulsars, and the SNRs themselves are often not point-like. We do not attempt to distinguish among the possible classifications and instead list in Table 7 plausible associations of each class for unidentified 3FGL sources found to be positionally associated with SNRs.[88] The Crab pulsar and PWN are represented by a total of three entries, two of which (designated i and s) represent spectral components of the PWN (see Section 5.1). We consider these three entries to represent two sources.

[87] Table 4 has 3034 entries because the PWN component of the Crab Nebula is represented by two cospatial sources (Section 3.3).
[88] Four sources positionally associated with SNRs were also found to be associated with blazars. We cannot quantitatively compare association probabilities between the blazar and the (spatially extended) SNR classes. In the 3FGL catalog, we list only the blazar associations for them. The sources and SNR associations are 3FGL J0217.3+6209 (G137.2+01.3), 3FGL J0223.5 +6313 (G132.7+01.3), 3FGL J0526.0+4253 (G166.0+04.3), and 3FGL J0215.6+3709 (G074.9+01.2).

Table 4
LAT 4 yr Catalog

Name 3FGL	R.A.	Decl.	l	b	θ_1	θ_2	ϕ	σ	F_{35}	ΔF_{35}	S_{25}	ΔS_{25}	Γ_{25}	$\Delta\Gamma_{25}$	Mod	Var	Flags	γ-ray Assoc.	TeV	Class[a]	ID or Assoc.
J0000.1 +6545	0.038	65.752	117.694	3.403	0.102	0.078	41	6.8	1.0	0.2	13.6	2.1	2.41	0.08	PL	...	3	2FGL J2359.6+6543c	...	...	...
J0000.2 −3738	0.061	−37.648	345.411	−74.947	0.073	0.068	−89	5.1	0.2	0.1	2.4	0.7	1.87	0.18	PL	...	...	...	...	...	...
J0001.0 +6314	0.254	63.244	117.293	0.926	0.248	0.160	−65	6.2	0.6	0.1	13.0	1.9	2.73	0.11	PL	...	3,4,5	2FGL J2358.9+6325	...	spp	...
J0001.2 −0748	0.321	−7.816	89.022	−67.324	0.082	0.070	−19	11.3	0.7	0.1	7.8	0.9	2.15	0.09	PL	...	...	2FGL J0000.9−0748	...	bll	PMN J0001−0746
J0001.4 +2120	0.361	21.338	107.665	−40.047	0.211	0.188	−33	11.4	0.3	0.1	8.1	0.8	2.78	...	LP	T	...	1FGL J0000.9−0745 3EG J2359+2041	...	fsrq	TXS 2358+209
J0001.6 +3535	0.404	35.590	111.661	−26.188	0.213	0.167	8	4.2	0.3	0.1	3.4	0.8	2.35	0.19	PL	...	4	...	...	...	...
J0002.0 −6722	0.524	−67.370	310.139	−49.062	0.102	0.086	69	5.9	0.3	0.1	3.3	0.8	1.95	0.16	PL	...	...	...	...	...	...
J0002.2 −4152	0.562	−41.883	334.070	−72.143	0.217	0.140	68	5.2	0.3	0.1	3.0	0.7	2.09	0.19	PL	...	...	2FGL J0001.7−4159	...	bcu	1RXS J000135.5−415519
J0002.6 +6218	0.674	62.301	117.302	−0.037	0.061	0.054	−55	18.0	2.8	0.2	18.4	1.7	2.35	...	LP	...	...	1FGL J0001.9−4158 2FGL J0002.7+6220	...	...	...
J0003.2 −5246	0.815	−52.777	318.976	−62.825	0.070	0.061	−44	5.7	0.3	0.1	3.0	0.8	1.90	0.17	PL	...	...	...	...	bcu	RBS 0006
J0003.4 +3100	0.858	31.008	110.964	−30.745	0.181	0.163	13	6.3	0.3	0.1	4.9	0.8	2.55	0.13	PL	...	...	...	...	...	...
J0003.5 +5721	0.890	57.360	116.486	−4.912	0.089	0.072	1	5.4	0.5	0.1	5.4	1.1	2.18	0.13	PL	...	...	...	...	...	...

[a] See Table 6 for class designators.

(This table is available in its entirety in machine-readable form.)

Table 5
LAT Third Catalog Description

Column	Description
Name	3FGL JHHMM.m+DDMM[c/e/i/s] , constructed according to IAU Specifications for Nomenclature; m is decimal
	minutes of R.A.; in the name, R.A. and Decl. are truncated at 0.1 decimal minutes and 1′, respectively;
	c indicates that based on the region of the sky the source is considered to be potentially confused
	with Galactic diffuse emission; e indicates a source that was modeled as spatially extended (see Section 3.4);
	the two spectral components of the Crab PWN are designated i and s
R.A.	Right Ascension, J2000, deg, 3 decimal places
Decl.	Declination, J2000, deg, 3 decimal places
l	Galactic longitude, deg, 3 decimal places
b	Galactic latitude, deg, 3 decimal places
θ_1	Semimajor radius of 95% confidence region, deg, 3 decimal places
θ_2	Semiminor radius of 95% confidence region, deg, 3 decimal places
ϕ	Position angle of 95% confidence region, deg. east of north, 0 decimal places
σ	Significance derived from likelihood test statistic for 100 MeV–300 GeV analysis, 1 decimal place
F_{35}	Photon flux for 1–100 GeV, 10^{-9} photons cm^{-2} s^{-1}, summed over 3 bands, 1 decimal place
ΔF_{35}	1σ uncertainty on F_{35}, same units and precision
S_{25}	Energy flux for 100 MeV–100 GeV, 10^{-12} erg cm^{-2} s^{-1}, from power-law fit, 1 decimal place
ΔS_{25}	1σ uncertainty on S_{25}, same units and precision
Γ_{25}	Photon number power-law index, 100 MeV–100 GeV, 2 decimal places
$\Delta\Gamma_{25}$	1σ uncertainty of photon number power-law index, 100 MeV–100 GeV, 2 decimal places
Mod.	PL indicates power-law fit to the energy spectrum; LP indicates log-parabola fit to the energy spectrum;
	EC indicates power-law with exponential cutoff fit to the energy spectrum
Var.	T indicates <1% chance of being a steady source; see note in text
Flags	See Table 3 for definitions of the flag numbers
γ-ray Assoc.	Positional associations with 0FGL, 1FGL, 2FGL, 3EG, EGR, or 1AGL sources
TeV	Positional association with a TeVCat source, P for unresolved angular size, E for extended
Class	Like "ID" in 3EG catalog, but with more detail (see Table 6). Capital letters indicate firm identifications;
	lowercase letters indicate associations
ID or Assoc.	Designator of identified or associated source

The photon flux for 1–100 GeV (F_{35}) and the energy flux for 100 MeV–100 GeV in Table 4 are evaluated from the fit to the full band (see Section 3.5). We do not present the integrated photon flux for 100 MeV–100 GeV (see Section 3.5). Table 8 presents the fluxes in individual bands as defined in Section 3.5.

4.2. Comparison with 0FGL, 1FGL, 2FGL and 1FHL

4.2.1. General Comparison

We compare the 3FGL with previous catalogs released by the LAT collaboration. These are listed in Table 9.

Associations among 3FGL and 0FGL/1FGL/2FGL and 1FHL sources are based on the following relation:

$$\Delta \leqslant d_{x,a} = \sqrt{\theta_{x,a}^2 + \theta_{x,3FGL}^2}, \qquad (4)$$

where Δ is the angular distance between the sources, d_x is defined in terms of the semimajor axis of the $x\%$ confidence error ellipse for the position of each source, e.g., the 95% confidence error for the automatic source association procedure (Section 5.2), and "a" is alternatively 0FGL, 1FGL, 2FGL, and 1FHL. In total, 1720 3FGL sources were automatically associated with entries in either the 0FGL, 1FGL, 2FGL, or

1FHL catalogs. The statistics of the association results are reported in Table 13.

In the 3FGL analysis the spectral fits are made using power-law, power-law with an exponential cutoff, or log-parabola models (Section 3.3). For each 2FGL and 3FGL source we also evaluated the spectral index (Γ) of the best power-law fit, and this enables a comparison of the spectral characteristics of the 1FGL, 2FGL, and 3FGL sources. Figure 16 shows the distributions of the power-law indices of the sources at high Galactic latitude and only those with a power-law spectral type in the 1FGL, 2FGL and 3FGL catalogs, to avoid possible confusion from more complex features. The three distributions are very similar, with an average $\Gamma_{1FGL} = 2.23 \pm 0.01$, average $\Gamma_{2FGL} = 2.21 \pm 0.01$, and average $\Gamma_{3FGL} = 2.19 \pm 0.01$. However, the peaks of the three distributions are not exactly coincident; also, they have different skewnesses. The small differences in the power-law index distributions could be related to slightly different systematic uncertainties in the effective area between the IRFs P7REP_SOURCE_V15, P7SOURCE_V6, and P6_V3_DIFFUSE used, respectively, for 3FGL, 2FGL, and 1FGL.

We have compared the distribution of the 95% confidence error radii of the 1FGL, 2FGL, and 3FGL sources at high

Table 6
LAT 3FGL Source Classes

Description	Identified		Associated	
	Designator	Number	Designator	Number
Pulsar, identified by pulsations	PSR	143	…	…
Pulsar, no pulsations seen in LAT yet	…	…	psr	24
Pulsar wind nebula	PWN	9	pwn	2
Supernova remnant	SNR	12	snr	11
Supernova remnant/pulsar wind nebula	…	…	spp	49
Globular cluster	GLC	0	glc	15
High-mass binary	HMB	3	hmb	0
Binary	BIN	1	bin	0
Nova	NOV	1	nov	0
Star-forming region	SFR	1	sfr	0
Compact steep spectrum quasar	CSS	0	css	1
BL Lac type of blazar	BLL	18	bll	642
FSRQ type of blazar	FSRQ	38	fsrq	446
Non-blazar active galaxy	AGN	0	agn	3
Radio galaxy	RDG	3	rdg	12
Seyfert galaxy	SEY	0	sey	1
Blazar candidate of uncertain type	BCU	5	bcu	568
Normal galaxy (or part)	GAL	2	gal	1
Starburst galaxy	SBG	0	sbg	4
Narrow-line Seyfert 1	NLSY1	2	nlsy1	3
Soft-spectrum radio quasar	SSRQ	0	ssrq	3
Total	…	238	…	1785
Unassociated	…	…	…	1010

Note.
The designation "spp" indicates potential association with SNR or PWN (see Table 7). Designations shown in capital letters are firm identifications; lowercase letters indicate associations. In the case of AGNs, many of the associations have high confidence. Among the pulsars, those with names beginning with LAT were discovered with the LAT.

Galactic latitude. The distribution of 95% confidence error radius for those sources with $25 < \mathrm{TS} < 100$ in any of the 1FGL, 2FGL, and 3FGL catalogs (Figure 17) shows the localization improvement for a given range of source detection significances. We evaluated the 95% confidence error radius as the geometric mean of the semimajor and semiminor axes of the 95% confidence error ellipse.

Figure 18 shows the energy flux distribution in 1FGL, 2FGL, and 3FGL. Comparing the current flux threshold with those published in previous LAT Catalog papers, we see that in 3FGL the threshold is down to $\simeq 3 \times 10^{-12}\,\mathrm{erg\,cm^{-2}\,s^{-1}}$, from $\simeq 5 \times 10^{-12}\,\mathrm{erg\,cm^{-2}\,s^{-1}}$ in 2FGL and $\simeq 8 \times 10^{-12}\,\mathrm{erg\,cm^{-2}\,s^{-1}}$ in 1FGL. Above that flux the 2FGL and 3FGL distributions are entirely compatible.

However, the 1FGL distribution shows a distinct bump between 1 and $2 \times 10^{-11}\,\mathrm{erg\,cm^{-2}\,s^{-1}}$. That accumulation of fluxes was clearly incorrect. We attribute it primarily to overestimating significances and fluxes due to the unbinned likelihood bias in the 1FGL analysis, and also to the less accurate procedure then used to extract source flux (see discussion in the 2FGL paper).

4.2.2. Comparison of Individual Sources

Figure 19 shows the distribution of the differences $\Gamma_{\mathrm{3FGL}} - \Gamma_{\mathrm{2FGL}}$ and $\Gamma_{\mathrm{3FGL}} - \Gamma_{\mathrm{1FGL}}$ for the 621 high-latitude sources with power-law spectrum type in common among the three catalogs. The average of the 3FGL–2FGL distribution is 0.04 ± 0.01, with the 3FGL sources slightly softer than the 2FGL ones, while the average of the 3FGL–1FGL distribution is -0.04 ± 0.01, with the 3FGL sources slightly harder than the 1FGL ones.

When comparing the distribution of 95% confidence error radius for the sources in common among all the LAT catalogs, we see that for 3FGL this parameter extends to lower values than for the earlier catalogs, showing that the localization has improved, thanks to improvements in the 3FGL analysis and increased statistics over the longer integration period for 3FGL (Figure 20).

4.2.3. Possible Causes for Losing Sources

In the remainder of this section we describe a variety of reasons why the "lost" 0FGL, 1FGL, 2FGL, and 1FHL sources might not appear in the 3FGL catalog. Table 10 shows the statistics of the "lost" sources.

We have also produced tables with all the "lost" sources for each previous LAT catalog. The first rows of the "lost" γ-ray source table for the 2FGL catalog are listed in Table 11, only reported for guidance.[89] In the last columns of Table 11 we assigned to each source one or more flags corresponding to possible causes for it to be lost and which we will discuss in the following paragraphs. In many cases, no one reason can be singled out.

Lost sources from previous LAT catalogs are in general equally distributed over all latitudes, with a slight excess at low latitudes for 2FGL "lost" sources. In fact, about 10% of the 2FGL "lost" sources are at low Galactic latitude, compared to 6% of high-latitude "lost" 2FGL sources. We remind the reader that at low latitudes the Galactic diffuse emission is most intense and improvements in the model for the diffuse emission would be expected to have the most influence (Section 2.3). The sources in common among 3FGL and the previous LAT catalogs are primarily outside the Galactic plane, as are the sources newly detected in 3FGL. Most of the "lost" sources were also listed as unassociated in the previous FGL catalogs. Among the former associated "lost" sources, most of them were associated with AGNs and a few with pulsars. For sources of the AGN type their absence from the 3FGL catalog can be due to their intrinsic variability. A faint source that flared during the first year, allowing it to be detected in 0FGL, can be diluted and become undetectable in a longer time interval.

Most of the "lost" sources have analysis flags or the c designator in 1FGL and 2FGL names, indicating that these sources were already flagged as influenced by the diffuse emission and recognized as potentially problematic or possibly spurious.

Some other 1FGL, 2FGL, and 1FHL sources do not have counterparts in the 3FGL catalog because they have been resolved into two or more 3FGL sources or candidate source seeds. We flag them with "S" (split) in the "Flag" column of Table 11. In some cases only one of the seeds reached TS > 25 and so was included in the 3FGL list.

---

[89] The full table of lost 2FGL sources and similar tables for lost 0FGL, lost 1FGL, and lost 1FHL sources are available only in the electronic version.
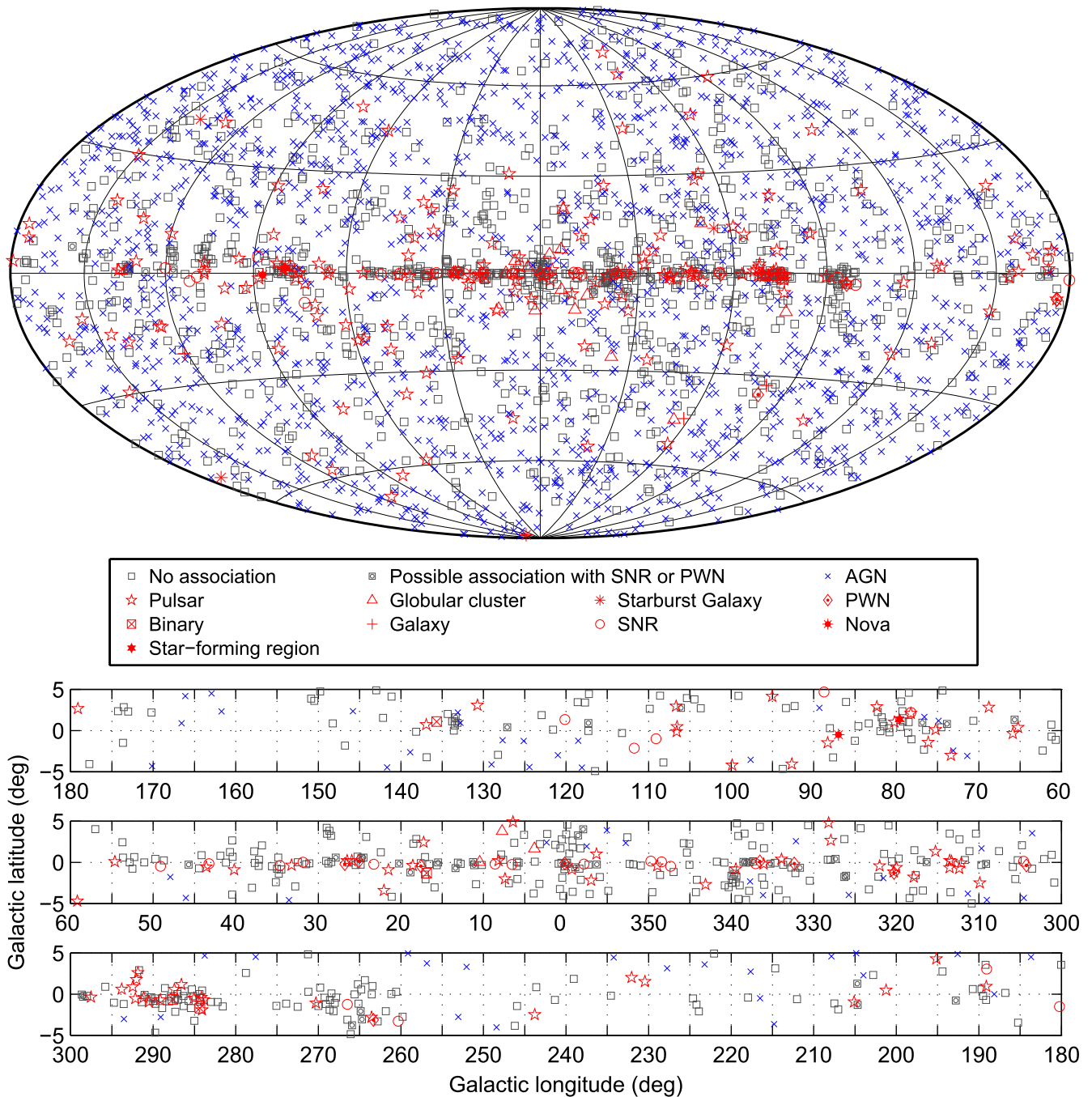
Figure 15. Full sky map (top) and blow-up of the inner Galactic region (bottom) showing sources by source class (see Table 6). All AGN classes are plotted with the same symbol for simplicity.

Several other possible causes of "lost" sources are evident: (1) the 3FGL γ-ray centroid has shifted with respect to the previous FGL catalogs, preventing the matching; (2) statistical threshold effects, i.e., their TS has dropped below 25. Additional considerations include variability and (generally small) effects from the different event selections used for the analyses (P7REP_SOURCE_V15 for 3FGL, P7CLEAN_V6 for 1FHL, P7SOURCE_V6 for 2FGL, and P6_V3_DIFFUSE for 0FGL); different Galactic diffuse emission models; different analysis procedures (unbinned likelihood analysis for 0FGL and 1FGL, binned likelihood analysis for 2FGL and 1FHL, and a combination of binned and unbinned for 3FGL). We analyze

those causes in more detail for 2FGL in Section 4.2.4. We stress that these differences are often not negligible.

A comparison of the source significances of the "lost" sources with those in the 3FGL catalog shows that (Figure 21) in the latter we have not lost highly significant sources. The peaks of the source significance distributions for all the sources of the FGL catalogs (not shown in the Figure 21) have shifted from 4–6σ for 1FGL to 4–5σ for 2FGL and 3FGL.

The power-law indices of high Galactic latitude ($|b| > 10°$) "lost" sources with power-law spectral type tend to be softer than average for their catalogs (Figure 22).

The numbers of associated sources among the 0FGL, 1FGL, and 2FGL catalogs and the 3FGL catalog do depend on the

Table 7
Potential Associations for Sources near SNRs

Name 3FGL	SNR Name	PWN Name	TeV Name	Common Name
J0001.0+6314	G116.5+01.1	…	…	…
J0128.4+6257	G127.1+00.5	…	…	R5
J0220.1+6202c	G132.7+01.3	…	…	HB3
J0224.0+6235	G132.7+01.3	…	…	HB3
J0500.3+5237	G156.2+05.7	…	…	…
J0610.6+1728	G192.8−01.1	…	…	PKS 0607+17
J0631.6+0644	G205.5+00.5	…	…	Monoceros Loop
J0640.9+0752	G205.5+00.5	…	…	Monoceros Loop
J0838.1−4615[a]	G263.9−03.3	…	…	Vela
J0839.1−4739	G263.9−03.3	…	…	Vela
J0843.1−4546	G263.9−03.3	…	…	Vela
J1101.9−6053	G290.1−00.8	…	…	MSH 11−61A
J1111.9−6038	G291.0−00.1	G291.0−0.1	…	MSH 11−62
J1209.1−5224	G296.5+10.0	…	…	PKS 1209−51
J1212.2−6251	G298.5−00.3	…	…	…
J1214.0−6236	G298.6−00.0	…	…	…
J1345.1−6224	G308.8−00.1	…	…	…
J1441.5−5955c	G316.3−00.0	…	…	MSH 14−57
J1549.1−5347c	G327.4+00.4	…	…	…
J1551.1−5610	G326.3−01.8	…	…	Kes 25
J1552.9−5610	G326.3−01.8	…	…	Kes 25
J1615.3−5146e	…	HESS J1614−518	…	…
J1628.9−4852	G335.2+00.1	…	…	…
J1636.2−4709c	G337.2+00.1	…	HESS J1634−472	…
J1638.6−4654[a]	G337.8−00.1	…	…	Kes 41
J1640.4−4634c	G338.3−00.0	…	HESS J1640−465	…
J1641.1−4619c	G338.5+00.1	…	HESS J1641−463	…
J1645.9−5420	G332.5−05.6	…	…	…
J1722.9−4529	G343.0−06.0	…	…	RCW 114
J1725.1−2832	G358.0+03.8	…	…	…
J1728.0−4606	G343.0−06.0	…	…	RCW 114
J1729.5−2824	G358.0+03.8	…	…	…
J1737.3−3214c	G356.3−00.3	…	…	…
J1745.1−3011	G359.1−00.5	…	HESS J1745−303	…
J1745.6−2859c	G000.0+00.0	G359.95−0.04	Galactic center	Sgr A East
J1810.1−1910	G011.1+00.1	…	HESS J1809−193	…
J1811.3−1927c	G011.2−00.3	…	HESS J1809−193	…
J1817.2−1739	G013.3−01.3	…	…	…
J1818.7−1528[a]	G015.4+00.1	…	…	…
J1828.4−1121[a]	G020.0−00.2	…	…	…
J1829.7−1304	G018.9−01.1	…	…	…
J1833.9−0711[a]	G024.7+00.6	…	…	…
J1834.6−0659	G024.7+00.6	…	…	…
J1840.1−0412	G027.8+00.6	…	…	…
J1915.9+1112	G045.7−00.4	…	…	…
J1951.6+2926	G065.7+01.2	…	…	…
J2014.4+3606	G073.9+00.9	…	…	…
J2022.2+3840	G076.9+01.0	…	…	…
J2225.8+6045	G106.3+02.7	…	G106.3+2.7	…

Note.

These sources are classified as spp in Table 4. They may be pulsars rather than the SNR or PWN named. Four additional 3FGL sources are associated with both an SNR and a blazar. For these the catalog lists the blazar associations; see text.

[a] These sources have been found to be significantly variable, i.e., `Variability_Index` > 72.44 (Section 3.6), which would be unexpected for physical associations with SNRs or PWNe.

criteria used to define spatial coincidence (Equation (4)). The numbers of 1FGL–3FGL, 2FGL–3FGL, and 1FHL–3FGL associated sources increase if we use $\Delta < d_{99.9}$ as an association criterion.[90] The 193 additional associations (listed

in Table 11 and corresponding 0FGL, 1FGL, 1FHL tables in the column "3FGL $(\Delta < d_{99.9})$") represent about 5% of the 0FGL, 1FGL, 2FGL, and 1FHL sources, as expected when passing from d_{95} to $d_{99.9}$. Furthermore, the improved model of the Galactic diffuse emission (Section 2.3) used to build the 3FGL catalog, together with the expected increase of the signal-to-noise ratio due to the use of 48 months of data,

[90] Assuming a Rayleigh distribution for the source angular separations, $d_{99.9}$ is evaluated using $\theta_{99.9} = 1.52\,\theta_{95}$.

Table 8
LAT 4 yr Catalog: Spectral Information

	0.1–0.3 GeV		0.3–1 GeV		1–3 GeV		3–10 GeV		10–100 GeV	
Name 3FGL	F_1[a]	$\sqrt{TS_1}$	F_2[a]	$\sqrt{TS_2}$	F_3[b]	$\sqrt{TS_3}$	F_4[c]	$\sqrt{TS_4}$	F_5[c]	$\sqrt{TS_5}$
J0000.1+6545	$1.81^{+0.82}_{-0.84}$	2.2	$0.69^{+0.14}_{-0.14}$	5.3	$1.24^{+0.23}_{-0.23}$	6.0	$0.58^{+0.49}_{-0.40}$	1.5	$0.28^{+0.19}_{-0.15}$	2.4
J0000.2−3738	$0.01^{+0.20}_{-0.01}$	0.0	$0.01^{+0.03}_{-0.01}$	0.6	$0.15^{+0.07}_{-0.06}$	2.9	$0.75^{+0.32}_{-0.26}$	4.2	$0.16^{+0.15}_{-0.09}$	3.5
J0001.0+6314	$2.91^{+0.74}_{-0.71}$	4.0	$0.47^{+0.11}_{-0.11}$	4.3	$0.30^{+0.18}_{-0.18}$	1.7	$1.16^{+0.48}_{-0.42}$	3.3	$0.02^{+0.13}_{-0.02}$	0.4
J0001.2−0748	$0.41^{+0.26}_{-0.26}$	1.6	$0.21^{+0.05}_{-0.04}$	5.3	$0.52^{+0.11}_{-0.10}$	7.0	$2.11^{+0.51}_{-0.45}$	8.0	$0.10^{+0.15}_{-0.08}$	1.6
J0001.4+2120	$1.52^{+0.24}_{-0.24}$	6.8	$0.36^{+0.05}_{-0.05}$	7.6	$0.36^{+0.10}_{-0.09}$	4.5	$0.00^{+0.19}_{-0.00}$	0.0	$0.00^{+0.11}_{-0.00}$	0.0
J0001.6+3535	$0.95^{+0.27}_{-0.27}$	3.6	$0.04^{+0.04}_{-0.04}$	0.9	$0.17^{+0.09}_{-0.08}$	2.5	$0.40^{+0.31}_{-0.23}$	2.0	$0.23^{+0.19}_{-0.13}$	2.3
J0002.0−6722	$0.05^{+0.28}_{-0.05}$	0.2	$0.06^{+0.03}_{-0.03}$	2.0	$0.20^{+0.08}_{-0.07}$	3.4	$0.83^{+0.32}_{-0.27}$	4.8	$0.28^{+0.19}_{-0.14}$	3.1
J0002.2−4152	$0.53^{+0.22}_{-0.22}$	2.5	$0.06^{+0.03}_{-0.03}$	2.1	$0.09^{+0.07}_{-0.06}$	1.5	$0.98^{+0.36}_{-0.31}$	4.7	$0.26^{+0.19}_{-0.14}$	2.6
J0002.6+6218	$1.05^{+0.40}_{-0.40}$	2.6	$0.80^{+0.09}_{-0.09}$	9.4	$2.44^{+0.23}_{-0.23}$	13.3	$3.58^{+0.69}_{-0.64}$	7.4	$0.00^{+0.15}_{-0.00}$	0.0
J0003.2−5246	$0.66^{+0.38}_{-0.38}$	1.8	$0.00^{+0.03}_{-0.00}$	0.0	$0.18^{+0.08}_{-0.07}$	3.1	$0.79^{+0.36}_{-0.28}$	3.7	$0.30^{+0.19}_{-0.14}$	4.5
J0003.4+3100	$0.86^{+0.27}_{-0.25}$	3.4	$0.15^{+0.04}_{-0.04}$	3.6	$0.36^{+0.10}_{-0.09}$	4.9	$0.20^{+0.26}_{-0.19}$	1.1	$0.01^{+0.14}_{-0.01}$	0.1
J0003.5+5721	$0.00^{+0.31}_{-0.00}$	0.0	$0.23^{+0.07}_{-0.07}$	3.5	$0.49^{+0.14}_{-0.14}$	4.0	$0.92^{+0.41}_{-0.35}$	3.3	$0.24^{+0.16}_{-0.12}$	3.0
J0003.8−1151	$0.01^{+0.21}_{-0.01}$	0.0	$0.05^{+0.04}_{-0.03}$	1.5	$0.23^{+0.08}_{-0.07}$	3.8	$0.47^{+0.30}_{-0.24}$	2.5	$0.18^{+0.16}_{-0.11}$	2.5
J0004.2+6757	$0.59^{+1.16}_{-0.59}$	0.5	$0.56^{+0.13}_{-0.13}$	4.4	$0.59^{+0.19}_{-0.18}$	3.4	$1.15^{+0.47}_{-0.42}$	3.2	$0.09^{+0.11}_{-0.07}$	1.4
J0004.2+0843	$0.23^{+0.25}_{-0.23}$	0.8	$0.03^{+0.04}_{-0.03}$	0.7	$0.12^{+0.09}_{-0.08}$	1.5	$1.16^{+0.41}_{-0.35}$	5.3	$0.08^{+0.12}_{-0.06}$	2.0

Notes.
[a] In units of 10^{-8} photons cm^{-2} s^{-1}.
[b] In units of 10^{-9} photons cm^{-2} s^{-1}.
[c] In units of 10^{-10} photons cm^{-2} s^{-1}.

(This table is available in its entirety in machine-readable form.)

Table 9
Statistics of Sources in LAT Catalogs

	0FGL[a]	1FGL	2FGL	1FHL[b]	3FGL
Total	205	1451	1873	514	3033
High-latitude sources	132	1043	1319	399	2193
Low-latitude sources	73	408	554	115	841
"Lost" sources[c] in 3FGL	12	310	300	17	...

Notes.
[a] 0FGL, the LAT Bright Source List, has a lower energy limit of 200 MeV and a significance threshold TS > 100.
[b] 1FHL is a catalog for the energy range >10 GeV.
[c] Sources without a counterpart in the 3FGL catalog, at the level of overlapping 95% source location confidence contours. These sources are discussed in Table 10.

allowed us to obtain better localizations of the sources at positions that might be outside the 95% confidence error regions reported in the 0FGL, 1FGL, or 2FGL catalogs. Indeed, about half of the 193 additional associations concern sources located along the Galactic plane. Also, in the 1FGL catalog the positions of sources associated with the LAT-detected pulsars and X-ray binaries are the high-precision positions of the identified counterparts. (These sources can be easily recognized because they have null values in the localization parameters reported in the 1FGL catalog.) Not all of these associations appear in the 3FGL catalog because they cannot be associated using d_{95}, but those that can be associated using $d_{99.9}$ are listed in Table 11 (and corresponding 0FGL, 1FGL, and 1FHL tables).
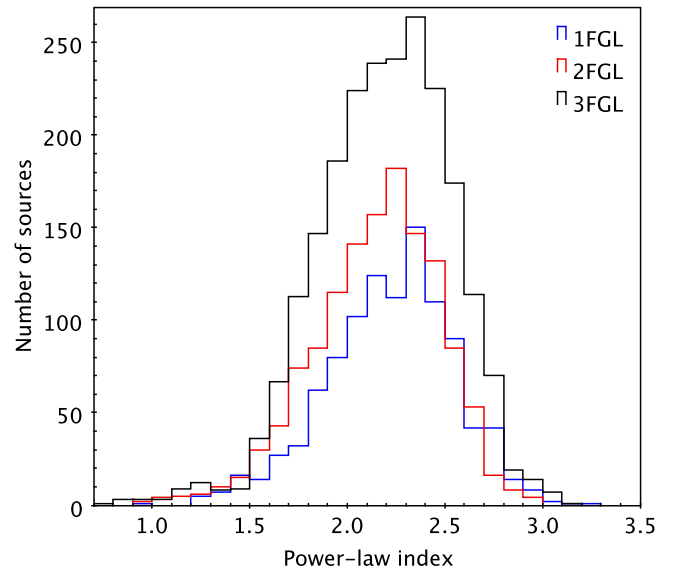

Figure 16. Distributions of the spectral index for the high-latitude sources ($|b| > 10°$) in 1FGL (1043 sources, blue line), 2FGL (1173 sources, red line), and 3FGL (1960 sources, black line) catalogs. 2FGL and 3FGL samples include only power-law spectrum type.

To study a possible reason for 0FGL, 1FGL, 2FGL, and 1FHL sources to disappear in the 3FGL catalog, we have compared the TS they had when published in their respective catalogs with their values in the 3FGL *pointlike* analysis. The 3FGL catalog was built, in fact, starting from 4003 seeds with TS > 10 in the *pointlike* analysis (Section 3.1). The final *gtlike* analysis, which did not change the positions of the seeds,
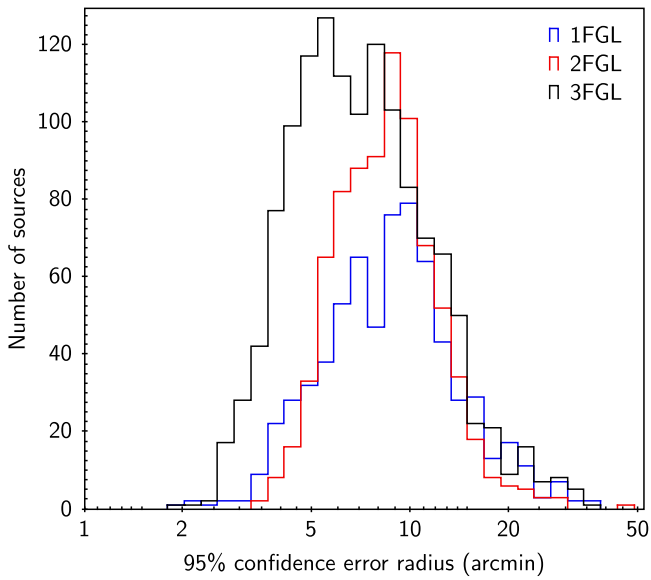
Figure 17. Distributions of the 95% confidence error radii for high-latitude sources ($|b| > 10°$) with $25 < TS < 100$ in 1FGL (blue line), 2FGL (red line), and 3FGL (black line), illustrating the improvement of localizations for sources of equivalent detection significances.
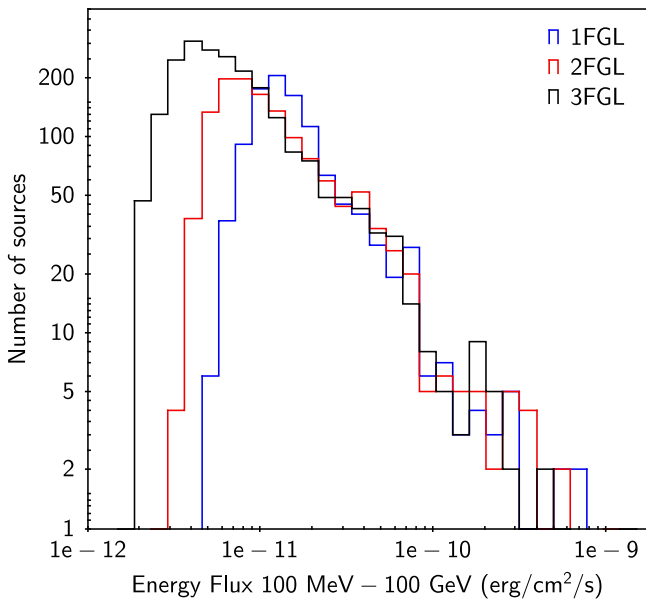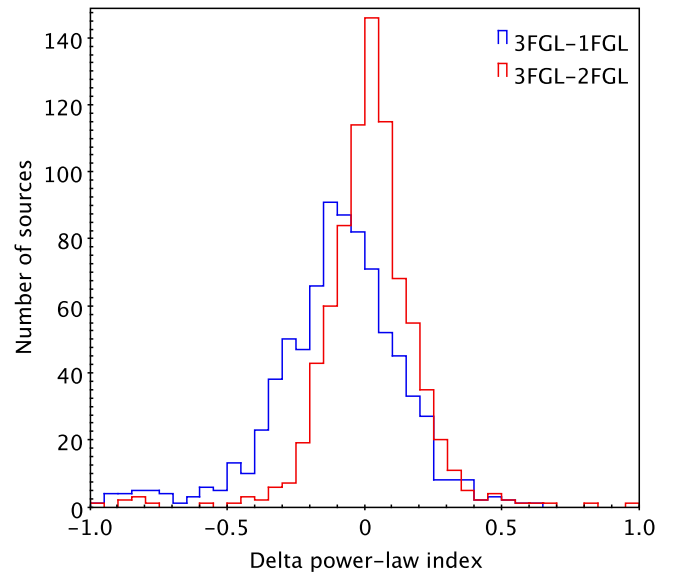

Figure 19. Distribution of the differences $\Gamma_{3FGL} - \Gamma_{1FGL}$ (blue line) and $\Gamma_{3FGL} - \Gamma_{2FGL}$ (red line) for the 621 sources at high latitude ($|b| > 10°$) in common among the 1FGL, 2FGL, and 3FGL catalogs. For the 2FGL and 3FGL samples only power-law spectrum type sources have been considered.

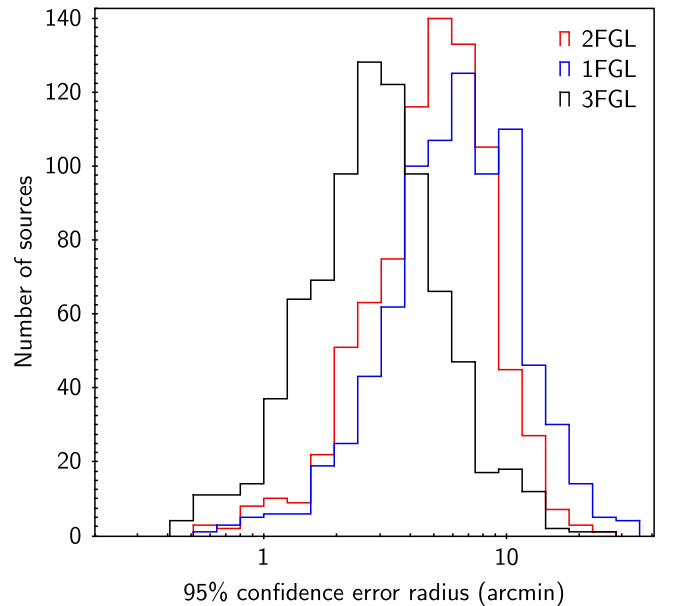**Figure 18.** Distributions of the energy flux for 1FGL (blue line), 2FGL (red line), and 3FGL (black line) sources at high Galactic latitude ($|b| > 10°$).

Figure 20. Distributions of the 95% confidence error radius for high-latitude sources ($|b| > 10°$) in common among 1FGL (blue line), 2FGL (red line), and 3FGL (black line), illustrating the improvement of localizations for sources of equivalent detection significances.

resulted in the 3033 sources with TS > 25 that make up the 3FGL catalog. Therefore, possibly many seeds did not reach the threshold but can be associated with 0FGL, 1FGL, 2FGL, and 1FHL sources (using $\Delta < d_{99.9}$). These sources, marked with "T" (for "*true*") in the "3FGL Seed" column of the Table 11, can be considered to be previously confirmed sources whose significance dropped below the threshold, as a result of time variability, changes in the model, or changes in the catalog analysis procedure for Galactic diffuse emission. Finally, we looked for those "lost" sources whose distances from an extended 3FGL source are less than 1°, and these are flagged with "E" in the column "Flag" of Table 11.

4.2.4. Step-by-step from 2FGL to 3FGL

In order to understand the improvements of the 3FGL analysis with respect to 2FGL, we have considered the effects of changing the analysis, the data set, and the diffuse emission model without changing the time range (i.e., leaving it as 2 yr years). To that end, we started with the 2FGL catalog and changed each of those three elements in sequence and compared each intermediate result with the previous one.

1. The main difference between the analyses is the *Front/Back* handling (Section 3.2). The comparison showed

Table 10
Statistics of "Lost" 0FGL, 1FGL, 2FGL, and 1FHL Sources

Category	0FGL not in 3FGL	1FGL not in 3FGL	2FGL not in 3FGL	1FHL not in 3FGL
All	12	310	300	17
With flags	...	131	211	...
Name-FGL c[a]	...	104	87	...
AGNs	1	22	27	1
PSR	0	1	3	0
Unassociated	11	264	234	16
Within 1° of a 3FGL e[b]	3	27	33	4
Sources in Other FGL Catalogs				
0FGL	...	5	5	0
1FGL	4	...	56	1
2FGL	3	67	...	1
1FHL	0	2	8	...
Not in any other *Fermi* catalog	7	237	237	15

Notes.
[a] c indicates that based on the region of the sky the source is considered to be potentially confused with Galactic diffuse emission.
[b] e indicates a source that was modeled as spatially extended.

that using identical isotropic diffuse spectra for *Front* and *Back* events in 2FGL resulted in underestimating the low-energy fluxes of high-latitude sources. As a consequence, the corrected analysis leads to larger TS values, higher photon fluxes, softer spectra, and smaller curvatures than in 2FGL. The effects are small on the scale of individual sources but collectively obvious. Quantitatively, the average difference in spectral index induced by this change was measured to be +0.05. Because that effect is due to the background, it is at the same level in σ units ($\simeq 0.4\sigma$) for faint and bright sources.

2. Changing data from Pass 7 (2FGL) to Pass 7 reprocessed (3FGL) results in somewhat larger TS, harder sources, and more curved spectra (but no change of integral flux on average). The average difference in spectral index is −0.03. This goes in the opposite direction to (and therefore partly offsets) the difference due to the separate *Front/Back* handling. However, the dependence on flux is not the same. The reprocessing affects essentially all spectral indices and curvatures equally in absolute terms.

3. Finally, changing the model for Galactic diffuse emission from `gal_2yearp7v6_v0` used in 2FGL to `gll_iem_v05_rev1` results in smaller TS, lower fluxes, and less curved spectra (but no change of spectral index on average). Like the first point above, this background-related effect is smaller in absolute (curvature) or relative (flux) terms for brighter sources.

In conclusion, to first order the resulting net changes are not very large, consistent with the general comparison between 3FGL and 2FGL at the beginning of this section. The 3FGL sources tend to be less curved than 2FGL ones. In particular, there are fewer pathological very strongly curved sources (with $\beta = 1$ and Flag 12 set) in 3FGL (41) than in 2FGL (64) even though there are more `LogParabola` spectra in 3FGL (395) than in 2FGL (336) because of the better statistics.

5. SOURCE ASSOCIATION AND IDENTIFICATION

5.1. Firm Identifications

As with the 2FGL and earlier LAT catalogs, we retain the distinction between associations and firm identifications. Although many associations that we list between LAT sources and potential counterparts at other wavelengths, particularly those for AGNs, have very high probability of being true, a firm identification, shown in the catalog by capitals in the Class column in Table 6, is based on one of three criteria.

1. Periodic Variability. Pulsars are the largest class in this category. All PSR labels indicate that pulsed γ-rays have been seen from the source with a probability of the periodicity occurring by chance of less than 10^{-6}. Pulsars detected in blind searches of LAT data are indicated as "LAT PSR" in the "ID or Assoc." column of Table 4; the other PSR detections are based on folding with radio or X-ray ephemerides (see Abdo et al. 2013). A similar chance probability requirement applies to the other set of periodic sources, the high-mass binaries (HMB). Three of these are included in the catalog: LS I+61 303 (Abdo et al. 2009c), LS 5039 (Abdo et al. 2009e), and 1FGL J1018.6−5856 (Corbet et al. 2011). Although not quite meeting the same chance probability, another binary (BIN) is included as an identification: Eta Carinae (Reitberger et al. 2012, 2015).

2. Spatial Morphology. Spatially extended sources whose morphology can be related to extent seen at other wavelengths include SNRs, PWNe, and galaxies, as described in Section 3.4. The Centaurus A lobes and core are both marked as identified, because they are part of the same extended source, although the core itself does not show spatial extent. Although individual molecular clouds could in principle be included in this list, the catalog construction incorporates most known clouds into the diffuse model, and so no sources of this type are identified in the catalog.

3. Correlated Variability. Variable sources, primarily AGNs, whose γ-ray variations can be matched to variability seen at one or more other wavelengths, are considered to be firm identifications. Although some cases are well documented, such correlated variability is not always easily defined. We conservatively require data in more than two energy bands for comparison. Finding a blazar to have a high X-ray flux at the same time as a γ-ray flare, for example, does not qualify if there is no long-term history for the X-ray emission. We include those sources whose variability properties are documented either in papers or with Astronomer's Telegrams.[91] This list does not represent the result of a systematic study. Ongoing work will undoubtedly enlarge this list. The one Galactic source identified in this way is nova V407 Cygni (Abdo et al. 2010h). Similarly short duration tangent gamma-ray emission observed from the classical novae, V959 Mon 2012 and V1234 Sco 2012, were not detected in the 4 yr integrated analysis in the 3FGL (Ackermann et al. 2014).

We include one exception to these rules. The Crab PWN is listed as a firm identification even though it does not meet any

---

[91] See http://www.astronomerstelegram.org.

Table 11
2FGL Sources Not in the 3FGL Catalog

2FGL	2FGL Assoc.[a]	l[a] (deg)	b[a] (deg)	θ_{95}[a] (deg)	σ[a]	Γ_{25}[a]	Var[a] $p>90\%$	3FGL[b] ($\Delta < d_{99.9}$)	3FGL[c] ($d_{99.9} < \Delta < 1°$)	Δ[d] (deg)	$\Delta/d_{99.9}$	3FGL[e] Seed	Flags[f]
J0004.2+2208	⋯	108.732	−39.43	0.194	5.401	2.494	F	⋯	⋯	⋯	⋯	T	⋯
J0011.3+0054	PMN J0011+0058	102.317	−60.352	0.223	6.172	2.435	T	⋯	⋯	⋯	⋯	⋯	F
J0013.8+1907	GB6 J0013+1910	110.786	−42.858	0.16	4.077	2.056	T	⋯	⋯	⋯	⋯	⋯	⋯
J0014.3−0509	⋯	99.374	−66.312	0.169	4.218	2.445	F	J0014.3−0455	⋯	0.322	0.725	T	F
J0118.6−4631	⋯	289.226	−69.872	0.134	4.483	1.782	F	⋯	⋯	⋯	⋯	⋯	⋯
J0124.6−2322	⋯	188.135	−81.611	0.113	7.473	2.31	F	⋯	J0123.7−2312	0.217	1.225	⋯	S,F
J0128.0+6330	⋯	126.998	0.922	0.255	4.965	2.57	F	⋯	J0128.4+6257	0.432	1.262	⋯	F
J0129.4+2618	⋯	133.451	−35.784	0.333	4.863	2.561	F	J0127.9+2551	⋯	0.813	0.707	T	⋯
J0158.6+8558	⋯	124.201	23.262	0.18	4.24	2.521	F	J0145.6+8600	⋯	0.334	0.691	T	⋯
J0214.5+6251c	⋯	132.251	1.495	0.134	4.112	2.257	F	⋯	⋯	⋯	⋯	⋯	c, F
J0218.7+6208c	⋯	132.937	0.975	0.078	10.52	2.767	F	J0217.3+6209	⋯	0.208	0.753	T	S, c, F
J0219.1−1725	1RXS J021905.8−172503	191.883	−67.564	0.148	4.315	1.92	F	⋯	⋯	⋯	⋯	T	⋯
J0221.3+6025c	⋯	133.81	−0.528	0.11	4.579	2.452	F	⋯	J0221.1+6059	0.391	1.451	⋯	c, F
J0221.4+6257c	⋯	132.962	1.856	0.118	9.547	2.635	F	⋯	J0223.5+6313	0.316	1.11	T	S, c, F
J0227.2+6029c	⋯	134.471	−0.22	0.097	6.069	2.383	F	⋯	⋯	⋯	⋯	⋯	c, F

Notes.

[a] All the values reported in these columns are from the 2FGL catalog.

[b] Name of the 3FGL source associated with the 2FGL source with positional coincidence evaluated using $d_{99.9}$.

[c] Closest 3FGL source having a distance $d_{99.9} < \Delta < 1°$ from the position of the 2FGL source.

[d] In this column is reported the angular separation (Δ) between the 2FGL source and the 3FGL sources associated using $d_{99.9}$ or the closest 3FGL source.

[e] T: The 2FGL source and one of the initial seeds for the 3FGL analysis have angular separation $<d_{99.9}$.

[f] S: The 2FGL source was split/resolved into one or more seeds; c: The 2FGL source was flagged with c, i.e., possibly contaminated by the diffuse emission; F: the 2FGL source had analysis flags; E: The 2FGL source has a distance $<1°$ from an extended 3FGL source. (This table is available in its entirety in FITS format.)
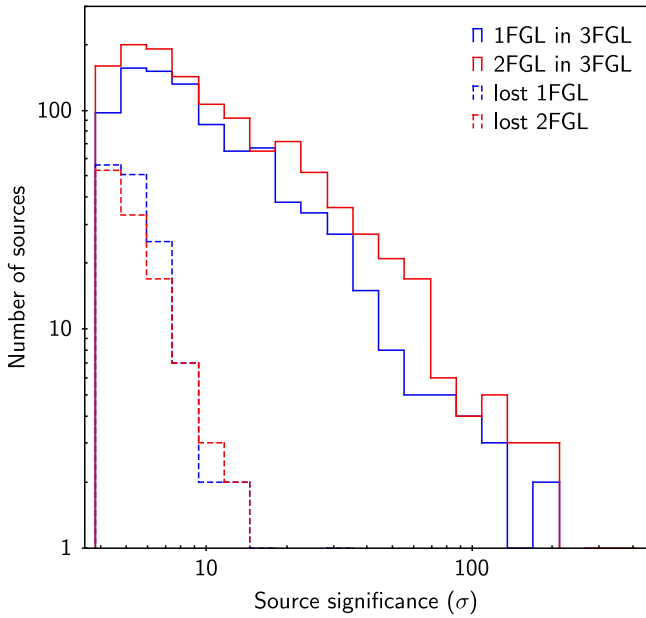
Figure 21. Distributions of the significances of "lost" 1FGL and "lost" 2FGL sources compared to the 1FGL and 2FGL sources that are associated with 3FGL sources. All sources at high Galactic latitudes ($|b| > 10°$) are included. (2FGL sources associated to 3FGL sources: solid red line, "lost" 2FGL sources: dashed red line, 1FGL sources associated to 3FGL sources: solid blue line, "lost" 1FGL sources: dashed blue line).
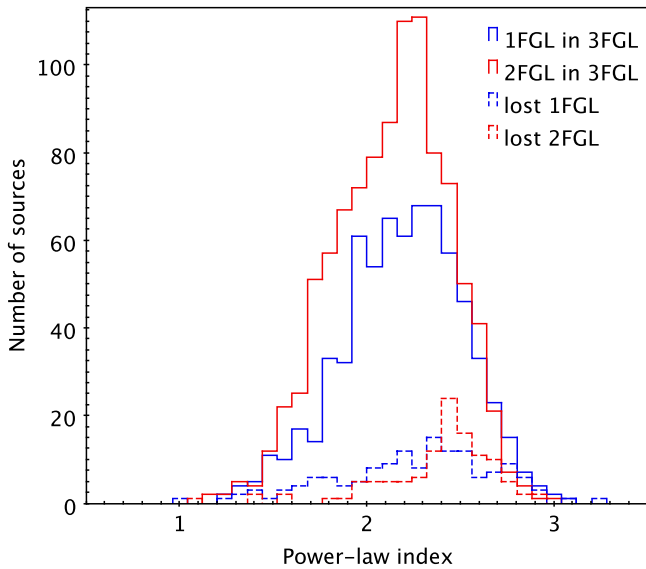

Figure 22. Distributions of the power-law index of the 1FGL sources (blue solid line) and 2FGL sources (red solid line) in the 3FGL catalog and of the "lost" 1FGL sources (blue dashed line) and 2FGL sources (red dashed line). All samples include only high-latitude sources ($|b| > 10°$).

of these criteria. The well-defined energy spectrum, distinct from the Crab pulsar spectrum and matching spectra seen at both lower and higher energies, provides a unique form of identification (Abdo et al. 2010e).

In total, we firmly identify 238 out of the 3033 3FGL sources. Among those, 143 are pulsars, 66 are AGNs (BCU, BLL, FSRQ, NLSY1, or RDG) 12 are SNRs, 4 are binaries (BIN or HMB), 9 are PWNe, 2 are normal galaxies, 1 is a massive star-forming region, and 1 is a nova (Table 6).

Table 12
Catalogs Used for the Automatic Source Association Methods

Name	Objects[a]	Reference
High $\dot{E}/d^2$ pulsars	213	Manchester et al. (2005) [b]
Other normal pulsars	1657	Manchester et al. (2005) [b]
Millisecond pulsars	137	Manchester et al. (2005) [b]
Pulsar wind nebulae	69	Collaboration internal
High-mass X-ray binaries	114	Liu et al. (2006)
Low-mass X-ray binaries	187	Liu et al. (2007)
Point-like SNRs	157	Green (2009)
Extended SNRs[†]	274	Green (2009)
O stars	378	Maíz-Apellániz et al. (2004)
WR stars	226	van der Hucht (2001)
LBV stars	35	Clark et al. (2005)
Open clusters	2140	Dias et al. (2002)
Globular clusters	160	Harris (1996)
Dwarf galaxies[†]	100	McConnachie (2012)
Nearby galaxies	276	Schmidt et al. (1993)
IRAS bright galaxies	82	Sanders et al. (2003)
BZCAT (Blazars)	3060	Massaro et al. (2009)
BL Lac	1371	Véron-Cetty and Véron (2010)
AGNs	10,066	Véron-Cetty and Véron (2010)
QSO	129,853	Véron-Cetty and Véron (2010)
Seyfert galaxies	27,651	Véron-Cetty and Véron (2010)
Radio-loud Seyfert galaxies	29	Collaboration internal
1WHSP	1000	Arsioli et al. (2015)
WISE blazar catalog	7855	D'Abrusco et al. (2014)
NRAO VLA Sky Survey (NVSS)[c]	1,773,484	Condon et al. (1998)
Sydney University Molonglo Sky Survey (SUMSS)[c]	211,050	Mauch et al. (2003)
Parkes-MIT-NRAO survey[c]	23,277	Griffith & Wright (1993)
CGRaBS	1625	Healey et al. (2008)
CRATES	11,499	Healey et al. (2007)
VLBA Calibrator Source List	5776	http://www.vlba.nrao.edu/astro/calib/vlbaCalib.txt
ATCA 20 GHz southern sky survey	5890	Murphy et al. (2010)
ATCA follow-up of 2FGL unassociated sources	424	Petrov et al. (2013)
ROSAT All Sky Survey (RASS) Bright and Faint Source Catalogs[c]	124,735	Voges et al. (1999),[d]
58 months BAT catalog	1092	Baumgartner et al. (2010)
Fourth IBIS catalog	723	Bird et al. (2010)
First AGILE catalog*	47	Pittori et al. (2009)
Third EGRET catalog*	271	Hartman et al. (1999)
EGR catalog*	189	Casandjian & Grenier (2008)
0FGL list*	205	(Abdo et al. 2009d, 0FGL)
1FGL catalog*	1451	(Abdo et al. 2010d, 1FGL)
2FGL catalog*	1873	(Nolan et al. 2012, 2FGL)
1FHL catalog*	514	(Ackermann et al. 2013a, 1FHL)
TeV point-like source catalog*	**82**	http://tevcat.uchicago.edu/
TeV extended source catalog[†]	66	http://tevcat.uchicago.edu/
LAT pulsars	147	Collaboration internal

Table 12
(Continued)

Name	Objects[a]	Reference
LAT identified	137	Collaboration internal

[a] Number of objects in the catalog.
[b] http://www.atnf.csiro.au/research/pulsar/psrcat
[c] All-sky surveys used only in the Likelihood Ratio method; see Section 5.2.1.
[d] The RASS Faint Source Catalog is available from http://www.xray.mpe.mpg.de/rosat/survey/rass-fsc/.

5.2. Automated Source Associations

Our approach for automated source association closely follows that used for the 2FGL, and details of the method are provided in Abdo et al. (2010d, 1FGL) and Nolan et al. (2012, 2FGL).

In summary, we use a Bayesian approach that trades the positional coincidence of possible counterparts with 3FGL sources against the expected number of chance coincidences to estimate the probability that a specific counterpart association is indeed real (i.e., a physical association). As for 1FGL and 2FGL, we retain counterparts as associations if they reach a posterior probability of at least 80%. We apply this method to a set of counterpart catalogs for which we calibrate the prior source association probabilities using Monte Carlo simulations of fake 3FGL catalogs.

Table 12 lists the catalogs used in the automatic association procedure, organized into four categories: (1) known or plausible γ-ray-emitting source classes, (2) surveys at other frequencies, (3) GeV sources, and (4) identified γ-ray sources. The first category allows us to assign 3FGL sources to object classes, while the second category reveals multiwavelength counterparts that may suggest the possible nature of the associated 3FGL sources. The third category allows assessment of former GeV detections of 3FGL sources, and the fourth keeps track of all firm identifications (see Section 5.1). For this last category we claim associations based on the spatial overlap of the true counterpart position with the 3FGL 99.9% confidence error ellipse.

With respect to 2FGL, we updated all catalogs for which more comprehensive compilations became available. As for 1FGL and 2FGL, we separately consider energetic and nearby pulsars, with spin-down energy flux $\dot{E}/d^2 > 5 \times 10^{32}$ erg kpc^{-2} s^{-1}. We also consider millisecond pulsars (MSPs) separately. For spin period P (s) and spin-down rate $\dot{P}$, we define MSPs as pulsars satisfying $\log_{10}\dot{P} + 19.5 + 2.5 \log_{10}P < 0$.

Catalogs indicated with an asterisk in Table 12 have source location uncertainties greater than those for the 3FGL sources. Catalogs indicated with a dagger have extended sources, with sizes greater than the source location uncertainty regions for 3FGL. For these catalogs we cannot apply the Bayesian association method. For the former catalogs we base associations on overlap of the 95% confidence error radii. For the latter, we require overlap between the extended source and the 95% confidence radius (semimajor axis) of the 3FGL source. These approaches are much less reliable than the Bayesian associations, so we do not claim any associations based on overlap in our final catalog. We record, however, any spatial overlap with a TeV source in the FITS file version of the catalog and use a special flag in our catalog (TEVCAT_FLAG), distinguishing point-like (P, angular diameter < 20′) from extended (E) TeV counterparts

(see Appendix B). We furthermore list all unassociated 3FGL sources that are spatially overlapping with SNRs or PWNe in Table 7.

5.2.1. Active Galactic Nuclei Associations

AGNs, and in particular blazars, are the largest class of associated sources in 3FGL at high Galactic latitudes.

In 3LAC, as in the Second LAT Catalog of AGNs (2LAC; Ackermann et al. 2011b), we added another association method to the automatic one described above. This is the LR method, frequently used to assess identification probabilities for radio, infrared, and optical sources (e.g., de Ruiter et al. 1977; Prestage & Peacock 1983; Sutherland & Saunders 1992; Lonsdale et al. 1998; Masci et al. 2001; Ackermann et al. 2011b). It is based on uniform surveys in the radio and in X-ray bands, enabling us to search for possible counterparts among the faint radio and X-ray sources. The LR method makes use of counterpart densities (assumed spatially constant over the survey region) through the log N − log s relation and therefore the source flux. This approach has been already used in 2LAC, and we refer the reader to Section 3.2 of that paper for a comprehensive description of the method, which computes the probability that a suggested association is the "true" counterpart.[92]

A source is considered as a likely counterpart of the γ-ray source if its reliability (see Equation (4) in 2LAC) is greater than 0.8 in at least one survey.

In total, our automatic association procedure based on the Bayesian method finds 1663 3FGL sources that are associated with AGNs, while the LR-based association method finds 1340 3FGL sources. For 405 sources only the Bayesian method provides an association, and for 82 sources only the LR method does so.

Overall, 3FGL includes 1745 sources associated with AGNs (58% of all 3FGL sources), of which 1145 are blazars, 573 are candidate blazars, 15 are radio galaxies, 5 are Seyfert galaxies, and 3 are other AGNs. The Seyfert galaxies are narrow-line Seyfert 1 galaxies that have been established as a new class of γ-ray active AGNs (Abdo et al. 2009f).

Comparing to 2FGL, we can make the following observations:

1. The 3FGL includes 610 more sources of AGN type than the 2FGL, i.e., a 76% increase. The fraction of new sources (not present in 2FGL) is slightly higher for hard-spectrum (i.e., $\Gamma < 2.2$) sources than for soft-spectrum ones (i.e., $\Gamma > 2.2$), 51% versus 47%, respectively, but the relative increase reaches 72% for very hard spectrum (i.e., $\Gamma < 1.8$) sources. In the 3FGL, 477 counterparts are new (81 FSRQs, 146 BL Lacs, 240 candidate blazars of unknown type, 10 non-blazar objects); the other counterparts were present in previous AGN *Fermi* catalogs but not included in any of the 0FGL, 1FGL, or 2FGL catalogs for various reasons (e.g., the corresponding γ-ray sources were not associated with AGNs, had more than one counterpart, or were flagged in the analysis).

---

[92] We note that the implementation of the LR method for the 2LAC associations was plagued with an error in the management of the sky coordinate precession that affected some of the associations. These false associations were also included in the active galaxy associations in 2FGL. The error has been fixed and the 2FGL associations re-derived. The corrected 2FGL catalog file has been delivered to the FSSC for distribution. In the present work, comparisons with 2FGL findings are based on this corrected set of associations.

2. The fraction of counterparts of unknown type (named "bcu") has increased notably between the two catalogs (from 20% to 28%). The number of these sources in the 3FGL has increased by more than a factor of 2.5 relative to that in the 2FGL, becoming almost equal to that of FSRQs. This increase is mainly due to the lower probability of having a published high-quality spectrum available for these fainter sources because of the lack of optical observing programs. In 3LAC, sources of the "bcu" type have been divided into three sub-types depending of the multiwavelength information available to characterize their "blazarness." In this paper we do not propagate this sub-division and refer to the 3LAC for census.

3. The relative increase in "bcu" drives a drop in the proportions of FSRQs and BL Lacs, which only represent 29% and 41% of the 3FGL, respectively (38% and 48% for 2FGL). The relative increase in the number of sources with respect to 2FGL is 34% and 42% for FSRQs and BL Lacs, respectively.

4. Out of 825 AGNs in the 2FGL, a total of 68 are missing in the full 3LAC sample, most of them due to variability effects. A few others are present in 3FGL but with shifted positions, ruling out the association with their former counterparts.

5.2.2. Normal Galaxies

The γ-ray emission of normal galaxies is powered by cosmic-ray interactions with interstellar gas and radiation. They are numerous but typically faint relative to active galaxies. The most luminous of the normal galaxies are starburst galaxies, which have very high densities of gas and massive star formation near their centers. Less distant are normal galaxies in the local group. As described above, we searched for associations with sources in catalogs of nearby galaxies and IRAS bright galaxies (Table 12).

In the 3FGL catalog we do not find additional associations with normal galaxies relative to those reported already in 2FGL: starburst galaxies M82 (3FGL J0955.4+6940), NGC 253 (3FGL J0047.5−2516) NGC 1068 (3FGL J0242.7−0001), and NGC 4945 (3FGL J1305.4−4926), and local group galaxies LMC (3FGL J0526.6−6825e), M31 (3FGL J0042.5 +4117), and the SMC (3FGL J0059.0−7242e).

Five sources in the 3FGL catalog lie within the extended source model for the LMC and are otherwise unassociated with counterparts at other wavelengths. These sources (3FGL J0456.2−6924, 3FGL J0524.5−6937, 3FGL J0525.2−6614, 3FGL 0535.3−6559, and 3FGL J0537.0−7113) are classified here as "gal" based solely on the spatial coincidence with the LMC, and their associations are listed as *LMC field*. Their particular natures remain uncertain.

5.2.3. Pulsars

Because pulsed emission can be such a clear signature, pulsars represent the largest class of firmly identified astrophysical objects in the 3FGL catalog. An extensive discussion of γ-ray pulsar properties is found in the 2FGL Catalog of Gamma-ray Pulsars (Abdo et al. 2013, 2PC). The public catalog of LAT-detected pulsars is regularly updated.[93]

At the time of the 3FGL association analysis, this catalog had 147 pulsars (Table 12). Only 137 of the LAT-detected pulsars have associations in the 3FGL catalog, however (Table 6). The missing 10 did not reach the TS $\geqslant 25$ criterion based on their average fluxes. Three of these are PSR J0737−3039A (Guillemot et al. 2013), J1640+2224, and J1705−1906 (Hou et al. 2014), and the remaining seven are flagged in the 2PC "spectral results" tables as either being too faint to fit or requiring an on-peak analysis to obtain spectra.

5.2.4. Pulsar Wind Nebulae

In addition to the four PWNe found in 2FGL (Crab, Vela-X, MSH 15−52, HESS J1825−137), the 3FGL catalog includes seven new PWN associations. Five of these are firm identifications because they are spatially extended LAT sources (see Table 1): HESS J1303−631 (3FGL J1303.0−6312e), HESS J1616−508 (3FGL J1616.2−5054e), HESS J1632−478 (3FGL J1633.0−4746e), HESS J1837−069 (3FGL J1836.5 −0655e), and HESS J1841−055 (3FGL J1840.9−0532e). The other two are positional associations with known PWNe: G279.8−35.8 (3FGL J0454.6−6825) and G0.13−0.11 (3FGL J1746.3−2859c).

5.2.5. Globular Clusters

Two globular cluster associations from the 2FGL catalog are not found in the 3FGL catalog.

1. 2FGL J1727.1−0704, previously associated with IC 1257, is found as 3FGL J1727.6−0654. This source is not formally associated with the globular cluster.
2. 2FGL J1824.8−2449, which was associated with NGC 6626, has been firmly identified as PSR J1824−2452A (Johnson et al. 2013). Its catalog listing is 3FGL J1824.6−2451.

The number of globular clusters associated with LAT sources does continue to grow. New associations are NGC 2608 (3FGL J0912.2−6452), NGC 6316 (3FGL J1716.6 −2812), NGC 6441 (3FGL J1750.2−3704), NGC 6541 (3FGL J1807.5−4343), NGC 6717 (3FGL J1855.1−2243), and NGC 6752 (3FGL J1910.7−6000). NGC 6752 had previously been noted as a likely LAT source by Tam et al. (2011b).

5.2.6. Supernova Remnants

Twelve SNRs are firmly identified in the 3FGL catalog as spatially extended sources (see Table 1). Six had previously appeared in the 2FGL catalog: IC 443, W28, W30, W44, W51C, and the Cygnus Loop. Additions are S147 (3FGL J0540.3+2756e, Katsuta et al. 2012), Puppis A (3FGL J0822.6 −4250e, Hewitt et al. 2012), Vela Jr. (3FGL J0852.7−4631e, Tanaka et al. 2011), RX J1713.7−3946 (3FGL J1713.5−3945e, Abdo et al. 2011d), Gamma Cygni (3FGL J2021.0+4031e, Lande et al. 2012), and HB21 (3FGL J2045.2+5026e, Reichardt et al. 2012; Pivato et al. 2013).

Additionally, we consider 11 unresolved 3FGL sources as being confidently associated with SNRs, based on individual studies of these SNRs in LAT data (see Ferrand & Safi-Harb 2012, and references therein).[94] These are given the "snr" designator (Table 6). The 2FGL sources that were designated

---

[93] See https://confluence.slac.stanford.edu/display/GLAMCOG/Public+List +of+LAT-Detected+Gamma-Ray+Pulsars.

[94] http://www.physics.umanitoba.ca/snr/SNRcat/

Table 13
Statistics of Source Associations

Category	0FGL	1FGL	2FGL	1FHL[a]	3FGL
Total	205	1451	1873	514	3033
Associated	168	821	1224	449	2023
Unassociated	37	630	649	65	1010
New γ-ray sources[b]	⋯	1265	762	52	1312
Sources associated with former LAT detections	⋯	186	1111	462	1721
Sources associated with former GeV detections[c]	74	162	170	4	206
Firmly identified sources	31	65	124	60	238
Sources associated with at least one object of known type	153	623	952	385	1398
Sources that have counterparts only in the multiwavelength catalogs	⋯	92	214	58	576

Notes.
[a] 1FHL: >10 GeV.
[b] Non-overlapping 95% source location confidence contours compared to previous LAT catalogs, at the level of overlapping 95% source location confidence contours.
[c] Here only the 1AGL, 3EG, and EGR catalogs are considered.

"snr" have been added to the "spp" class in 3FGL. Many of the 68 SNRs or PWNe in this table are spatially extended sources at other wavelengths, and therefore the chance probability of an overlap with an LAT source is non-negligible. As for previous LAT catalogs, we encourage great care in any analysis using these potential associations.

5.2.7. Binaries

Three HMB sources that appeared in 2FGL are also found in 3FGL: LS I+61 303 (3FGL J0240.5+6113), 1FGL J1018.6 −5856 (3FGL J1018.9−5856), and LS 5039 (3FGL J1826.2 −1450). All were firmly identified by binary periodicity. We note that each of the three is a TeV emitter but that the two other binary systems that have been detected in the TeV energy regime, HESS J0632+057 and PSR B1259−63, do not have counterparts in 3FGL. PSR B1259−63/LS 2883 is a bright LAT source during a small part of the 3.4 yr binary period following periastron (Abdo et al. 2011a; Tam et al. 2011a). HESS J0632 +057 has not been detected at all.

A fourth HMB from 2FGL, Cygnus X−3 (2FGL J2032.1 +4049), does not appear in 3FGL. It is an intermittent LAT source and was not active enough averaged over the 4 yr of this catalog to produce a significant detection. Eta Carinae, which appeared in 2FGL as a possible massive star association, is included as 3FGL J1045.1−5941, identified as a binary system. The LAT data exhibit the known 5.5 yr binary period (Reitberger et al. 2012, 2015). Although listed in the catalog as a nova, V407 Cygni is also a binary system. Its flaring activity in 2010 (Abdo et al. 2010h) was bright enough that it appears as 3FGL J2102.3+4547.

5.2.8. Multiwavelength Associations

In addition to the catalogs of classified sources, we also searched for associations with catalogs of radio and TeV sources. Our association procedure for AGNs heavily relies on associations with radio sources as most of the γ-ray-emitting AGNs are bright sources of radio emission (see Section 5.2.1). In fact, essentially all of the radio associations we find have been classified subsequently as AGNs.

We did not search for general associations with infrared, optical, or soft X-ray catalogs. Within the LAT source error regions we would find multiple potential counterparts, most of which necessarily would be due to chance, since many of the

sources in these catalogs are thermal in nature. We included, however, the hard X-ray catalogs *INTEGRAL*-IBIS and *Swift*-BAT and blazar candidates extracted from the infrared *WISE* catalog (D'Abrusco et al. 2014) in the automated association pipeline. These data, when included in a study of the SEDs to evaluate their synchrotron peak frequencies and general behaviors, help in understanding the natures of the candidate counterparts. This was done especially for all the sources classified as bcu/BCU and agn.

5.2.9. Statistics of Association Results

In total we find that 1976 of the 3033 sources in the 3FGL catalog (59%) have been associated with at least one non-GeV γ-ray counterpart by the automated procedures. Table 13 summarizes the association results.

5.3. GeV and TeV Source Associations

Through 2014 August, 155 flaring *Fermi*-LAT sources were detected and promptly reported in more than 249 Astronomer's Telegrams.[95] Of these sources, six are not in 3FGL. For two of these the flaring state was detected outside the time interval covered by 3FGL: S5 1044+71 (a 2FGL source classified as an FSRQ) and PMN J1626−2426 (in the proximity of an unassociated 2FGL source flagged as potentially contaminated by the diffuse emission). The other four are Cyg X−3 (an HMB associated with 2FGL J2032.1+4049; see Section 5.2.7), CGRaBS J1848+3219 (an FSRQ associated with 2FGL J1848.6+3241), PKS 1124−186 (an FSRQ associated with 2FGL J1126.6−1856), and PKS 2123−463 (an FSRQ associated with 2FGL J2125.0−4632). The reason that these three FSRQs are missing from the 3FGL catalog is probably that they have average fluxes below the detection threshold.

Sources in 3FGL that are positionally associated with sources seen by the ground-based TeV telescopes are of particular interest for broadband spectral studies. As for the 2FGL catalog, we studied associations with the TeVCat[96] compilation of sources detected by very high energy observatories. The energy threshold for TeVCat sources is not uniform, but it is typically greater than 100 GeV. We used a compilation of TeVCat sources prepared on 2014 October 27

---

[95] https://www.glast.stanford.edu/cgi-bin/pub_rapid
[96] http://tevcat.uchicago.edu

that has 148 unique entries. This comprises the so-called "Default" and "Newly Announced" TeV catalogs. We note that, as in 1FGL and 2FGL, the "Galactic center ridge" was not included for association purposes since it represents diffuse emission over an extended region along the Galactic plane (Aharonian et al. 2006).

This TeVCat compilation by its nature does not represent a complete survey, and our general statistical procedure for evaluating probabilities of chance association could not be applied. As for 2FGL, we separately considered point-like and extended TeVCat sources (Table 12). For point-like sources the criterion for association was overlapping 95% source location regions (indicated by "P" in the "TeV" column of Table 4). For extended sources (LAT or TeVCat) the criterion was spatial overlap within their respective angular extents (indicated by "E"). We note that, in the literature, the shapes of the extended TeV sources are usually approximated to a circle or to an ellipse. For the purposes of our association pipeline, we imposed a circular geometry on all extended TeV sources, setting the radius to the length of the semimajor axis. In the case of TeV sources whose morphologies depart significantly from a simple ellipse or a circle, this simplification of their geometry could lead to missed 3FGL associations.

In total, 124 3FGL sources have TeV counterparts. Of the 148 TeV sources considered, 117 have 3FGL associations and, out of these, 6 TeV sources have multiple 3FGL associations. Five of these are extended TeV sources and one is the Crab, which is associated with both the synchrotron and the inverse Compton Crab 3FGL sources (3FGL J0534.5+2201s/3FGL J0534.5+2201i). The TeV sources HESS J1018−589, Westerlund 2, HESS J1458−608, and MGRO J2019+37 have two 3FGL associations each, while Westerlund 1 has three 3FGL associations.

We note that the TeV source HESS J1018−589 has two components, denoted A (a point source) and B (extended emission). Of the two 3FGL associations, 3FGL J1018.9 −5856, an LAT high-mass binary, lies closer to location A, and 3FGL J1016.3−5858, an LAT pulsar, lies closer to location B.

Table 14 shows the associations between extended TeVCat sources and 3FGL catalog sources. Some of these, designated with e appended to their source names, were explicitly modeled as extended sources corresponding to H.E.S.S. sources (see Section 3.4).

Out of the 58 TeV AGNs, 57 have associated sources in 3FGL. Only HESS J1943+213, tentatively classified as a high-synchrotron peaked (HSP) blazar (HESS Collaboration 2011; Leahy & Tian 2012), does not have a 3FGL association. This presumed blazar is unique in the TeV sky in that it shines through the Galactic plane. We note that the VERITAS source VER J2016+371 is positionally associated with 3FGL J2015.6 +3709 although the VERITAS source is probably a PWN (Aliu et al. 2014) and the LAT source is associated with an FSRQ of unknown redshift.

The Milagro source, MGRO J2031+41, which comprises TeV J2032+4130, was also included as a separate source in the TeV list that was used to evaluate the associations with 3FGL because it is postulated that its emission is due to more than one source (Abdo et al. 2007). Due to the large extent of MGRO J2031+41 (1°.8; Abdo et al. 2012a), it has positional overlap with eight 3FGL sources in addition to 3FGL J2032.2+4126. We have listed just one LAT source 3FGL J2028.6+4110e, the Cygnus Cocoon, as being associated with MGRO J2031+41.

Table 14
Associations of 3FGL with Extended TeV Sources

TeVCat Name[a]	3FGL Name
Boomerang	J2225.8+6045, J2229.0+6114
CTA 1	J0007.0+7302
CTB 37A	J1714.5−3832
Geminga	J0633.9+1746
HESS J1018−589	J1016.3−5858, J1018.9−5856
HESS J1303−631	J1303.0−6312e
HESS J1356−645	J1356.6−6428
HESS J1458−608	J1456.7−6046, J1459.4−6053
HESS J1503−582	J1503.5−5801
HESS J1507−622	J1506.6−6219
HESS J1614−518	J1615.3−5146e
HESS J1616−508	J1616.2−5054e
HESS J1626−490	J1626.2−4911
HESS J1632−478	J1633.0−4746e
HESS J1640−465	J1640.4−4634c
HESS J1708−443	J1709.7−4429
HESS J1718−385	J1718.1−3825
HESS J1745−303	J1745.1−3011
HESS J1800−240	J1800.8−2402
HESS J1804−216	J1805.6−2136e
HESS J1809−193	J1810.1−1910
HESS J1825−137	J1824.5−1351e
HESS J1834−087	J1834.5−0841
HESS J1837−069	J1836.5−0655e
HESS J1841−055	J1840.9−0532e
HESS J1848−018	J1848.4−0141
HESS J1858+020	J1857.9+0210
IC 443	J0617.2+2234e
Kookaburra (Rabbit)	J1418.6−6058
Kookaburra PWN	J1420.0−6048
MGRO J1908+06	J1907.9+0602
MGRO J2019+37	J2021.1+3651, J2017.9+3627
MGRO J2031+41	J2028.6+4110e
MSH 15−52	J1514.0−5915e
RX J0852.0−4622	J0852.7−4631e
RX J1713.7−3946	J1713.5−3945e
SNR G292.2−00.5	J1119.1−6127
Terzan 5	J1748.0−2447
TeV J2032+4130	J2032.2+4126
Vela X	J0833.1−4511e
VER J2019+407	J2021.0+4031e
W 28	J1801.3−2326e
W 51	J1923.2+1408e
Westerlund 1	J1648.3−4611, J1650.3−4600, J1651.5−4626
Westerlund 2	J1023.1−5745, J1024.3−5757

Note.
[a] From http://tevcat.uchicago.edu.

Due to its large extent (2°.6), the Milagro Geminga source (Abdo et al. 2009h) has positional overlap with two 3FGL sources, 3FGL J0633.9+1746 (the Geminga pulsar) and the unidentified source 3FGL J0626.8+1743. We have associated only the Geminga pulsar with the Milagro source. Abdo et al. (2009h) postulate that the Milagro emission could be due to a pulsar-driven wind associated with Geminga.

The TeV sources Boomerang and SNR G103.3+02.7 have positional overlap at TeV energies. They are each positionally coincident with the same two 3FGL sources, the unidentified source 3FGL J2225.8+6045 and the pulsar, 3FGL J2229.0

+6114. We have associated SNR G103.3+02.7 with 3FGL J2225.8+6045 and Boomerang, classified as a PWN at TeV energies, with 3FGL J2229.0+6114, the LAT pulsar.

Relative to 2FGL, eight TeV sources are newly associated with LAT sources. All but one of these sources (HESS J1641 −463) had already been detected at TeV energies when 2FGL and 1FHL were released. None of these eight sources, however, have counterparts in those catalogs.

1. The H.E.S.S. Galactic Center source is associated with 3FGL J1745.6−2859c. The corresponding source 2FGL J1745.6−2858 had a large enough position offset that it was not considered associated with the TeV source. The Galactic center remains, however, a particularly complex region whose detailed study is beyond the scope of this paper.
2. Three HSP blazars (SHBL J001355.9−185406, 1ES 0229 +200, and 1ES 0347−121) are associated with 3FGL sources.
3. The shell SNR Tycho is associated with the faint LAT source 3FGL J0025.7+6404. Although the center of the TeV emission is offset by 0°.12 from the LAT source, the relatively large uncertainty of the LAT position indicates sufficient positional overlap for association.
4. The TeV PWN HESS J1809−193 is another new TeV association in 3FGL. Discovered at TeV energies in 2007, it is a relatively bright TeV source with an integral flux 14% that of the Crab Nebula in the same energy band (Aharonian et al. 2007).
5. The unidentified TeV sources HESS J1626−490 and HESS J1641−463 are also new TeV associations for 3FGL.

Thirty-one TeV sources have no counterparts in 3FGL; one of these, the unidentified extended TeV source HESS J1857 +026, has an association in 1FHL (1FHL J1856.9+0252). It is the only TeV source to have a 1FHL association but none in 2FGL or 3FGL. The other TeV sources having no counterparts in 3FGL comprise 10 other unidentified TeV sources, 10 PWNe, 2 binaries, 4 shell-type SNRs, 2 SNR–molecular cloud associations, 1 composite SNR (i.e., 9 out of the 19 SNRs in TeVCat), and the HSP blazars discussed earlier.

We note that two TeV sources, HESS J1634−472 and SNR W49B, were each associated with LAT sources in 2FGL and in 1FHL but do not have associations in 3FGL. A source coincident with W49B has been detected by the LAT, 3FGL J1910.9+0906, but this does not have positional overlap with the TeV detection of W49B.

The TeV source HESS J1427−608 had an association in 2FGL but was not associated with an LAT source in 1FHL and does not have an association in 3FGL.

5.4. Properties of Unassociated Sources

Among the 3033 sources in the 3FGL catalog, 2033 have associations or identifications with known astrophysical objects. Although that number is greater than the total number of sources in the 2FGL catalog, 1010 (33%) of the 3FGL sources remain unassociated. Among these unassociated sources are many that were found in previous LAT catalogs, indicating that some persistent mysteries remain despite extensive efforts to find associations over the past few years. The continued prevalence of unassociated sources is expected, as the improvement in sensitivity with 4 yr of flight data and
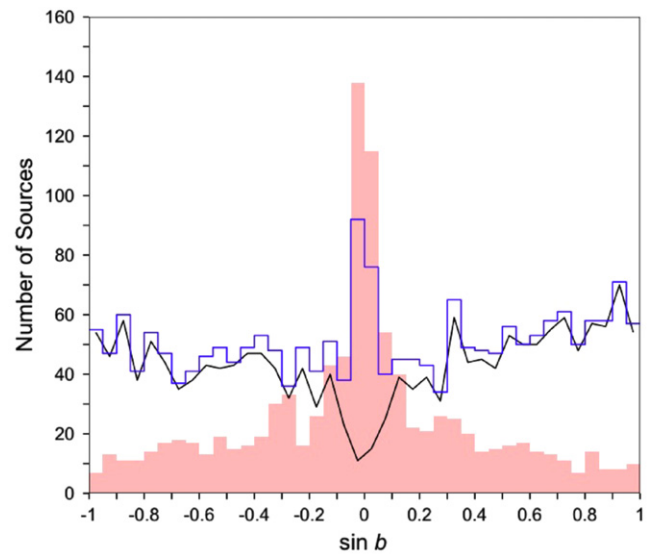

Figure 23. Distributions in Galactic latitude b of unassociated sources (shaded red region), all associated sources (blue histogram), and all active galaxy source classes (black line). Binned in $\sin b$, an isotropic distribution would be flat.

improvements to the characterization of backgrounds have allowed *Fermi*-LAT to probe the γ-ray sky to unprecedented depths. As a result, direct comparison to previous releases is difficult.

The distribution of unassociated sources on the sky is compared in Figure 23 to the distribution of the associated sources. The plot reveals some important features that should be kept in mind when considering unassociated 3FGL sources. Of the 992 unassociated sources in the 3FGL, 334 fall within the Galactic plane ($|b| < 5°$). This leaves 658 unassociated at $|b| > 5°$ sources for an average density of 1.75×10^{-2} sources deg^{-2}. While this density reflects the finite angular resolution and sensitivity of the instrument, some of the shortfall of associations is attributable to the fact that not all areas of the sky have been mapped uniformly at other wavelengths. For instance, a 3269 deg^2 "overlap region" in the north Galactic Cap intensively covered by five radio catalogs GB6 (6 cm), FIRST (20 cm), NVSS (20 cm), WNSS (92 cm), and VLSSr (4 m), as well as by the Sloan Digital Sky Survey (DR9) optical survey (Kimball & Ivezić 2008), contains only 31 unassociated sources. The corresponding density of unassociated sources is 9.48×10^{-3} sources deg^{-2}, nearly half of the overall average.

Within the Galactic plane, the unassociated source population is a combination of both Galactic and extragalactic source classes. Outside the plane, the LAT-detected AGN source density is 0.045 deg^{-2}. By extrapolation, this implies that there should be 160 detectable AGNs within the 10° band surrounding the Galactic plane (not accounting for incompleteness of AGN catalogs at low latitudes). Only 56 sources are associated with active galaxies in this region. At low latitudes the LAT detection threshold is higher, and catalogs of active galaxies are incomplete, but extrapolation from higher latitudes suggests that fewer than ~100 of the unassociated sources in the region $|b| < 5°$ could be active galaxies.

Of the remaining unassociated sources, we expect most to be Galactic objects. If we use the fractions of Galactic associated sources in this latitude range as a guide, we find that nearly half

should be pulsars (47%), and most of the remainder should be SNRs (44%), with only a small number of other Galactic sources (9%). These yet-to-be-detected pulsars may never be seen to pulse: part of the neutron star population will have magnetic and rotation axis orientations causing γ-ray emission to be spread over a large part of the rotation phase (Hou et al. 2014). This, combined with a low γ-ray flux in the presence of high background, renders blind periodicity searches insensitive to pulsations (Dormody et al. 2011). That many of these sources are likely to be previously undetected SNRs is also reasonable. Ackermann et al. (2012b) recognized that the distribution of unassociated LAT sources near the Galactic plane matched the scale height appropriate for Population I objects, such as the SNR parent population of massive stars.

It should be emphasized that a substantial fraction of the unassociated sources (40%) has at least one analysis flag set (Section 3.9). We find that 57% of the sources with at least one flag have $|b| < 5°$, which reflects the complexity of the Galactic diffuse emission (Sections 3.7.3 and 3.8). Because of the difficulties in source detection against the bright diffuse background along the Galactic plane, unassociated sources with analysis flags set should be considered with caution. That difficulty is acute in the Galactic bulge (within 5° of the Galactic center), in the Vela ($l \sim 268°$) and Cygnus ($l \sim 80°$) regions. The immediate vicinity of the Galactic center is particularly uncertain, with seven sources within 1°, on top of bright diffuse emission. We did not attempt in the framework of 3FGL to devise models dedicated to those regions, so the source positions and characteristics there are not as reliable as in the extragalactic sky.

We also note a number of clusters of unassociated sources, mostly near the Galactic plane. Obvious ones are near $(l, b) = (133.5, +1), (340, -2)$. Since there is no specific search for extended sources in 3FGL, many of those clusters are probably extended sources (SNRs, PWNe, star formation regions). The extended sources that are currently declared (Section 3.4) are all relatively bright, with a median significance of 32σ. This leaves a lot of room for fainter extended sources.

6. GALACTIC SOURCE NUMBER COUNTS

The 3LAC companion paper discusses briefly the source number counts of extragalactic sources. Here we address the Galactic source number counts, following the analysis for the 1FHL catalog, which was based on the method described by Strong (2007), and which addressed energies above 10 GeV. For 3FGL we use energies above 1 GeV. Photon fluxes over that energy range (F_{35} of Table 4) are more accurate than over the full band, as explained in the 2FGL paper. The much larger number of sources in 3FGL compared to 1FHL means that the entire analysis is more robust.

The motivation for performing a Galactic source population analysis is first to obtain estimates of the global source characteristics, i.e., space density and luminosity function, second to estimate the contribution from sources below the detection threshold to the Galactic "diffuse" emission, and third to generate templates of this emission, to be incorporated into diffuse emission models for future source catalogs. Source population analysis also puts the detected sources in the context of the total source content of the Galaxy.

The method is guided by properties of known sources such as pulsars but does not attempt physical modeling of the sources. The approach is essentially geometrical; nevertheless, the analysis reveals the basic properties of the source population. We refer to the modeling of the source population(s) as *population synthesis*. Since the population synthesis includes all sources down to arbitrarily low flux levels (for a given model), it can also be used to study the flux limit of the actual catalog and assess how the observed source number counts are affected by the detection procedure. This serves as a consistency check on other methods of assessing the detection threshold.

An essential principle is to use the fact that low-latitude sources probe the high-luminosity, low-space-density objects at large distances, while the high-latitude sources constrain the low-luminosity, high-space-density nearby objects.

This is because high-luminosity sources are rare but visible to large distances that are only sampled in the Galactic plane, while low-luminosity sources are common but only visible when nearby, so they dominate outside the plane. These samples are complementary and allow the full luminosity function to be estimated.

6.1. Source Population Synthesis

The population synthesis and subsequent analysis are performed using the GALPLOT software, which is publicly available.[97] Let L_γ be the luminosity of a source in photons s^{-1} in some energy range. We use photon luminosities since they are most directly related to the detectability of sources and detection thresholds. The luminosity function at galactocentric distance R and distance from Galactic plane z is the space density of sources per unit luminosity $\rho(L_\gamma, R, z)$. The shape of the luminosity function is assumed independent of position, i.e., $\rho(L_\gamma, R, z)$ is separable in L_γ and (R,z). After Strong (2007), we assume that the luminosity function depends on luminosity as $L_\gamma^{-\alpha}$ for $L_{\gamma,\mathrm{min}} < L_\gamma < L_{\gamma,\mathrm{max}}$ and is zero outside these limits. The total space density of sources is $\rho(R, z) = \int \rho(L_\gamma, R, z) \, dL_\gamma$, which we normalize to the value $\rho_\odot$ at $(R, z) = (R_\odot, 0)$. For a source of luminosity L_γ at distance d the flux is $S_\gamma = L_\gamma/4\pi d^2$. The differential source number counts are defined as $N(S_\gamma)$ sources per unit flux over the area of sky considered. At lower S_γ, both the luminosity function and the spatial boundaries influence $N(S_\gamma)$. For this analysis the source fluxes are binned in $\log(S_\gamma)$ so that the plotted distributions are proportional to $S_\gamma N(S_\gamma)$; we use 5 bins per decade of S_γ, appropriate to the statistics available. We use standard Monte Carlo techniques to sample $\rho(L_\gamma, R, z)$ throughout the Galaxy, using oversampling to reduce statistical fluctuations if necessary. We use the sources generated from such simulations to form simulated catalogs extending below the 3FGL flux limit and compare the flux distributions with the observations.

In the present work we do not explicitly account for the source detection efficiency in 3FGL, but simply compare the predictions with the data mindful of the range of the estimated detection threshold. Since the detection efficiency and threshold depend on direction, mainly because of the Galactic diffuse emission, and also exposure variations, accounting for this
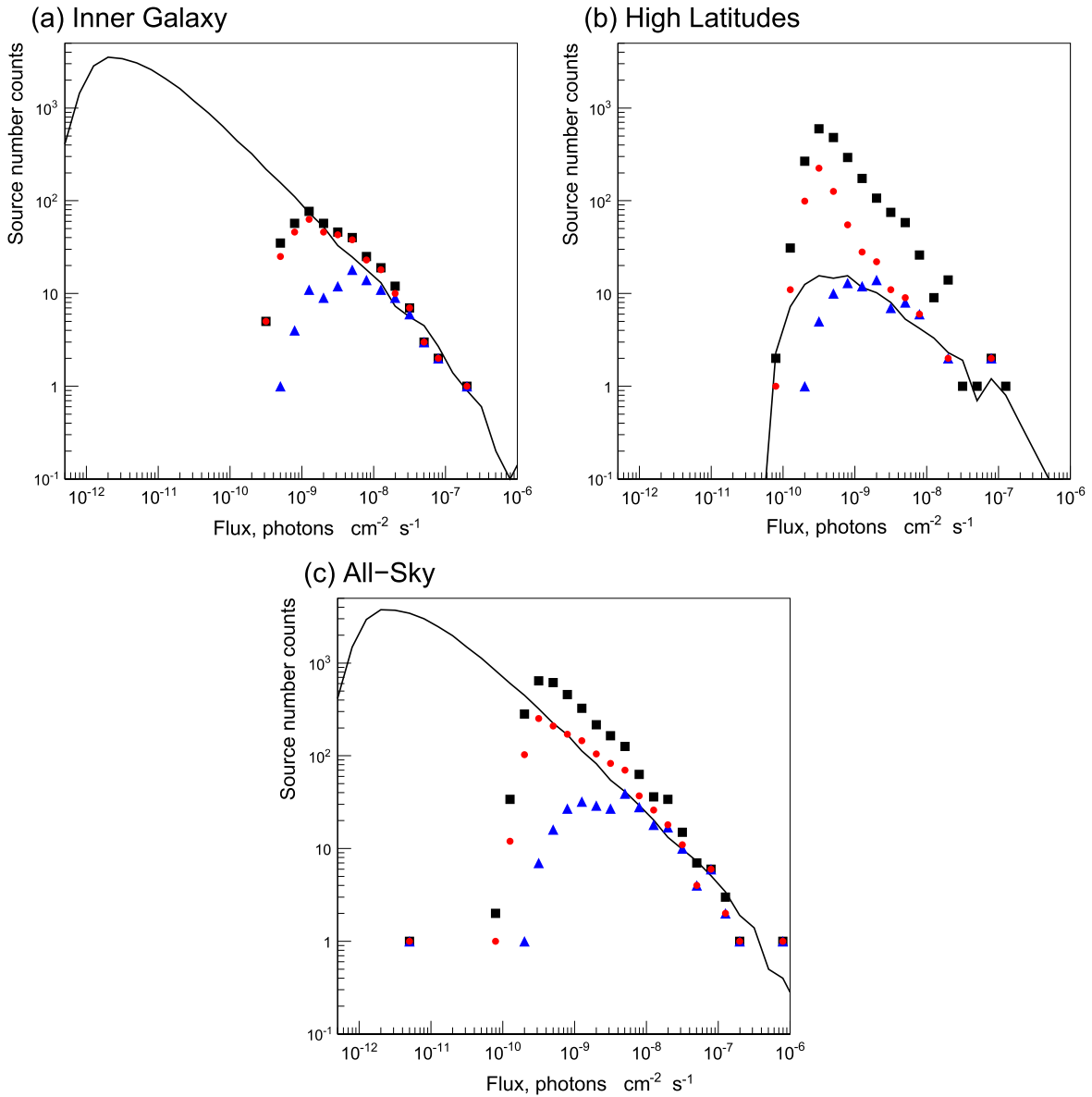

Figure 24. Dependence of source number counts (number of sources per 0.2 dex) on source photon flux *S* above 1 GeV. The markers are source number counts from the 3FGL catalog; blue triangles are identified and associated Galactic sources, red circles are identified and associated Galactic, and unassociated sources, and black squares are all sources including extragalactic (for reference). The curves are from the reference model described in the text. (a) Inner Galaxy ($|b| < 10°$, $300° < l < 60°$); (b) high latitudes ($|b| > 10°$, all longitudes); (c) all-sky.

would require considerably more study than possible in the present work, and is not required for the scope here.

A large number of models were generated and compared with the data; for this paper we choose one reference model that is found to reproduce the data satisfactorily but is not unique. This suffices to illustrate plausible properties of the Galactic source population. A complete study of source number counts, optimizing the model over all parameters and considering spatial distributions and more sky regions, or using information about particular source classes, is beyond the present paper and is foreseen in a future work.

6.2. Model and Comparison with Data

Our reference model for the luminosity function has $\rho_\odot = 100$ kpc^{-3} and an $L_\gamma^{-1.8}$ dependence on luminosity in

the range $2 \times 10^{34} - 2 \times 10^{39}$ photons s^{-1} above 1 GeV. The luminosity law is discussed in Strong ([2007](#)); the chosen power-law index 1.8 is larger than expected for normal pulsars (1.5 or less) or MSPs, but here we wish to encompass both of these source types, and also other sources like SNRs, with a single power-law function, for simplicity. This index is required to fit $N(S_\gamma)$ at both low and high latitudes; the steep slope ensures enough low-luminosity sources to match high-latitude number counts.

The distribution in galactocentric distance is based on the model of Lorimer et al. ([2006](#)) for the distribution of pulsars, taken as representative of Galactic sources. We adopt an exponential scale height of 500 pc, guided by that of pulsars; the source number count distribution $N(S_\gamma)$ depends only weakly on the scale height. This distribution peaks near $R = 4$ kpc and falls to zero at $R = 0$; it was chosen for

illustration and has not been optimized for the 3FGL source number counts. The spectrum of sources was taken as a power-law with exponential cutoff, index 1.4, and cutoff energy 3.2 GeV, with correlated dispersion in these parameters as found for pulsars. This is representative of pulsars but is not critical for this work since we use integral photon fluxes above 1 GeV as the basis for the analysis of $N(S_\gamma)$. The spectrum is used here only when comparing with the spectrum of interstellar emission, to estimate the contribution of sources to the diffuse emission (Section 6.3).

Figure 24 compares the simulated $N(S_\gamma)$ with the observed flux distributions of 3FGL sources at low latitudes in the inner Galaxy ($|b| < 10°$, $300° < l < 60°$) and high latitudes ($|b| > 10°$), as well as for the full sky for reference. The predictions agree reasonably with Galactic plus unassociated sources at low latitudes, and with Galactic associated sources at high latitudes (where unassociated sources are probably mainly AGNs). At high latitudes it is important that the model does not overpredict Galactic plus unassociated sources, and this condition is satisfied. The reference model is consistent with the low-latitude source number counts, having the observed dependence on flux above the source detection threshold; the slope reflects the spatial distribution (independent of the shape of the luminosity function) above 10^{-8} photons cm^{-2} s^{-1}, while the distributions for both the model and observed source number counts flatten at lower fluxes, following the luminosity function.

Some of the unassociated sources in the inner Galaxy may be AGNs; using high-latitude AGNs and unassociated sources (which are probably mainly AGNs) and scaling by solid angle, we estimate about 30 AGNs above the threshold for the inner Galaxy. This can be compared to 254 Galactic identified plus associated sources in the inner Galaxy for the same threshold, so that the AGNs contribution is negligible, especially considering that most of these should be identified/associated AGNs and hence excluded from our sample. For comparison, there are 33 (identified/associated) AGNs in this region, similar to our estimate from high latitudes, so the selection of Galactic classes certainly avoids the presence of more than a few AGNs among the unassociated sources.

Pulsars, including MSPs, have a range of luminosities 10^{32}–10^{37} erg s^{-1} (Abdo et al. 2013), corresponding to about 3×10^{34}–3×10^{39} photons s^{-1} (taking a mean energy 2 GeV $= 3.2 \times 10^{-3}$ erg). This is consistent with the range we have found from our $N(S_\gamma)$ analysis at low and high latitudes, although we are not assuming anything about the physical nature of the sources.

In this model there are 2.9×10^4 sources in the Galaxy (in the luminosity range considered), with a total luminosity >1 GeV of 2×10^{40} photons s^{-1}, or about 6×10^{37} erg s^{-1}. 3FGL contains about 266 Galactic sources (identified plus associated in Table 6), so that the LAT detects about 1% of the sources in the Galaxy; allowing for a significant number of unassociated sources at low latitudes being Galactic, a larger number is certainly included in 3FGL. Figure 24 shows that the distribution of simulated sources (in the reference model) continues down to fluxes $\sim$100 times below the detection threshold, the cutoff being due to the finite spatial extent of the Galaxy. The ratio of total flux below threshold to above threshold is about 0.25, which gives an estimate of the

Table 15
LAT 3FGL FITS Format: ROI Extension

Column	Format	Unit	Description
ROI_num	I		ROI number (cross-reference to main table)
RAJ2000	E	deg	R.A. of ROI center
DEJ2000	E	deg	Decl. of ROI center
GLON	E	deg	Galactic longitude of ROI center
GLAT	E	deg	Galactic latitude of ROI center
Radius	E	deg	ROI radius (unbinned mode) or half-side (binned mode)
PARNAMi[a]	E	⋯	Value of diffuse model parameter i
Unc_PARNAMi	E	⋯	1σ error on PARNAMi

Note.
[a] Two columns (value and error) for each diffuse model parameter. The parameter name is given by the PARNAMi keyword in the extension header.

contribution of the undetected sources to the "diffuse" emission (see below).

Using the work of Watters & Romani (2011), we can estimate the number of γ-ray pulsars in the Galaxy; they give a pulsar birthrate of 1 per 59 yr, which corresponds to 1.7×10^4 pulsars up to age 1 Myr. This is consistent with our model; we include other classes of sources, but this shows that our value is plausible.

6.3. Contribution of Undetected Sources to Diffuse Galactic Emission

Judging from the turnover in the inner Galaxy $N(S_\gamma)$ data, the detection threshold there is about 1×10^{-9} photons cm^{-2} s^{-1}, and we adopt this for the following estimates. For the inner Galaxy, the total flux from sources is 3×10^{-6} photons cm^{-2} s^{-1}, with 2.4×10^{-6} photons cm^{-2} s^{-1} above threshold, 0.6×10^{-6} photons cm^{-2} s^{-1} below threshold. So 20% of the total source flux is below threshold, and the ratio of flux below/above threshold is 25%. We can use the measured diffuse spectrum directly, comparing with the contribution from sources relative to interstellar emission: for the inner Galaxy as defined here, this gives 12% from sources above threshold, 3% from sources below threshold, at 1 GeV. These estimates are clearly model dependent, in particular the adopted luminosity function gives a large number of low-luminosity sources, but they are certainly of the correct order, since varying the models within the range consistent with the data does not change the estimates greatly; details are beyond the scope of this paper.

For comparison with our estimates, Watters & Romani (2011) used physical modeling of young pulsars and estimated their contribution to diffuse emission as 2.8%, however using all-sky averages and for only 6 months of LAT data taking. A study of the MSP contribution to the Galactic emission, for energies above 100 MeV, has been given by Grégoire & Knödlseder (2013); they find that the contribution is at the few percent level.

Population synthesis can be used to estimate the increase in the number of sources with improved detection limits; in this model, reducing the threshold by a factor 2 would yield about twice as many sources at low latitudes.
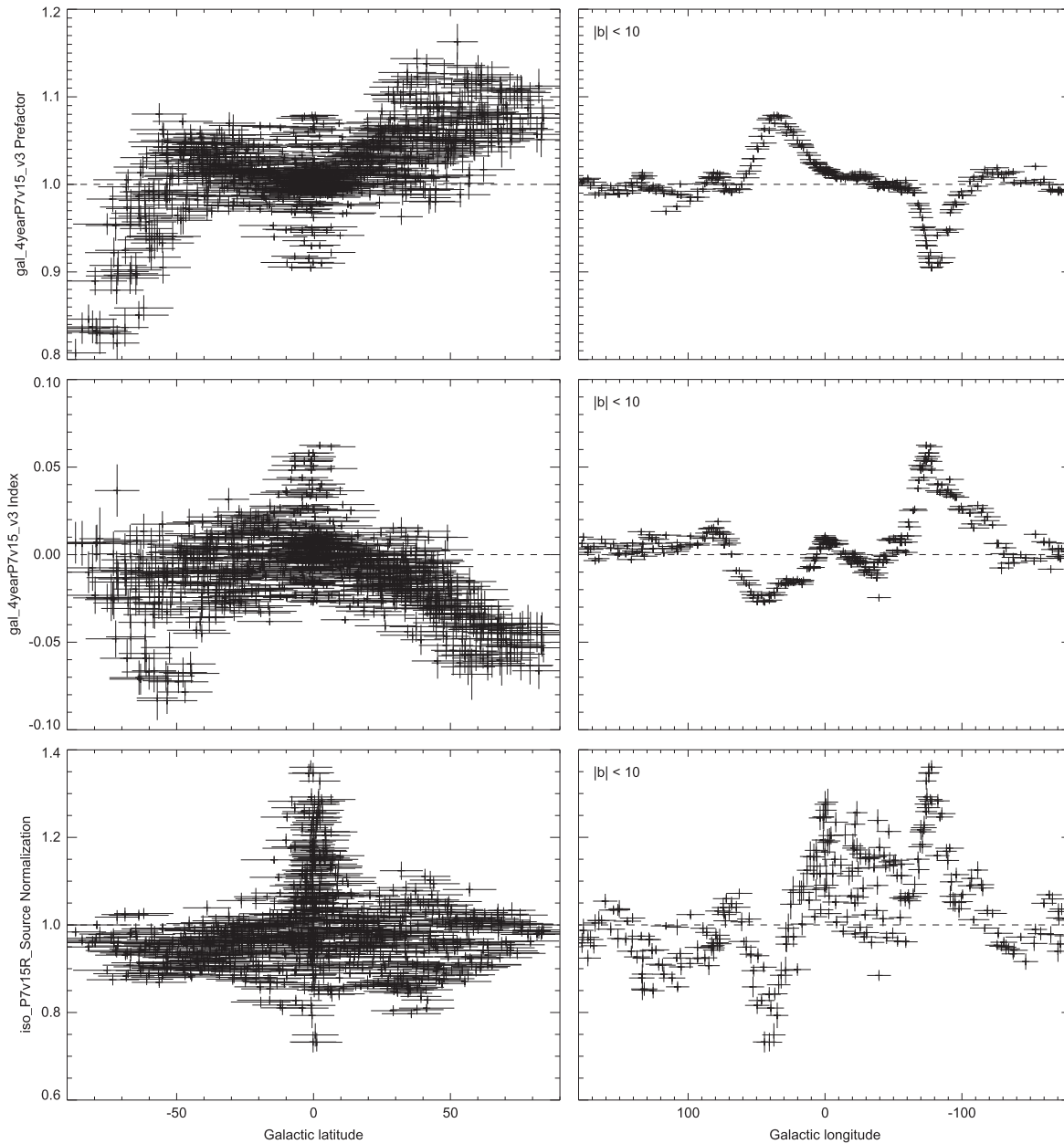
Figure 25. Diffuse model parameters in each RoI. The horizontal error bar is the RoI radius. The vertical error bar is the statistical error from the fit. The vertical scale is the same in the left and right plots for a given parameter. Top: normalization of the Galactic diffuse component (at 500 MeV). Center: spectral index of the power-law correction to the Galactic diffuse component (positive means a harder model). Bottom: normalization of the isotropic component. Left: all values as a function of Galactic latitude. Right: Galactic plane only as a function of Galactic longitude.

Finally, we consider the global picture. The luminosity of the interstellar emission from cosmic-ray interactions is about 1×10^{41} photons s^{-1} or 4×10^{38} erg s^{-1} for energies above 1 GeV (Strong et al. 2010), so that sources have about 20% of the interstellar luminosity. This is also an estimate of the contribution of all Galactic sources to the total Galactic γ-ray intensity, averaged over the sky.

7. CONCLUSIONS

The third *Fermi* LAT catalog is the deepest yet in the 100 MeV–300 GeV energy range. The increased sensitivity relative to the 2FGL catalog is due to both the longer time interval (4 yr versus 2 yr for 2FGL) and the use of reprocessed Pass 7 data, which provides a narrower PSF above 3 GeV. The 3FGL catalog also benefits from higher-level improvements in the analysis, including an improved model for Galactic diffuse emission and a refined method for source detection.

The 3FGL catalog includes 3033 sources. The sources are detected (TS > 25) based on their average fluxes in the 4 yr data set; 647 of the sources are found to be significantly variable on monthly timescales. We flag 78 (2.6%) of the sources as potentially being related to imperfections in the model for Galactic diffuse emission; the character c is appended to their names. An additional 572 (18.9%) are flagged in the catalog for less serious concerns, e.g., for the spectral model having a poor fit or for being close to a brighter

Table 16
LAT 3FGL FITS Format: LAT_Point_Source_Catalog Extension

Column	Format	Unit	Description
Source_Name	18A	⋯	Official source name 3FGL JHHMM.m+DDMM
R.A.J2000	E	deg	R.A.
DEJ2000	E	deg	Decl.
GLON	E	deg	Galactic longitude
GLAT	E	deg	Galactic latitude
Conf_68_SemiMajor	E	deg	Long radius of error ellipse at 68% confidence
Conf_68_SemiMinor	E	deg	Short radius of error ellipse at 68% confidence
Conf_68_PosAng	E	deg	Position angle of the 68% long axis from celestial north, positive toward increasing R.A. (eastward)
Conf_95_SemiMajor	E	deg	Long radius of error ellipse at 95% confidence
Conf_95_SemiMinor	E	deg	Short radius of error ellipse at 95% confidence
Conf_95_PosAng	E	deg	Position angle of the 95% long axis from celestial north, positive toward increasing R.A. (eastward)
ROI_num	I	⋯	ROI number (cross-reference to ROIs extension)
Signif_Avg	E	⋯	Source significance in σ units (derived from test statistic) over the 100 MeV–300 GeV band
Pivot_Energy	E	MeV	Energy at which error on differential flux is minimal
Flux_Density	E	cm^{-2} MeV^{-1} s^{-1}	Differential flux at Pivot_Energy
Unc_Flux_Density	E	cm^{-2} MeV^{-1} s^{-1}	1σ error on differential flux at Pivot_Energy
Spectral_Index	E	⋯	Best-fit photon number power-law index: for LogParabola spectra, index at Pivot_Energy; for PL(Super)ExpCutoff spectra, low-energy index
Unc_Spectral_Index	E	⋯	1σ error on Spectral_Index
Flux1000	E	cm^{-2} s^{-1}	Integral photon flux from 1 to 100 GeV
Unc_Flux1000	E	cm^{-2} s^{-1}	1σ error on integral photon flux from 1 to 100 GeV
Energy_Flux100	E	erg cm^{-2} s^{-1}	Energy flux from 100 MeV to 100 GeV obtained by spectral fitting
Unc_Energy_Flux100	E	erg cm^{-2} s^{-1}	1σ error on energy flux from 100 MeV to 100 GeV
Signif_Curve	E	⋯	Significance (in σ units) of the fit improvement between power-law and either LogParabola (for ordinary sources) or PLExpCutoff (for pulsars) A value greater than 4 indicates significant curvature
SpectrumType	18A	⋯	Spectral type (PowerLaw, LogParabola, PLExpCutoff, PLSuperExpCutoff)
beta	E	⋯	Curvature parameter (β of Equation (1)) for LogParabola; NULL for other spectral types
Unc_beta	E	⋯	1σ error on β for LogParabola; NULL for other spectral types
Cutoff	E	MeV	Cutoff energy (E_c of Equation (2)) for PL(Super)ExpCutoff; NULL for other spectral types
Unc_Cutoff	E	MeV	1σ error on cutoff energy for PL(Super)ExpCutoff; NULL for other spectral types
Exp_Index	E	⋯	Exponential index (b of Equation (2)) for PLSuperExpCutoff; NULL for other spectral types
Unc_Exp_Index	E	⋯	1σ error on exponential index for PLSuperExpCutoff; NULL for other spectral types
PowerLaw_Index	E	⋯	Best fit power-law index; equal to Spectral_Index if SpectrumType is PowerLaw
Flux30_100	E	cm^{-2} s^{-1}	Integral photon flux from 30 to 100 MeV (not filled)
Unc_Flux30_100	2E	cm^{-2} s^{-1}	1σ lower and upper error on integral photon flux from 30 to 100 MeV (not filled)
nuFnu30_100	E	erg cm^{-2} s^{-1}	Spectral energy distribution between 30 and 100 MeV (not filled)
Sqrt_TS30_100	E	⋯	Square root of the test statistic between 30 and 100 MeV (not filled)
Flux100_300	E	cm^{-2} s^{-1}	Integral photon flux from 100 to 300 MeV
Unc_Flux100_300	2E	cm^{-2} s^{-1}	1σ lower and upper error on integral photon flux from 100 to 300 MeV[a]
nuFnu100_300	E	erg cm^{-2} s^{-1}	Spectral energy distribution between 100 and 300 MeV
Sqrt_TS100_300	E	⋯	Square root of the test statistic between 100 and 300 MeV
Flux300_1000	E	cm^{-2} s^{-1}	Integral photon flux from 300 MeV to 1 GeV
Unc_Flux300_1000	2E	cm^{-2} s^{-1}	1σ lower and upper error on integral photon flux from 300 MeV to 1 GeV[a]
nuFnu300_1000	E	erg cm^{-2} s^{-1}	Spectral energy distribution between 300 MeV and 1 GeV
Sqrt_TS300_1000	E	⋯	Square root of the test statistic between 300 MeV and 1 GeV
Flux1000_3000	E	cm^{-2} s^{-1}	Integral photon flux from 1 to 3 GeV
Unc_Flux1000_3000	2E	cm^{-2} s^{-1}	1σ lower and upper error on integral photon flux from 1 to 3 GeV[a]
nuFnu1000_3000	E	erg cm^{-2} s^{-1}	Spectral energy distribution between 1 and 3 GeV
Sqrt_TS1000_3000	E	⋯	Square root of the test statistic between 1 and 3 GeV
Flux3000_10000	E	cm^{-2} s^{-1}	Integral photon flux from 3 to 10 GeV
Unc_Flux3000_10000	2E	cm^{-2} s^{-1}	1σ lower and upper error on integral photon flux from 3 to 10 GeV[a]
nuFnu3000_10000	E	erg cm^{-2} s^{-1}	Spectral energy distribution between 3 and 10 GeV
Sqrt_TS3000_10000	E	⋯	Square root of the test statistic between 3 and 10 GeV
Flux10000_100000	E	cm^{-2} s^{-1}	Integral photon flux from 10 to 100 GeV
Unc_Flux10000_100000	2E	cm^{-2} s^{-1}	1σ lower and upper error on integral photon flux from 10 to 100 GeV[a]
nuFnu10000_100000	E	erg cm^{-2} s^{-1}	Spectral energy distribution between 10 and 100 GeV
Sqrt_TS10000_100000	E	⋯	Square root of the test statistic between 10 and 100 GeV
Variability_Index	E	⋯	Sum of $2 \times \log$(Likelihood) difference between the flux fitted in each time

Table 16
(Continued)

Column	Format	Unit	Description
			interval and the average flux over the full catalog interval; a value greater
			than 72.44 over 48 intervals indicates <1% chance of being a steady source
Signif_Peak	E	⋯	Source significance in peak interval in σ units
Flux_Peak	E	cm^{-2} s^{-1}	Peak integral photon flux from 100 MeV to 100 GeV
Unc_Flux_Peak	E	cm^{-2} s^{-1}	1σ error on peak integral photon flux
Time_Peak	D	s (MET)	Time of center of interval in which peak flux was measured
Peak_Interval	E	s	Length of interval in which peak flux was measured
Flux_History	48E	cm^{-2} s^{-1}	Integral photon flux from 100 MeV to 100 GeV in each interval (best fit from
			likelihood analysis with spectral shape fixed to that obtained over full interval)
Unc_Flux_History	2×48E	cm^{-2} s^{-1}	1σ lower and upper error on integral photon flux in each interval
			added in quadrature with 2% systematic component
Extended_Source_Name	18A	⋯	Cross-reference to the ExtendedSources extension for extended sources, if any
0FGL_Name	18A	⋯	Name of corresponding 0FGL source, if any
1FGL_Name	18A	⋯	Name of corresponding 1FGL source, if any
2FGL_Name	18A	⋯	Name of corresponding 2FGL source, if any
1FHL_Name	18A	⋯	Name of corresponding 1FHL source, if any
ASSOC_GAM1	18A	⋯	Name of likely corresponding 1AGL source
ASSOC_GAM2	18A	⋯	Name of likely corresponding 3EG source
ASSOC_GAM3	18A	⋯	Name of likely corresponding EGR source
TEVCAT_FLAG	A	⋯	P if positional association with non-extended source in TeVCat
			E if associated with a more extended source in TeVCat, N if no TeV association
ASSOC_TEV	24A	⋯	Name of likely corresponding TeV source from TeVCat
CLASS1	5A	⋯	Class designation for associated source; see Table 6
ASSOC1	26A	⋯	Name of identified or likely associated source
ASSOC2	26A	⋯	Alternate name of identified or likely associated source
Flags	I	⋯	Source flags (binary coding as in Table 3)[b]

Notes.
[a] Separate 1σ errors are computed from the likelihood profile toward lower and larger fluxes. The lower error is set equal to NULL, and the upper error is derived from a Bayesian upper limit if the 1σ interval contains 0 (TS < 1; see Section 3.5).
[b] Each condition is indicated by one bit among the 16 bits forming `Flags`. The bit is raised (set to 1) in the dubious case, so that sources without any warning sign have `Flags = 0`.

source. Of the 3033 sources in the catalog, 238 (7.8%) are considered identified, based on correlated variability or (for 25 of the identified sources) correlated angular sizes with observations at other wavelengths. Of the remainder, we find likely lower-energy counterparts for 1786 sources (59.6%). The remaining 992 sources (32.7%) are unassociated.

The identified and associated sources in the 3FGL catalog include many Galactic and extragalactic source classes. The largest Galactic source class continues to be pulsars, with 143 known γ-ray pulsars and 24 candidates. Other Galactic source classes have continued to grow; 15 globular clusters are now associated with LAT sources. Our analysis of Galactic source counts, informed by a model for the luminosity function, suggests that at 1 GeV $\sim$3% of the Galactic diffuse emission is due to unresolved Galactic sources. Blazars remain the largest class of extragalactic source, with more than 1100 identified or associated with BL Lac or FSRQ active galaxies. Non-blazar classes of active galaxies are also found, including a Seyfert galaxy (Circinus galaxy), a compact steep spectrum radio source (3C 286), and several radio galaxies. The populations of active galaxies in 3FGL are considered in more detail in the companion 3LAC catalog.

_____
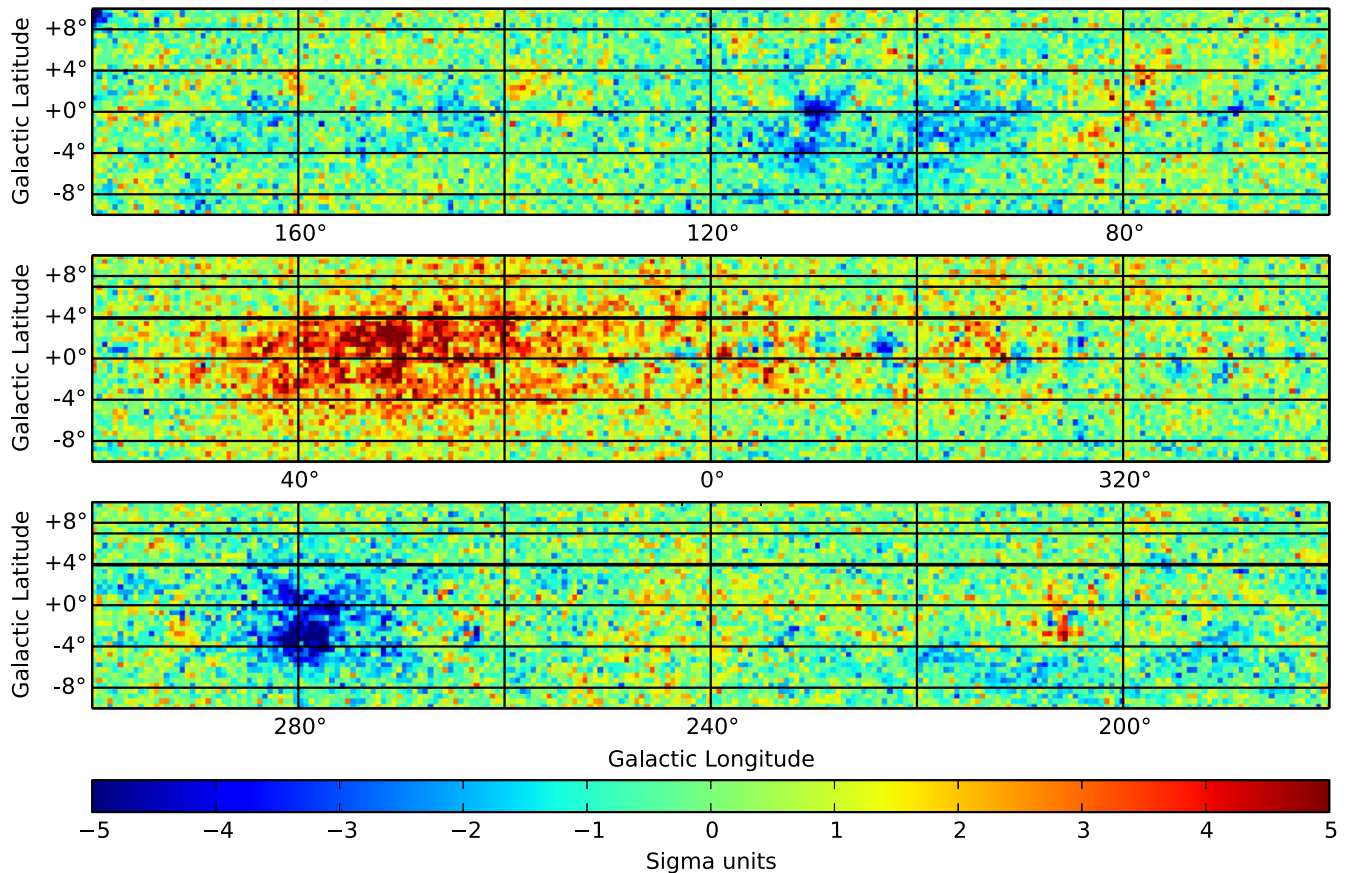[98] http://www.atnf.csiro.au/research/pulsar/psrcat

Figure 26. Residuals when setting the diffuse model normalizations to 1 and no power-law correction, integrated from 100 MeV to 100 GeV and expressed in sigma units over $0°.5$ pixels. Top: positive Galactic longitudes from the anticenter to Cygnus. Center: Galactic ridge. Bottom: negative Galactic longitudes from Carina to the anticenter.

This research has made use of Aladin,[99] TOPCAT[100] and APLpy, an open-source plotting package for Python.[101] The authors acknowledge the use of HEALPix[102] (Górski et al. 2005).

Facilities: Fermi.

APPENDIX A
DIFFUSE MODEL ADJUSTMENTS

In Section 3.2 we noted that the diffuse emission model has three free parameters in each RoI. We report their values in the ROI extension of the catalog (Table 15), and we show in Figure 25 how they vary over the sky. The first thing to notice is that the amplitude of the variations is relatively small. Overall the Galactic normalization does not vary by more than 20%, and in the Galactic plane (i.e., where it is the dominant component) it does not vary by more than 10%. The slope of the power-law correction does not exceed 0.1 (positive or negative), and inside the plane it does not exceed 0.05. The isotropic normalization does not vary by more than 40%, and outside the Galactic plane (i.e., where it is the dominant component) it does not vary by more than 20%. This indicates that the diffuse model is quite accurate. Nevertheless, the statistical precision of the data is so good that the deviations are

formally very significant. Leaving those parameters free allows releasing some of the tension that exists locally between the data and the diffuse model.

At high latitudes (left-hand plots) the isotropic component is stable (as it should be), but the Galactic normalization shows a clear north–south effect. The model is too high in the south but lacks emission in the north. The middle plot also indicates that the model is somewhat too hard particularly in the north. The group of points where the model is too hard in the south is around (R.A., decl.) = (+10°, −60°).

At low latitudes (right-hand plots) the error bars on the Galactic diffuse parameters are very small and the parameter values are very correlated between an RoI and its neighbor. This is because the distance between the centers of neighboring RoIs in the plane (a few degrees) is much smaller than their diameter (15°–20°). The model appears to be too low and somewhat too hard east of the Galactic center (around longitude +35°), whereas it is too high and too soft just west of the Carina region (around longitude −80°). Outside those two regions the fitted Galactic model is very close to the original one. Inside the plane the isotropic component is a minor contributor, and it tends to fluctuate a lot.

Figure 26 is another illustration of the same effect. It shows the residuals between the data and the full-sky model (original diffuse model + 3FGL sources, without any free parameter), integrated from 100 MeV to 100 GeV. The figure is restricted to the Galactic plane because at the scale shown here ($0°.5$ pixels) nothing comes out clearly at high latitude. The units are

99 http://aladin.u-strasbg.fr/
100 http://www.star.bristol.ac.uk/m̄bt/topcat/
101 http://aplpy.github.com
102 http://healpix.jpl.nasa.gov/

sigma units (statistical deviations). The model was originally computed with 0°.1 pixels in order to model the sources accurately. The main features are the data excess east of the Galactic center and the data deficit around −80°, which correspond to the features in Figure 25.

APPENDIX B
DESCRIPTION OF THE FITS VERSION
OF THE 3FGL CATALOG

The FITS format version of the 3FGL catalog[103] has four binary table extensions. The extension `LAT_Point_Source_Catalog` Extension has all of the information about the sources, including the monthly light curves (Table 16).

The extension `Hist_Start` lists the Mission Elapsed Time (seconds since 00:00 UTC on 2000 January 1) of the start of each bin of the monthly light curves. The final entry is the ending time of the last bin.

The extension `GTI` is a standard GTI listing the precise time intervals (start and stop in MET) included in the data analysis. The number of intervals is fairly large because on most orbits (~95 minutes) *Fermi* passes through the SAA, and science data taking is stopped during these times. In addition, data taking is briefly interrupted on each non-SAA-crossing orbit, as *Fermi* crosses the ascending node. Filtering of time intervals with large rocking angles, other data gaps, or operation in non-standard configurations introduces some more entries. The GTI is provided for reference and would be useful, e.g., for reconstructing the precise data set that was used for the 2FGL analysis.

The extension `ExtendedSources` (format unchanged since 2FGL) contains information about the 25 spatially extended sources that are modeled in the 3FGL catalog, including locations and shapes.

REFERENCES

Abdo, A. A., Abeysekara, U., Allen, B. T., et al. 2012a, ApJ, 753, 159
Abdo, A. A., Ackermann, M., Ajello, M., et al. 2009a, PhRvD, 80, 122004
Abdo, A. A., Ackermann, M., Ajello, M., et al. 2009b, ApJL, 706, L1
Abdo, A. A., Ackermann, M., Ajello, M., et al. 2009c, ApJL, 701, L123
Abdo, A. A., Ackermann, M., Ajello, M., et al. 2009d, ApJS, 183, 46
Abdo, A. A., Ackermann, M., Ajello, M., et al. 2009e, ApJL, 706, L56
Abdo, A. A., Ackermann, M., Ajello, M., et al. 2009f, ApJL, 707, L142
Abdo, A. A., Ackermann, M., Ajello, M., et al. 2009g, APh, 32, 193
Abdo, A. A., Ackermann, M., Ajello, M., et al. 2010a, ApJ, 714, 927
Abdo, A. A., Ackermann, M., Ajello, M., et al. 2010b, A&A, 523, A46
Abdo, A. A., Ackermann, M., Ajello, M., et al. 2010c, Sci, 328, 725
Abdo, A. A., Ackermann, M., Ajello, M., et al. 2010d, ApJS, 188, 405
Abdo, A. A., Ackermann, M., Ajello, M., et al. 2010e, ApJ, 708, 1254
Abdo, A. A., Ackermann, M., Ajello, M., et al. 2010f, ApJ, 718, 348
Abdo, A. A., Ackermann, M., Ajello, M., et al. 2010g, ApJ, 713, 146
Abdo, A. A., Ackermann, M., Ajello, M., et al. 2010h, Sci, 329, 817
Abdo, A. A., Ackermann, M., Ajello, M., et al. 2010i, Sci, 327, 1103
Abdo, A. A., Ackermann, M., Ajello, M., et al. 2010j, ApJ, 712, 459
Abdo, A. A., Ackermann, M., Ajello, M., et al. 2010k, A&A, 512, A7
Abdo, A. A., Ackermann, M., Ajello, M., et al. 2011a, ApJL, 736, L11
Abdo, A. A., Ackermann, M., Ajello, M., et al. 2011b, ApJ, 734, 116
Abdo, A. A., Ackermann, M., Ajello, M., et al. 2011c, Sci, 331, 739
Abdo, A. A., Ackermann, M., Ajello, M., et al. 2011d, ApJ, 734, 28
Abdo, A. A., Ackermann, M., Ajello, M., et al. 2012b, ApJ, 758, 140
Abdo, A. A., Ajello, M., Allafort, A., et al. 2013, ApJS, 208, 17
Abdo, A. A., Allen, B., Berley, D., et al. 2007, ApJL, 664, L91
Abdo, A. A., Allen, B. T., Aune, T., et al. 2009h, ApJL, 700, L127
Acero, F., Ackermann, M., Ajello, M., et al. 2013, ApJ, 773, 77
Ackermann, M., Ajello, M., Albert, A., et al. 2012a, ApJS, 203, 4
Ackermann, M., Ajello, M., Albert, A., et al. 2014, Sci, 345, 554

Ackermann, M., Ajello, M., Allafort, A., et al. 2011a, Sci, 334, 1103
Ackermann, M., Ajello, M., Allafort, A., et al. 2011b, ApJ, 743, 171
Ackermann, M., Ajello, M., Allafort, A., et al. 2012b, ApJ, 753, 83
Ackermann, M., Ajello, M., Allafort, A., et al. 2012c, APh, 35, 346
Ackermann, M., Ajello, M., Allafort, A., et al. 2013a, ApJS, 209, 34
Ackermann, M., Ajello, M., Asano, K., et al. 2013b, ApJS, 209, 11
Ackermann, M., Ajello, M., & Atwood, W. 2015, ApJ, submitted
Aharonian, F., Akhperjanian, A. G., Aye, K.-M., et al. 2005, A&A, 439, 1013
Aharonian, F., Akhperjanian, A. G., Barres de Almeida, U., et al. 2008, A&A, 477, 353
Aharonian, F., Akhperjanian, A. G., Bazer-Bachi, A. R., et al. 2006, Natur, 439, 695
Aharonian, F., Akhperjanian, A. G., Bazer-Bachi, A. R., et al. 2007, A&A, 472, 489
Ajello, M., Allafort, A., Baldini, L., et al. 2012, ApJ, 744, 80
Aliu, E., Aune, T., Behera, B., et al. 2014, ApJ, 788, 78
Allafort, A., Baldini, L., Ballet, J., et al. 2013, ApJL, 777, L2
Arsioli, B., Fraga, P., Giommi, P., Padovani, P., & Marrese, P. M. 2015, A&A, in press
Atwood, W. B., Abdo, A. A., Ackermann, M., et al. 2009, ApJ, 697, 1071
Baumgartner, W. H., Wayne, H., Tueller, J., Markwardt, C., & Skinner, G. 2010, BAAS, 42, 675
Bird, A. J., Bazzano, A., Bassani, L., et al. 2010, ApJS, 186, 1
Bregeon, J., Charles, E., & Wood, M. 2013, arXiv:1304.5456
Casandjian, J.-M., & the Fermi LAT Collaboration 2015, arXiv:1502.07210
Casandjian, J.-M., & Grenier, I. A. 2008, A&A, 489, 849
Clark, J. S., Larionov, V. M., & Arkharov, A. 2005, A&A, 435, 239
Condon, J. J., Cotton, W. D., Greisen, E. W., et al. 1998, AJ, 115, 1693
Corbet, R. H. D., Cheung, C. C., Kerr, M., et al. 2011, ATel, 3221, 1
D'Abrusco, R., Massaro, F., Paggi, A., et al. 2014, ApJS, 215, 14
de Palma, F., Brandt, T. J., Johannesson, G., Tibaldo, L., & the Fermi LAT Collaboration 2013, arXiv:1304.1395
de Ruiter, H. R., Arp, H. C., & Willis, A. G. 1977, A&AS, 28, 211
Dias, W. S., Alessi, B. S., Moitinho, A., & Lépine, J. R. D. 2002, A&A, 389, 871
Dormody, M., Johnson, R. P., Atwood, W. B., et al. 2011, ApJ, 742, 126
Ferrand, G., & Safi-Harb, S. 2012, AdSpR, 49, 1313
Górski, K. M., Hivon, E., Banday, A. J., et al. 2005, ApJ, 622, 759
Green, D. A. 2009, BASI, 37, 45
Grégoire, T., & Knödlseder, J. 2013, A&A, 554, A62
Griffith, M. R., & Wright, A. E. 1993, AJ, 105, 1666
Grondin, M.-H., Funk, S., Lemoine-Goumard, M., et al. 2011, ApJ, 738, 42
Guillemot, L., Kramer, M., Johnson, T. J., et al. 2013, ApJ, 768, 169
Harris, W. E. 1996, AJ, 112, 1487
Hartman, R. C., Bertsch, D. L., Bloom, S. D., et al. 1999, ApJS, 123, 79
Healey, S. E., Romani, R. W., Cotter, G., et al. 2008, ApJS, 175, 97
Healey, S. E., Romani, R. W., Taylor, G. B., et al. 2007, ApJS, 171, 61
Helene, O. 1983, NIMPR, 212, 319
HESS Collaboration 2011, A&A, 529, A49
Hewitt, J. W., Grondin, M.-H., Lemoine-Goumard, M., et al. 2012, ApJ, 759, 89
Hou, X., Smith, D. A., Guillemot, L., et al. 2014, A&A, 570, A44
Johannesson, G., Orlando, E., & the Fermi-LAT Collaboration 2013, arXiv:1307.0197
Johnson, T. J., Guillemot, L., Kerr, M., et al. 2013, ApJ, 778, 106
Katagiri, H., Tibaldo, L., Ballet, J., et al. 2011, ApJ, 741, 44
Katsuta, J., Uchiyama, Y., Tanaka, T., et al. 2012, ApJ, 752, 135
Kerr, M. 2010, PhD thesis, Univ. Washington
Kimball, A. E., & Ivezić, Ž 2008, AJ, 136, 684
Lande, J., Ackermann, M., Allafort, A., et al. 2012, ApJ, 756, 5
Leahy, D. A., & Tian, W. W. 2012, A&A, 539, A128
Liu, Q. Z., van Paradijs, J., & van den Heuvel, E. P. J. 2006, A&A, 455, 1165
Liu, Q. Z., van Paradijs, J., & van den Heuvel, E. P. J. 2007, yCat, 346, 90807
Lonsdale, C., Conrow, T., Evans, T., et al. 1998, in IAU Symp. 179, New Horizons from Multi-Wavelength Sky Surveys, ed. B. J. McLean, D. A. Golombek, J. J. E. Hayes, & H. E. Payne (Dordrecht: Kluwer), 450
Lorimer, D. R., Faulkner, A. J., Lyne, A. G., et al. 2006, MNRAS, 372, 777
Maíz-Apellániz, J., Walborn, N. R., Galué, H. Á, & Wei, L. H. 2004, ApJS, 151, 103
Manchester, R. N., Hobbs, G. B., Teoh, A., & Hobbs, M. 2005, AJ, 129, 1993
Masci, F. J., Condon, J. J., Barlow, T. A., et al. 2001, PASP, 113, 10
Massaro, E., Giommi, P., Leto, C., et al. 2009, A&A, 495, 691
Mattox, J. R., Bertsch, D. L., Chiang, J., et al. 1996, ApJ, 461, 396
Mauch, T., Murphy, T., Buttery, H. J., et al. 2003, MNRAS, 342, 1117
McConnachie, A. W. 2012, AJ, 144, 4
Moskalenko, I. V., & Strong, A. W. 1998, ApJ, 493, 694
Murphy, T., Sadler, E. M., Ekers, R. D., et al. 2010, MNRAS, 402, 2403

---

[103] The file is available from the FSSC, http://fermi.gsfc.nasa.gov/ssc.

Nolan, P. L., Abdo, A. A., Ackermann, M., et al. 2012, ApJS, 199, 31
Petrov, L., Mahony, E. K., Edwards, P. G., et al. 2013, MNRAS, 432, 1294
Pittori, C., Verrecchia, F., Chen, A. W., et al. 2009, A&A, 506, 1563
Pivato, G., Hewitt, J. W., Tibaldo, L., et al. 2013, ApJ, 779, 179
Prestage, R. M., & Peacock, J. A. 1983, MNRAS, 204, 355
Reichardt, I., de Oña-Wilhelmi, E., Rico, J., & Yang, R. 2012, A&A, 546, A21
Reitberger, K., Reimer, A., Reimer, O., & Takahashi, H. 2015, A&A, in press
Reitberger, K., Reimer, O., Reimer, A., et al. 2012, A&A, 544, A98
Sanders, D. B., Mazzarella, J. M., Kim, D.-C., Surace, J. A., & Soifer, B. T.
    2003, AJ, 126, 1607
Schmidt, K., Priebe, A., & Boller, T. 1993, AN, 314, 371

Strong, A. W. 2007, Ap&SS, 309, 35
Strong, A. W., Porter, T. A., Digel, S. W., et al. 2010, ApJL, 722, L58
Sutherland, W., & Saunders, W. 1992, MNRAS, 259, 413
Tam, P. H. T., Huang, R. H. H., Takata, J., et al. 2011a, ApJL, 736, L10
Tam, P. H. T., Kong, A. K. H., Hui, C. Y., et al. 2011b, ApJ, 729, 90
Tanaka, T., Allafort, A., Ballet, J., et al. 2011, ApJL, 740, L51
Tavani, M., Bulgarelli, A., Vittorini, V., et al. 2011, Sci, 331, 736
van der Hucht, K. A. 2001, NewAR, 45, 135
Véron-Cetty, M.-P., & Véron, P. 2010, A&A, 518, A10
Voges, W., Aschenbach, B., Boller, T., et al. 1999, A&A, 349, 389
Watters, K. P., & Romani, R. W. 2011, ApJ, 727, 123